





Turbulent gas-rich disks at high redshift: bars & bulges in a radial shear flow

JOSS BLAND-HAWTHORN ^{1,2} THOR TEPPER-GARCIA ^{1,2} OSCAR AGERTZ ³ AND CHRISTOPH FEDERRATH ^{4,2}

¹*Sydney Institute for Astronomy, School of Physics, A28, The University of Sydney, NSW 2006, Australia*

²*Centre of Excellence for All-Sky Astrophysics in Three Dimensions (ASTRO 3D), Australia*

³*Lund Observatory, Division of Astrophysics, Department of Physics, Lund University, Box 43, SE-221 00 Lund, Sweden*

⁴*Research School of Astronomy and Astrophysics, Australian National University, Canberra, ACT 2611, Australia*

ABSTRACT

Recent observations of high-redshift galaxies ($z \lesssim 7$) reveal that a substantial fraction have turbulent, gas-rich disks with well-ordered rotation and elevated levels of star formation. In some instances, disks show evidence of spiral arms, with bar-like structures. These remarkable observations have encouraged us to explore a new class of dynamically self-consistent models using our AGAMA/RAMSES hydrodynamic N-body simulation framework that mimic a plausible progenitor of the Milky Way at high redshift. We explore disk gas fractions of $f_{\text{gas}} = 0, 20, 40, 60, 80, 100\%$ and track the creation of stars and metals. The high gas surface densities encourage vigorous star formation, which in turn couples with the gas to drive turbulence. We explore three distinct histories: (i) there is no ongoing accretion and the gas is used up by the star formation; (ii) the star-forming gas is replenished by cooling in the hot halo gas; (iii) in a companion paper, we revisit these models in the presence of a strong perturbing force. At low $f_{\text{disk}} (\lesssim 0.3)$, where f_{disk} is the mass fraction of stars relative to dark matter within $2.2 R_{\text{disk}}$, a bar does not form in a stellar disk; this remains true even when gas dominates the inner disk potential. For a dominant baryon disk ($f_{\text{disk}} \gtrsim 0.5$) at all gas fractions, the turbulent gas forms a strong *radial shear flow* that leads to an intermittent star-forming bar within about 500 Myr; turbulent gas speeds up the formation of bars compared to gas-free models. For $f_{\text{gas}} \lesssim 60\%$, all bars survive, but for higher gas fractions, the bar devolves into a central bulge after 1 Gyr. The star-forming bars are reminiscent of recent discoveries in high-redshift ALMA observations of gaseous disks.

Keywords: galaxies: high-redshift; galaxies: ISM; galaxies: kinematics and dynamics; galaxies: structure

1. INTRODUCTION

Stellar bars have long intrigued astronomers, not least because they are a common feature of galaxies in the local universe (Erwin 2018), but what do they teach us? A cold stellar disk with ordered rotation is a low-entropy system that wants to transport angular momentum outwards. Bar instabilities are routinely observed in N-body disk simulations (Hohl 1971; Athanassoula & Sellwood 1986), and are a genuine feature of synthetic disks supported by other approaches to dynamical analysis (Sellwood & Wilkinson 1993). *All* galactic disks are unstable to the onset of bars ultimately – just why they arise was first illustrated by Toomre (1981). Disk perturbations are amplified into outward-propagating (leading) waves by the shearing action of the disk; if the inner galactic potential is not too deep, the trailing waves can tunnel through the centre and emerge as leading waves, thereby “swing amplifying” the instability in a positive feedback loop, analogous to the action of a resonant laser cavity. Thus, bars probe the inner galactic potential (including the influence of any supermassive black hole), the dynamical stability and maturity of the stellar disk, the outer halo through the bar’s angular velocity and, most notably, the degree of baryon domination over dark matter within the domain of the stellar disc.

In light of recent developments, our view of disk formation in the early universe is undergoing a radical overhaul. With the launch of the James Webb Space Telescope (JWST), a new window into the distant universe has revealed that (mostly thin) disk galaxies¹ dominate the population out to at least $z \approx 6$ (Kartaltepe et al. 2023; Ferreira et al. 2022; Robertson et al. 2023), although further analysis is needed (Huertas-Company et al. 2023). We can use bars (and bulges) to learn about the early history of galaxies, particularly when the phenomenon can be traced to the highest redshifts. The recent discovery of high-redshift stellar bars (Guo et al. 2022; Le Conte et al. 2023; Costantin et al. 2023) is one of the early successes of the JWST. If baryons dominate the local gravitational potential (e.g. Price et al. 2021), stellar bars can form in $1 - 2$ Gyr (Bland-Hawthorn et al. 2023).

The early disks have provided a number of unexpected results. While there are selection effects to consider, most of the early disks observed to date are very rich in gas and exhibit high levels of star formation. In the redshift range $z = 1.1 - 2.3$, Guo et al. (2022) showed that turbulent star-forming disks can have well-developed stellar bars that look much like their mature low-redshift counterparts. Even spiral arms have been observed in turbulent (“hot”) disk galaxies at $z \approx 2 - 2.5$ (Dawson et al. 2003; Law et al. 2012; Yuan et al. 2017; Margalef-Bentabol et al. 2022); in one instance, the galaxy disk appears to have three spiral arms (Law et al. 2012), a rare phenomenon in the local universe.

Our new work is in response to ALMA, VLA and integral-field spectroscopic observations of gas-rich, star-forming disks in the redshift range $z \sim 1 - 3$ (Chapman et al. 2004; Genzel et al. 2006; Förster Schreiber et al. 2006), supported by subsequent observations (Shapiro et al. 2008; Swinbank et al. 2012; Hodge et al. 2019; Neeleman et al. 2021; Rizzo et al. 2022). Intriguingly, there are clear cases where the gas entirely dominates the baryon disk fraction (e.g. Hodge et al. 2019; Rizzo et al. 2022), and even here bar-like features and/or velocity fields are observed (Tsukui et al. 2024; Smail et al. 2023; Huang et al. 2023; Neeleman et al. 2023). In these instances, *stellar* bars are either weak or non-existent.

So what are these “gaseous bars”? Very little is known about the evolution of non-axisymmetric perturbations in gas-rich disks (q.v. Cazes & Tohline 2000). For earlier publications on bar formation that include gas, only a narrow range in gas fraction is treated and few consider prescriptions for star formation. A notable example that does consider bar formation in star-forming disks is Seo et al. (2019), but here $f_{\text{gas}} \lesssim 10\%$. Gas-dominated disks are a difficult problem that requires the gas to be internally supported if it is to avoid collapsing on a dynamical timescale ($\lesssim 100$ Myr).

But these must be considered because there is a tendency for the disk mass fraction in the form of gas to increase with redshift (Carilli & Walter 2013; Tacconi et al. 2020). Star formation rates, gas turbulence and clumpiness also increase, such that the mean circular rotation speed divided by the internal gas velocity dispersion V_c/σ declines with increasing redshift (Wisnioski et al. 2015; Zhou et al. 2017). Importantly, gas dispersions measured with cool molecular lines tend to be narrower than dispersions measured with emission lines arising from warmer ionized gas. Both measures of dispersion, however, show an increasing trend with redshift (Ejdetjärn et al. 2022). Wisnioski et al. (2015) argued that these galaxies were in quasi-equilibrium, being fed by smooth accretion of cool gas from the environment, with galaxy mergers playing a lesser role. The fraction of these disks that are dynamically settled is unclear (Förster Schreiber et al. 2006), with some authors suggesting that half (Bellocchi et al. 2012; Rodrigues et al. 2017) or all (Simons et al. 2019) of these systems could be experiencing strong mergers, within the limits of the integral-field spectroscopic observations.

We have developed² a new high-resolution (parsec scale) simulation framework that is ideally suited to discovering how turbulent disks evolve dynamically. In high-redshift galaxies, the observed high gas fraction and enhanced gas surface densities lead to elevated star-formation rates and the output energy and momentum couples with the gas and drives the turbulence (Agertz et al. 2009). A turbulent (compressible) gas disk with ordered rotation, perhaps surprisingly, shares dynamical similarities with (collisionless) stellar disks. It may even be susceptible to bar instabilities, although there is very little published work on this problem (Cazes & Tohline 2000).

Our first paper is focussed on objects with halo masses of order $10^{11} M_\odot$, a dynamical mass that is characteristic of the recent JWST discoveries at $z \sim 1 - 3$ (Guo et al. 2022; Le Conte et al. 2023; Costantin et al. 2023). This is the expected mass of a Milky Way progenitor at that epoch. (We consider more massive systems in a later paper because these are more representative of the ALMA disks observed to date.) Our first step is to consider a galactic ecosystem in some form of dynamical equilibrium, with and without smooth accretion from the ambient hot corona. As we show,

¹ We caution that the JWST disk fraction is inferred from multiband photometry. At $z < 1$, Neichel et al. (2008) found a high degree of correlation between photometric “disks” and ordered rotation in kinematic studies, but the relevance of the Sérsic fitting function out to such high redshifts has yet to be established.

² The broader context of controlled experiments on isolated disks is presented in App. A.

these ecosystems manifest intermittent and long-lived behaviour, including disk-halo interaction, bars and spiral arms, bulge formation, and so forth. We discover “bar-like” phenomena for the first time at all gas fractions, even in fully gas-dominated turbulent disks, including a remarkable “radial shear flow” with its own unique signatures. Once again, as for the stellar disks, these bar-like signatures only arise in disks that dominate the local gravitational potential (Bland-Hawthorn et al. 2023).

The structure of the paper is as follows. In Sec. 2, we introduce and motivate the model parameters for a Milky Way progenitor galaxy. To carry out this work, we update the AGAMA self-consistent modelling module (Vasiliev 2019) to allow for the inclusion of gas components (disk, halo; details to be presented in a companion paper; Tepper-García et al., in prep). All of the computations are carried out with the RAMSES N-body/hydrodynamics code (Teyssier 2002) at low ($N_{\text{lo}} \sim 10^7$ elements) and high ($N_{\text{hi}} \sim 10^8$ elements) resolution, including star formation and metal production. We also conduct repeated simulations at the same initial conditions (different random seeds) to examine stochastic effects given the nature of turbulent media. In Sec. 3, we outline the main processes that lead to star formation in turbulent media. In Sec. 4, we present the main findings from the new simulations and provide links to the simulation movies. In Sec. 5, we discuss the simulations and their implications for high-redshift disks, before drawing our conclusions in Sec. 6.

2. GALAXY MODELS AND SIMULATIONS

2.1. Framework and initial conditions

In defining a Milky Way progenitor, we adopt a model with three key components – a live dark matter halo, a massive stellar/gaseous disk and, for a subset of models, a hot coronal gas filling the live dark matter halo, which serves to supply the disk with a smooth flow of accreting gas after it cools. The hot coronal gas also compresses the disk-halo interaction maintained by feedback processes. Our intent is to minimize the number of free parameters in the model while retaining its usefulness. Small central bulges tend to form during the evolution of the disk, or from gas accreting from the halo, but we do not start with central bulges when simulating such early disks.

In the gaseous disk, the star formation rate is set by the gas surface density and this activity feeds back sufficient energy and momentum to maintain the turbulent pressure support (see below). We explore two distinct accretion histories: (i) there is no ongoing accretion and the gas is used up by the star formation; (ii) the star-forming gas is replenished by cooling in the hot halo gas. In a later paper, we explore the response to a strong impulse triggered by an interacting, massive companion.

The initial conditions (particle positions and velocities) for each of the components making up our Galaxy model are created with the Action-based GALaxy Modelling Architecture software package (AGAMA; Vasiliev 2019). The reader is referred to Tepper-García et al. (2021, their section 3) for a detailed description of AGAMA’s self-consistent module for the collisionless components in our model (dark matter [DM] halo, stellar disk). We have complemented the AGAMA framework to include the gas phase (cf. Tepper-García et al. 2022); our methodology is described in detail in a companion paper (Tepper-García et al., in preparation). Here only a brief description is provided for completeness.

Our approach for setting up a gas disk follows Wang et al. (2010) who give a prescription for isothermal gas disks in equilibrium. The gas disk is initially perfectly isothermal and axisymmetric, with a surface density profile described by a radially declining function proportional to $\exp(-R/R_{\text{disk}})$, where R_{disk} is the scalelength of the disk. Its vertical structure is dictated by the total gravitational potential of the system, but roughly follows a $\text{sech}^2(z/z_0)$ profile, characteristic of a gas distribution in hydrostatic equilibrium, with a scaleheight z_0 that varies with cylindrical radius (a ‘flaring’ disk). The azimuthal velocity profile of the gas disk ensures rotational support against radial instabilities (see Wang et al. 2010, their equation 13). The initial (somewhat artificial) configuration of the gas disk does not greatly affect its long-term evolution, but is important however to define the model through its initial gas fraction f_{gas} .

In setting up the hot gaseous halo, we focus our attention on pressure-supported, spinning gas configurations, embedded within a DM halo of mass M_{halo} . For simplicity, the hot halo is assumed to follow initially the same profile as its host DM halo (e.g. Mo et al. 1998; Ascasibar et al. 2003; Teyssier et al. 2013). The hot halo mass is chosen so as to close the cosmic baryon budget in the box. The cosmic baryon fraction $f_b = 0.16$ (Planck Collaboration et al. 2020) implies a hot halo mass of approximately $5.5 \times 10^9 M_{\odot}$. This is appropriate for a Milky Way progenitor at $z \approx 3$.

Since the mass distribution of the hot halo is fixed by construction, all that remains to be calculated is its velocity structure and the internal energy (temperature). The velocity structure, i.e. rotation speed, is calculated assuming that the specific angular momentum of the gas, j_h , follows that of the dark matter (c.f. Bullock et al. 2001; Kaufmann et al. 2006). We adopt $v_{\phi}(r) = j_h(r) / r \propto M_{\text{halo}}(< r) / r$. The specific internal energy of the gas, corrected for its

net rotation speed $v_\phi(r)$, is given by $e = (\gamma - 1)^{-1} (c_s^2 - v_\phi^2)$, where c_s is the hydrostatic (i.e. $v_\phi \equiv 0$) sound speed. This approach results in gas temperatures of about a few 10^6 K close to the centre and $\sim 10^4$ K in the outer regions, and rotation speeds in the range $10\text{--}50$ km s $^{-1}$.

It is worth emphasising that, as with the gas disk, the initial configuration of the hot halo is largely irrelevant to the subsequent evolution of the galaxy, with the exception of its mass, which will impact the amount of accretion onto the disk. Finally, we note that the mass of the hot halo does not count towards the gas fraction f_{gas} that defines each model; the latter is entirely defined by the initial cool gas assigned to the disk.

2.2. Progenitor galaxy parameters

We now describe the choice of parameters for our progenitor analogue at high redshift. Within the context of the CDM hierarchy, it is possible to estimate the likely mass and size evolution of a Milky Way progenitor with cosmic time. Bland-Hawthorn & Gerhard (2016, their figure 1) use a Press-Schechter code to estimate the 1σ range in total halo mass and size with redshift across all merger trees that lead to the Milky Way’s estimated mass ($\log M_{\text{vir}}/M_\odot = 12.1$) and size ($R_{\text{vir}} \approx 280$ kpc) at $z = 0$. Over the redshift range from $z \approx 3$ to the present day, the halo mass and size increase by an order of magnitude. In support of this, Kartaltepe et al. (2023, their figure 1) show the distribution of baryon stellar masses for disk systems over the redshift interval $z \approx 1\text{--}6$. These exhibit a large scatter about a mean baryon mass of $\log M_\star/M_\odot = 9.5$ as compared with $\log M_\star/M_\odot \approx 10.6$ for the Milky Way at $z = 0$. In summary, for our Milky Way progenitor, we adopt halo parameters of $R_{\text{vir}} \approx 40$ kpc and $\log M_{\text{vir}}/M_\odot \approx 11$. The exact values are given in Tab. 1. The halo concentration is calculated for its given mass and redshift with the help of the COMMAH package (Correa et al. 2015).

The next important parameter is the disk mass fraction f_{disk} that determines how dominant the disk baryons are with respect to the underlying dark matter halo. This is defined as

$$f_{\text{disk}} = \left(\frac{V_{\text{c,disk}}(R_s)}{V_{\text{c,tot}}(R_s)} \right)_{R_s=2.2R_{\text{disk}}}^2. \quad (1)$$

Here $V_c(R)$ is the circular velocity at a radius R , R_{disk} is the exponential disk scalelength, and $R_s = 2.2R_{\text{disk}}$ is the traditional scalelength adopted in studies of disks. The Milky Way today has a dominant central disk with $f_{\text{disk}} = 0.5\text{--}0.65$ depending on the chosen bar model (Bland-Hawthorn & Gerhard 2016, their Fig. 17). Here we adopt $f_{\text{disk}} = 0.5$. There is evidence for a substantial fraction of disks dominating their local gravitational potential in the redshift interval $z \approx 1\text{--}2.5$ (Price et al. 2021). Baryon domination has an impact on the subsequent disk evolution as it becomes more susceptible to internal and external perturbations (Fujii et al. 2018; Bland-Hawthorn et al. 2023).

The third model parameter is the gas mass fraction within the same radial scale:

$$f_{\text{gas}} = \left(\frac{M_{\text{disk,gas}}}{M_{\text{disk}}} \right)_{R_s=2.2R_{\text{disk}}} \quad (2)$$

where M_{disk} is the total disk mass and $M_{\text{disk,gas}}$ is the gas contribution. This definition is not universal and care must be taken. The gas fraction declines as more of the mass is locked up in stars. The main parameters are listed in Tab. 1. The synthetic galaxy is composed of a host DM halo with a fixed mass, a pre-existing (‘old’) stellar disk, and a gaseous disk. The summed masses of the stellar and gaseous component are set to $\log M_{\text{disk}}/M_\odot \approx 10$, yielding $f_{\text{disk}} \approx 0.5$, but their individual masses (either gas or stars) are adjusted so as to attain different f_{gas} values in the range 0% to 100%. The evidence for a broad range in gas fractions is presented in Carilli & Walter (2013): the overall trend is an increasing gas fraction with increasing redshift, but the scatter is large.

The baryon mass is preserved in both the accreting and non-accreting halo models. In the former case, the total baryon mass of the disk increases with time. Note that the initial scalelength of the disk (both gas and stars) is roughly maintained at $R_{\text{disk}} \approx 1.8$ kpc across models. At $z \sim 0$, the gaseous and stellar disk scalelengths can differ by a factor of two (e.g. Milky Way; Bland-Hawthorn & Gerhard 2016) due to the cumulative effect of gas accretion at later times. The above parameters are broadly consistent with arguably the best Milky Way progenitor analogue to date, the object CEERS-2112 at a photometric redshift of $z \approx 3.0$ (Costantin et al. 2023).

2.3. Galaxy formation physics

The galaxies are evolved using the hydrodynamics+ N -body code RAMSES (Teyssier 2002). RAMSES adopts an oct-tree hierarchical grid that provides adaptive resolution and solves the fluid equations using a second-order unsplit

M_\star ($10^8 M_\odot$)	M_{gas} ($10^8 M_\odot$)	R_{disk} (ckpc)	f_{disk}	f_{gas}	Label	High	Low
9.80	0.0	0.7	0.3	0.0	fd30_fg00_nac	0	1
7.80	2.0	0.7	0.3	0.2	fd30_fg20_nac	0	1
5.90	3.90	0.7	0.3	0.4	fd30_fg40_nac	0	1
3.90	5.90	0.7	0.3	0.6	fd30_fg60_nac	0	1
112	0.0	1.8	0.5	0.0	fd50_fg00_nac	0	1
88.8	22.2	1.8	0.5	0.2	fd50_fg20_nac	2	1
66.6	44.4	1.8	0.5	0.4	fd50_fg40_nac	2	3
44.4	66.6	1.8	0.5	0.6	fd50_fg60_nac	2	1
22.2	88.8	1.8	0.5	0.8	fd50_fg80_nac	0	1
0.0	112	1.8	0.5	1.0	fd50_fg100_nac	0	1
88.8	22.2	1.8	0.5	((0.2))	fd50_fg20_ac	0	1
66.6	44.4	1.8	0.5	((0.4))	fd50_fg40_ac	0	1
44.4	66.6	1.8	0.5	((0.6))	fd50_fg60_ac	0	1
22.2	88.8	1.8	0.5	((0.8))	fd50_fg80_ac	0	1
0.0	112	1.8	0.5	((1.0))	fd50_fg100_ac	0	1
555	0.0	3.0	0.7	0.0	fd70_fg00_nac	0	1
444	111	3.0	0.7	0.2	fd70_fg20_nac	0	1
333	222	3.0	0.7	0.4	fd70_fg40_nac	0	1
222	333	3.0	0.7	0.6	fd70_fg60_nac	0	1

Table 1. Overview of galaxy models. The DM host halo properties ($M_{\text{halo}} = 10^{11} M_\odot$; $R_{\text{vir}} = 37$ ckpc; $r_s = 9.2$ ckpc) are identical across models, and they are consistent with a MW-progenitor analogue at $z \approx 3$. Table columns are as follows: (1) Disk stellar mass; (2) Disk gas mass; (3) Disk scalelength; (4) disk-to-total mass ratio (Eq. 1); (5) Gas to total disk mass fraction at $t = 0$ (Eq. 2) – the double brackets indicate accreting gas from a hot corona with a mass $M \approx 5.5 \times 10^9 M_\odot$ at $t = 0$; note that the hot halo mass is not accounted for in f_{gas} . (6) Model designation; (7) No. of high-resolution models; (8) No. of low-resolution models with different random seeds.

Godunov method with the HLLC approximate Riemann solver (Toro 1999). We apply a MinMod slope limiter to reconstruct the piecewise linear solution for the Godunov solver. To close the relation between gas pressure and internal energy, we use an ideal gas equation of state with an adiabatic index $\gamma = 5/3$. Mesh refinement is based on a quasi-Lagrangian approach, where a cell is split into 8 sub-cells if its mass exceeds $94,000 M_\odot$ and $11,750 M_\odot$ in the low- and high-resolution models, respectively. In addition, a cell is allowed to refine if it contains more than 8 dark matter particles. We allow for 12 (14) levels of grid refinement in the low (high) resolution suite, leading to a finest grid resolution of 24 (6) parsecs.

The adopted star/galaxy formation physics is presented in Agertz et al. (2013) and Agertz et al. (2021). Briefly, star formation is treated as a Poisson process, sampled using $10^3 M_\odot$ star particles, occurring on a cell-by-cell basis according to the star formation law,

$$\dot{\rho}_\star = \epsilon_{\text{ff}} \frac{\rho_g}{t_{\text{ff}}} \quad \text{for } \rho_g > \rho_{\text{SF}}. \quad (3)$$

Here $\dot{\rho}_\star$ is the star formation rate density, ρ_g the gas density, $t_{\text{ff}} = \sqrt{3\pi/32G\rho_g}$ is the free-fall time, and ϵ_{ff} is the star formation efficiency per free-fall time of gas in the cell. The star formation threshold is set to $\rho_{\text{SF}} = 10(100) \text{ cm}^{-3}$ in the low(high)-resolution models. Grisdale et al. (2017, 2018, 2019) demonstrate how high star formation efficiencies ($\epsilon_{\text{ff}} \sim 10\%$) on scales of parsecs, coupled to the feedback models in this work, provide a close match to the observed density and velocity structure of the ISM in local spirals, as well as giant molecular cloud properties in good agreement with Milky Way observations. Motivated by these findings, we adopt $\epsilon_{\text{ff}} = 10\%$.

Each formed star particle is treated as a single-age stellar population with a Chabrier (2003) initial mass function. We account for injection of energy, momentum, mass, and heavy elements over time from core-collapse SN and SNIa, stellar winds, and radiation pressure into the surrounding gas. Each mechanism depends on stellar age, mass and gas/stellar metallicity (with main sequence lifetimes taken from Raiteri et al. 1996), calibrated on the stellar evolution

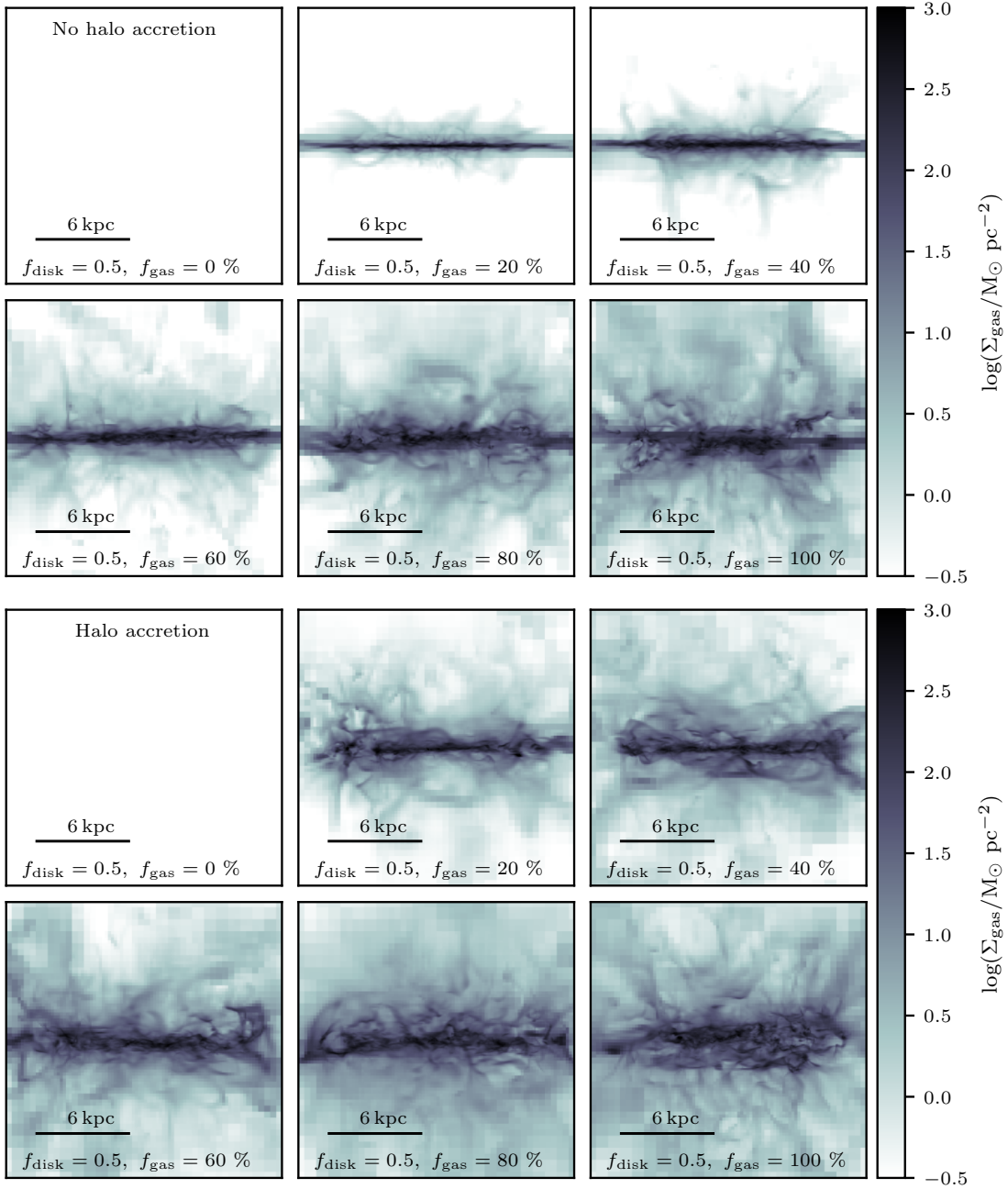


Figure 1. Edge-on gas surface density maps taken from our simulations at $t_o = 1$ Gyr for a disk mass fraction comparable to the Milky Way today. The panels are 18 kpc (comoving kpc) across. The top six panels are for six different initial gas fractions with *no* halo accretion; the bottom six are the matching simulations that include halo accretion.

code STARBURST99 (Leitherer et al. 1999). The effect of supernova explosions is captured following the approach by Kim & Ostriker (2015). Briefly, when the supernova cooling radius³ is resolved by more than 6 cells, supernova explosions are initialized in the ‘energy conserving’ phase by injecting 10^{51} erg per SN into the nearest grid cell. When

³ The cooling radius in gas with density n and metallicity Z scales as $\approx 30(n/1\text{cm}^3)^{-0.43}(Z/Z_\odot + 0.01)^{-0.18}\text{pc}$ for a SN explosion with energy $E_{\text{SN}} = 10^{51}$ erg (e.g. Cioffi et al. 1988; Thornton et al. 1998).

the cooling radius is resolved by less than 6 cells, the explosion is initialized in its ‘momentum conserving’ phase, with the momentum built up during the Sedov-Taylor phase⁴ injected into cells surrounding the star particle.

The iron (Fe) and oxygen (O) abundances are tracked separately, with yields taken from [Woosley & Heger \(2007\)](#). When computing the gas cooling rate, which is a function of the total metallicity, we construct a total metal mass following $M_Z = 2.09M_{\text{O}} + 1.06M_{\text{Fe}}$ (see [Kim et al. 2014](#)) according to the mixture of alpha and iron group elements for the Sun ([Asplund et al. 2009](#)). Metallicity dependent cooling is accounted for using the cooling functions by [Sutherland & Dopita \(1993\)](#) for gas temperatures in the range $10^{4-8.5}$ K, with rates from [Rosen & Bregman \(1995\)](#) used for cooling down to ~ 10 K. Heating from a cosmic UV background is modelled following [Haardt & Madau \(1996\)](#), under the assumption that gas self-shields at high enough densities (see [Aubert & Teyssier 2010](#)).

In order to provide a visual sense of what the different levels of disk-halo interaction look like, we present two collages in Fig. 1. The top collage shows the impact of star formation and feedback (for a range of gas fractions) when the disk is viewed edge-on after 1 Gyr. The gas is initially prescribed with no subsequent accretion. The bottom collage shows the matching models that have subsequent halo accretion of cool gas from the hot corona surrounding each galaxy.

3. STAR FORMATION IN TURBULENT MEDIA: BASIC EQUATIONS AND CONCEPTS

Many authors have considered star formation in turbulent media ([Padoan 1995](#); [Klessen et al. 2000](#); [Elmegreen et al. 2003](#); [Krumholz & McKee 2005](#); [Padoan & Nordlund 2011](#); [Hennebelle & Chabrier 2011](#); [Federrath & Klessen 2012](#); [Federrath 2018](#); [Burkhart & Mocz 2019](#)), motivated by the fact that clouds in nearby galaxies and the Milky Way have non-thermal line widths (e.g., [Larson 1981](#); [Solomon et al. 1987](#); [Ossenkopf & Mac Low 2002](#); [Heyer & Brunt 2004](#); [Rosolowsky & Blitz 2005](#)), widely believed to be due to supersonic turbulence ([Federrath et al. 2021a](#)). Both from observations and simulations, the turbulent velocity dispersion σ_v averaged over a volume of diameter ℓ scales as $\sigma_v \propto \ell^p$ with $p \approx 0.5$ ([Larson 1981](#); [Heyer & Brunt 2004](#); [Roman-Duval et al. 2011](#); [Federrath 2013](#); [Federrath et al. 2021a](#)).

3.1. The gas density distribution

Supersonically turbulent, isothermal gas has a lognormal density distribution ([Vázquez-Semadeni 1994](#); [Passot & Vázquez-Semadeni 1998](#); [Padoan & Nordlund 2002](#); [Kritsuk et al. 2007](#)) such that

$$p(s) = \frac{1}{\sqrt{2\pi\sigma_s^2}} \exp \left[-\frac{(s - s_0)^2}{2\sigma_s^2} \right], \quad (4)$$

for which $s = \ln(\rho/\rho_0)$ is the dimensionless log-density contrast (i.e., the natural logarithm of the density divided by the mean density ρ_0), and the average log-density parameter is $s_0 = -(1/2)\sigma_s^2$ ([Li et al. 2003](#); [Federrath et al. 2008, 2010](#)). The dispersion in density of $p(s)$ over the region is ([Padoan & Nordlund 2011](#); [Molina et al. 2012](#))

$$\sigma_s = \sqrt{\ln \left(1 + b^2 \mathcal{M}^2 \frac{\beta}{\beta + 1} \right)}, \quad (5)$$

where $\mathcal{M} = \sigma_v/c_s$ is the three-dimensional (3D) turbulent Mach number of the medium, c_s is the sound speed within the density fluctuation of diameter ℓ , and β is the plasma beta parameter (ratio of thermal to magnetic pressure; note that $\beta \rightarrow \infty$ in cases without magnetic fields). The parameter b in Eq. (5) is the turbulence driving parameter, which is controlled by the mixture of solenoidal vs. compressive modes in the driving mechanism of the turbulence ([Federrath et al. 2008](#)). Purely solenoidal (divergence-free) driving has $b \sim 1/3$, while purely compressive (curl-free) driving is characterised by $b \sim 1$ ([Federrath et al. 2010](#); [Dhawalikar et al. 2022](#); [Gerrard et al. 2023](#)). Slight modifications of Eq. (5) can be made to account for non-isothermal gas conditions ([Nolan et al. 2015](#); [Federrath & Banerjee 2015](#)). We do not consider magnetic fields in this early analysis; these supply local pressure support and therefore tend to slow down the evolution of collapsing filaments (e.g., [Li et al. 2004](#); [Padoan & Nordlund 2011](#); [Federrath 2015](#)). We consider the consequences of magnetohydrodynamics (MHD) and turbulence in a later paper.

⁴ The adopted relation for the momentum is $4 \times 10^5 (E_{\text{SN}}/10^{51} \text{ erg})^{16/17} (n/1 \text{ cm}^{-3})^{-2/17} (Z/Z_{\odot})^{-0.2} M_{\odot} \text{ km s}^{-1}$ (e.g. [Blondin et al. 1998](#); [Kim & Ostriker 2015](#); [Hopkins 2018](#)), where E_{SN} is the total energy injected by SNe in a cell with gas density n and metallicity Z compared to Solar ($Z_{\odot} = 0.02$).

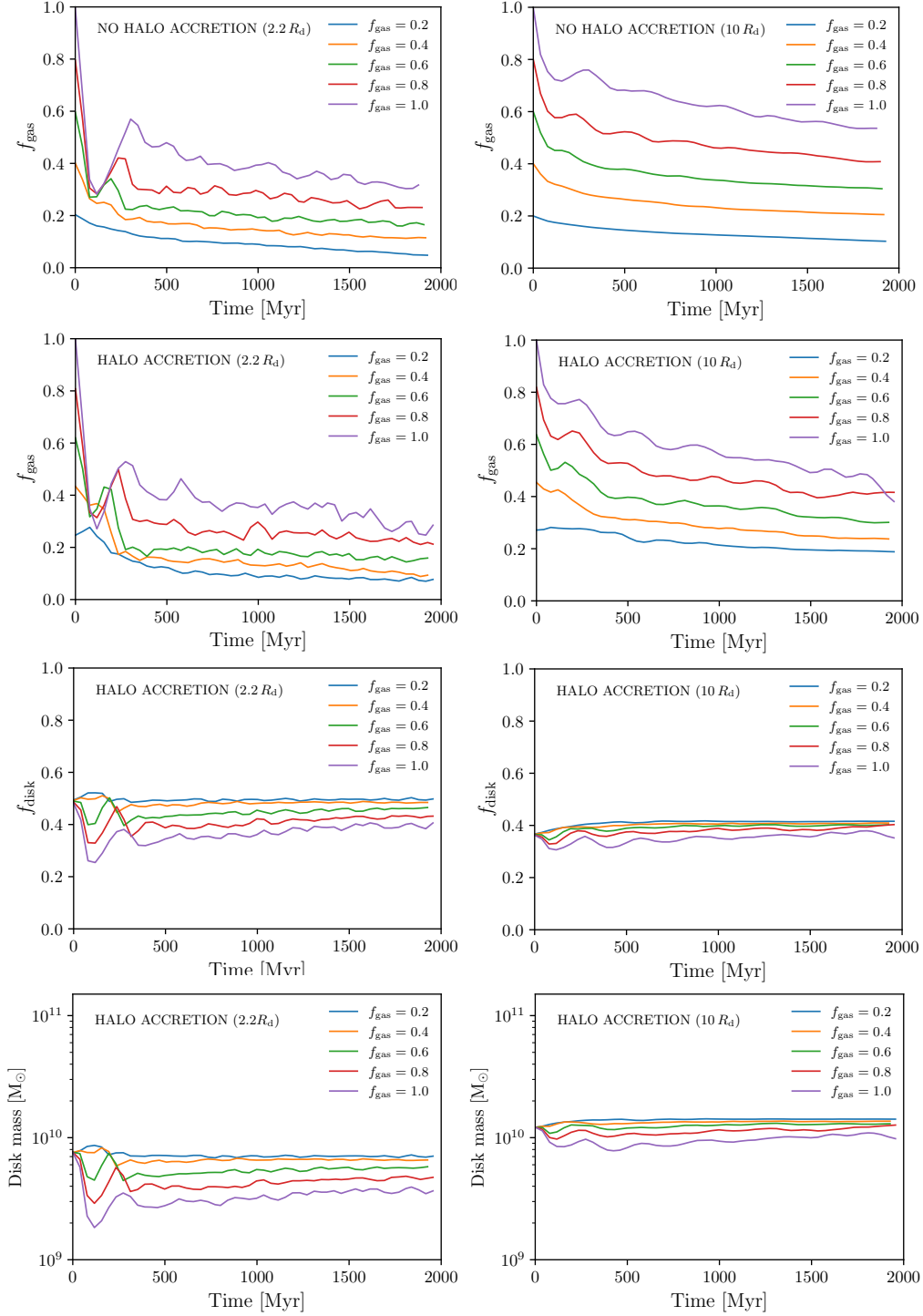


Figure 2. The change in gas fraction, disk mass fraction and disk mass with cosmic time for our heavy disk ($f_{\text{disk}} = 0.5$) simulations. The top row is for “no halo accretion” models; all other rows are for “halo accretion” models, for which there is constant accretion onto the disk plane. Two disk zones are shown: (Left) $R < 2.2 R_{\text{disk}}$; (Right) $R < 10 R_{\text{disk}}$. In each plot, we show the time evolution for 5 different initial gas fractions, as indicated. These are systematically lower in the halo-accretion models, because the enhanced accretion drives more vigorous star formation, which consumes the gas at a faster rate and drives mass-loaded, circulating winds – see Fig. 4. In the bottom two rows, the winds are increasingly more effective at removing disk baryons at higher gas fractions, particularly across the inner disk.

3.1.1. *The star formation rate*

Krumholz & McKee (2005) consider the fraction of the turbulent gas mass in collapsing density fluctuations. In these regions, gravity starts to become a dominant factor, as opposed to turbulence. This defines a critical density for star formation (see Federrath & Klessen 2012, for a comprehensive comparison of different models for the critical density) by comparing the Jeans length with the turbulent sonic scale (Federrath et al. 2021a), which marks the transition from supersonic turbulence on cloud scales, to subsonic turbulence inside the dense star-forming cores and accretion discs. The total star formation rate (SFR) in a gas cloud with mass M_{cl} is thus given by (Krumholz & McKee 2005; Federrath & Klessen 2012)

$$\dot{M}_* = \text{SFR}_{\text{ff}} \frac{M_{\text{cl}}}{t_{\text{ff}}}, \quad (6)$$

where t_{ff} is the freefall (collapse) time within the cloud, and SFR_{ff} is the star formation rate per freefall time, which takes account of the complex fractal hierarchy in a turbulent medium. It is a dimensionless SFR; for example, if $\text{SFR}_{\text{ff}} = 0.1$, then in one freefall time, 10% of the gas mass in the cloud would have formed stars. From fits to simulations, Krumholz & McKee (2005) arrived at

$$\text{SFR}_{\text{ff}} \approx 0.014 \left(\frac{\alpha_{\text{vir}}}{1.3} \right)^{-0.68} \left(\frac{\mathcal{M}}{100} \right)^{-0.32}, \quad (7)$$

where α_{vir} is the virial parameter (ratio of twice turbulent to gravitational energy). Note that SFR_{ff} drops with increasing \mathcal{M} in this model, contrary to the expectation that increasing \mathcal{M} results in a higher dense-gas fraction, and thus higher SFR. Indeed, more recent calculations show that the model provided by Eq. (7) does not fit simulations in which the Mach number (\mathcal{M}) is varied (Federrath & Klessen 2012). This is due to the fact that the Krumholz & McKee (2005) model does not account for the density dependence of the freefall time.

Hennebelle & Chabrier (2011) provide a multi-freefall framework of the SFR, in which the density dependence of the freefall time is taken into account by evaluating it inside the integral that defines SFR_{ff} (Federrath & Klessen 2012). This multi-freefall model of star formation provides excellent fits to numerical simulations with a wide range of different parameters, namely the virial parameter (α_{vir}), the sonic Mach number (\mathcal{M}), the plasma beta (β , or alternatively the Alfvén Mach number), and the turbulence driving parameter (b ; Federrath & Klessen 2012). The strongest dependence of the SFR is on the turbulence driving mode, resulting in differences in SFR_{ff} by as much as an order of magnitude (Federrath & Klessen 2012; Federrath 2018), and in the virial parameter α_{vir} , which can completely shut off star formation at sufficiently high α_{vir} . However, all 4 dimensionless parameters can play a critical role, depending on the exact position in the 4D parameter space. This space is illustrated in a set of figures presented in Federrath & Klessen (2012, see their figure 1).

The full theoretical expression for the multi-freefall turbulence-regulated SFR_{ff} model is given by (Federrath & Klessen 2012)

$$\text{SFR}_{\text{ff}} = \frac{\epsilon}{2\phi_t} \exp\left(\frac{3}{8}\sigma_s^2\right) \left[1 + \text{erf}\left(\frac{\sigma_s^2 - s_{\text{crit}}}{\sqrt{2}\sigma_s^2}\right) \right], \quad (8)$$

with the critical log-density

$$s_{\text{crit}} = \ln \left[(\pi^2/5) \phi_x^2 \alpha_{\text{vir}} \mathcal{M}^2 (1 + \beta^{-1})^{-1} \right]. \quad (9)$$

The log-density dispersion σ_s is given by Eq. (5) and the numerical parameters ϵ , ϕ_t , and ϕ_x are of order of unity, and were determined in Federrath & Klessen (2012) by fitting a set of ~ 30 MHD simulations with varying α_{vir} , \mathcal{M} , b , and β . The star-to-core ratio $\epsilon \sim 0.3\text{--}0.5$ (Federrath et al. 2014), and the best-fit $\phi_t \sim 2$ and $\phi_x \sim 0.2$ (for details, see table 3 in Federrath & Klessen 2012). We return to these ideas in the next section when we examine star formation processes across each of our simulated disks.

Note that for a fixed value of $\text{SFR}_{\text{ff}} = 0.1$, Eq. 6 reduces to the star formation law adopted on a cell-by-cell basis (Eq. 3) in this work. In future work we will explore the galactic scale impact of self-consistently adopting turbulence based star formation models in our AGAMA/RAMSES simulations. Preliminary result of such an approach is presented in section 4.4.3.

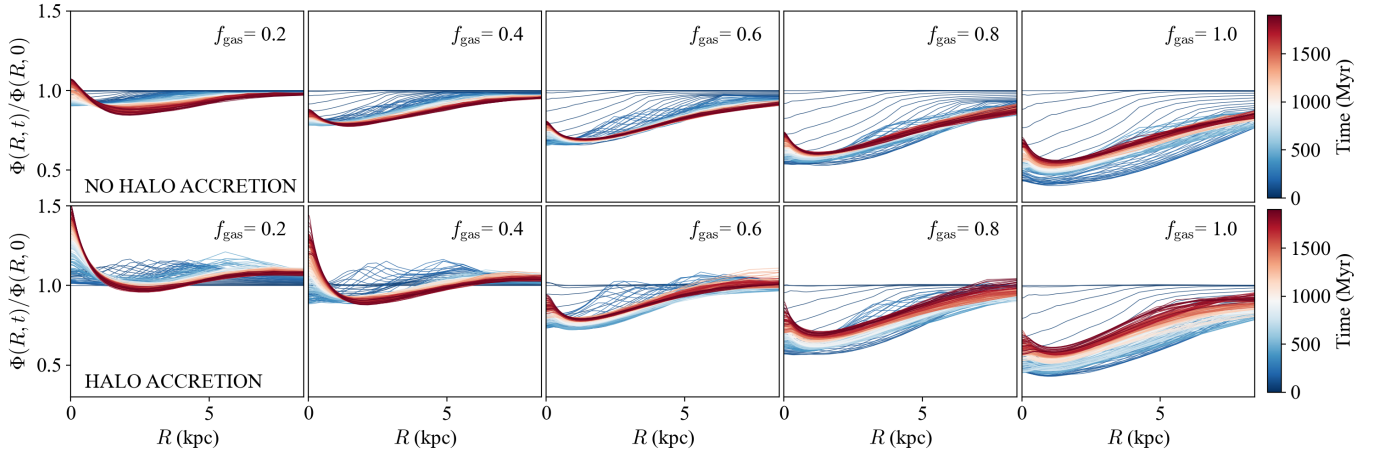


Figure 3. The evolution of the azimuthally averaged, radial profile of the total disk potential $\Phi(R, t)$ with cosmic time, normalised to the starting potential $\Phi(R, 0)$ encoded in colour for (top) no halo accretion, (bottom) halo accretion. Blue tracks are early in cosmic time and red tracks are later times, as indicated. For $f_{\text{gas}} < 0.5$, the disk potential is fairly constant but, above this limit, the loss of gas mass in circulating winds leads to a substantial weakening of the disk potential. Note that the vertical axis is a ratio of gravitational potentials, such that a curve moving downwards reflects a weaker potential.

4. RESULTS: FORMATION OF GASEOUS AND STELLAR BARS

4.1. Milky Way progenitor simulations and general properties

In Table 1, the simulations are grouped into different categories – low resolution, repeated simulations, and high resolution with different initial conditions. All movies are available at our website <http://www.physics.usyd.edu.au/turbo-disks/>. There are 6 types of simulations distinguished by the different initial gas fractions ($f_{\text{gas}} = 0, 20, 40, 60, 80, 100\%$); these are run at low resolution for a total of 2 Gyr because we are focussed on the high-redshift universe ($z \gtrsim 3$).

The filename convention is as follows:

We use `fdXX_fgYY_nac` for “no halo accretion” models, and `fdXX_fgYY_ac` for “halo accretion” models. Here, `XX` is the disk mass fraction percentage and `YY` is the gas fraction percentage. If the simulation has multiple versions generated by different random seeds, the file is referred to as `fdXX_fgYY_nac.ZZ`, where `ZZ` is the version number.

In Fig. 2, we present the evolution of f_{gas} for all 5 gas-rich disk models. The top row presents the models without halo accretion for radii within $2.2R_{\text{disk}}$ and within $10R_{\text{disk}}$. The second row shows the matching results for the halo accretion model. In both models, the gas is cooling from the outset and is characterised by an initial starburst forming stars, before declining rapidly to a lower gas fraction. The bottom two rows show that the disk loses progressively more of its mass after the initial burst as a function of f_{gas} , but then regains some of the mass at later times. The mass loss clearly affects the inner disk (LHS figures) much more than the outer disk (RHS figures). This mass loss is seen more clearly with the evolution of the disk’s gravitational potential (Fig. 3). The radial traces are shown at different times, with blue corresponding to early times, and red curves depicting late times. For $f_{\text{gas}} < 0.5$, the disk potential is fairly constant, but above this limit, the loss of gas mass in circulating winds leads to a substantial weakening of the disk potential.

We also investigate if the initial setup influences the long-term behaviour of the simulations. We explore three different initial equations of state: (i) cooling ($t_{\text{start}} = 0$ Myr); (ii) short-term adiabaticity before cooling ($t_{\text{start}} = 50$ Myr); and (iii) long-term adiabaticity before cooling ($t_{\text{start}} = 400$ Myr). Here, t_{start} is the time at which gas cooling, and therefore heating, star formation and stellar feedback, are switched on. The first case leads to an initial starburst when the gas column density is at its peak; for the other two cases, the initial starburst event is more subdued. The long-term behaviour does not appear to be affected by the initial equation of state.

As we have seen, the gas fractions are systematically lower in the halo-accretion models, compared to the “no accretion” case, which is surprising at first glance. But an examination of the models reveals that the halo accretion drives more vigorous star formation, which consumes the gas at a faster rate, and some of the gas is carried away from

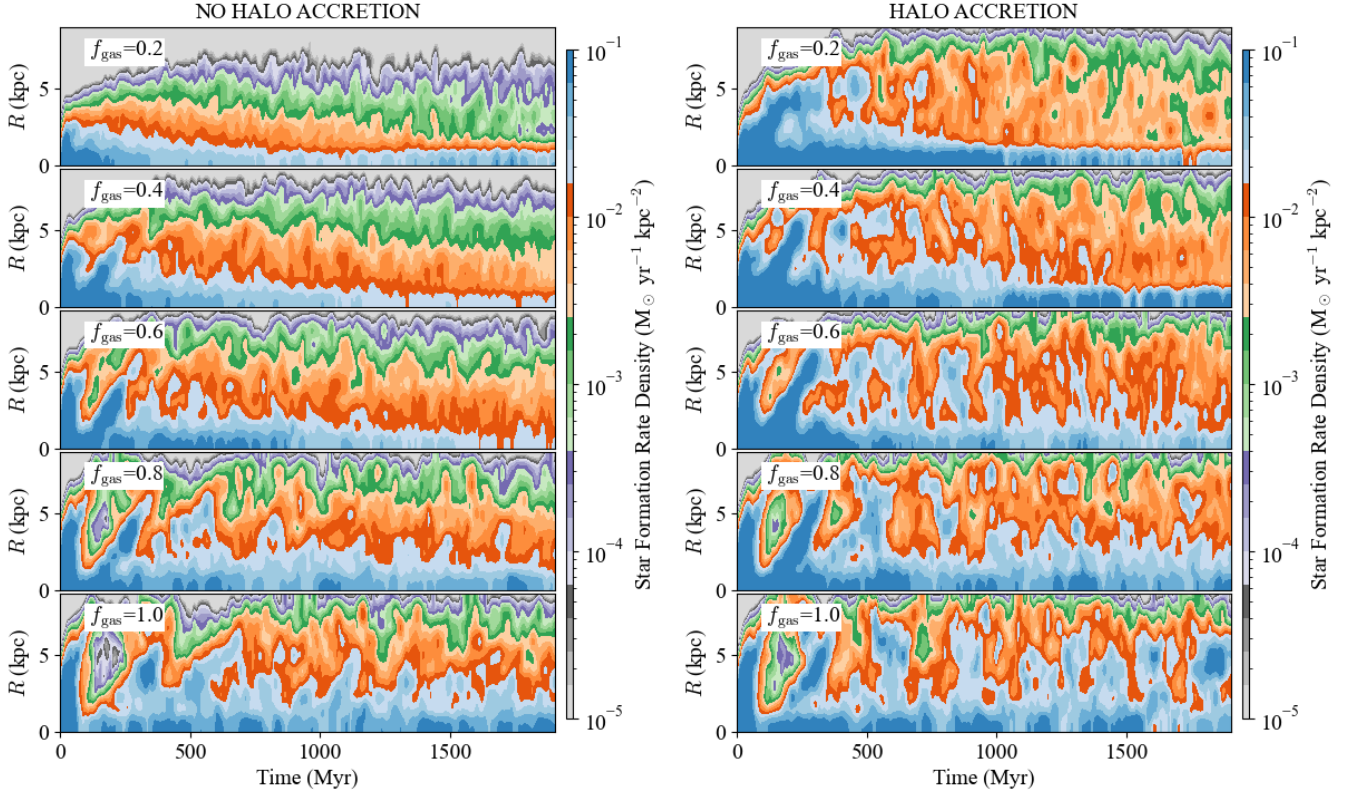


Figure 4. Periodograms drawn from our heavy disk ($f_{\text{disk}} = 0.5$) simulations that capture how the star formation rate (SFR) surface density (in units of $M_{\odot} \text{ yr}^{-1} \text{ kpc}^{-2}$) evolves as a function of radius and cosmic time: (Left) No halo accretion; (Right) Halo accretion. The five rows correspond to different gas fractions, in order from the top, $f_{\text{gas}} = 20, 40, 60, 80, 100\%$. All models commence with a short-lived, disk-wide starburst phase that moves outwards for the first 300 Myr. The higher f_{gas} models sustain a higher SFR surface density on average for both models. The halo-accretion models sustain higher star formation rates for all times compared to the matched “no accretion” model.

the disk. We see this more clearly in the periodograms presented in Fig. 4 by comparing the left and right figures at the same value of f_{gas} . Periodograms simultaneously display the spatial and temporal behaviour of a quantity q . The spatial information is azimuthally averaged, such that a periodogram effectively represents a map $q(R, t)$, e.g. $\Sigma_{\text{SFR}}(R, t)$. It is constructed by calculating a radial profile of q at a given time, and concatenating each of these profiles for all available time steps.

All of the models in Fig. 4 show high levels of burstiness and intermittent behaviour, becoming increasingly so at higher gas fraction. The models with the highest gas fractions exhibit other forms of intermittent behaviour, including spiral arms and bar-like structures that come and go. For this reason, we run the $f_{\text{gas}} = 40\%$ model three times with different random seeds to give us a better insight into the effects of stochasticity. (These models are `fd50_fg40_noacc.01`, `fd50_fg40_noacc.02` and `fd50_fg40_noacc.03`.) If the simulations are synchronized, we see how each of the models develop multiple flocculent spiral arms at different times, before they all settle into the bar-dominated phase within about 500 Myr. These are noisy systems.

4.2. Gaseous and stellar velocity dispersions

In Fig. 5, we present the vertical kinematic dispersions σ_z for all 5 gas-rich disk models measured through the simulated disks (averaged in azimuth) as a function of radius and time. Once again, the radial traces are shown at different times, with blue corresponding to early times, and red curves depicting late times. The top and bottom collages correspond to the “no halo accretion” and “halo accretion” models respectively. The left column shows the predicted results for cold gas ($T_{\text{gas}} < 10^3 \text{ K}$) and, in all cases, the vertical kinematics settle down to less than $\sigma_{z, \text{gas}} \approx 20$

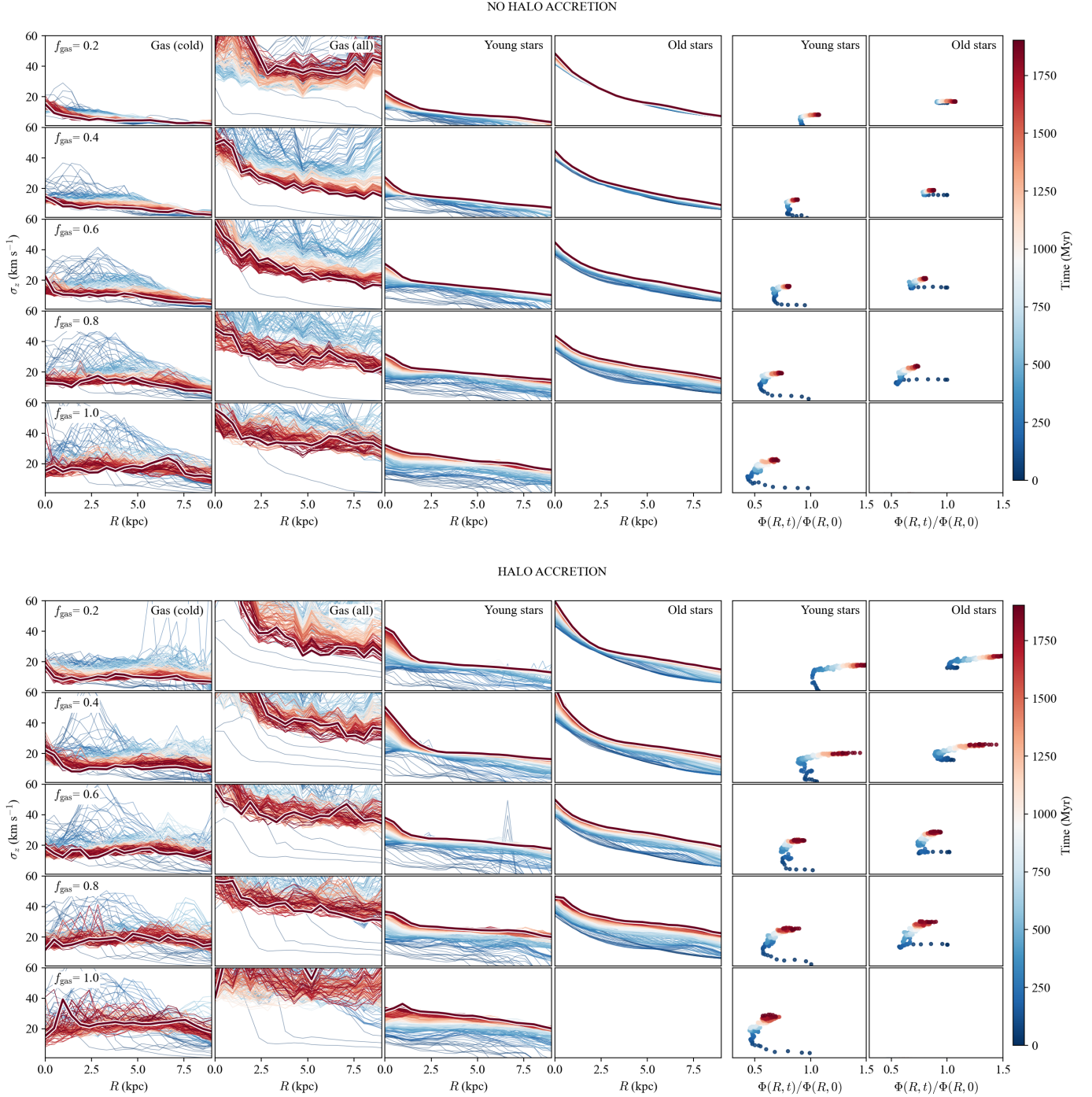


Figure 5. The evolution of the azimuthally averaged, vertical kinematic dispersion σ_z with radius for all disk components: (top) no halo accretion, (bottom) halo accretion. Blue tracks are early in cosmic time and red tracks are later times. Within each collage, we show the evolution for all gas fractions: columns (1) cold gas, (2) all gas, (3) young stars, (4) pre-existing stars. The gas dispersions settle down from initially high values; interestingly, the stellar dispersions show the opposite trend. In columns (5) and (6), the stellar σ_z has a strong dependence on the depth of the disk’s potential (see Fig. 3) as a function of time (see text). The disk potential is weakening as points move to the left due to baryon mass loss.

km s^{-1} from a high of twice that value within a gigayear. For the halo accretion models, the settling dispersion is $20 - 40 \text{ km s}^{-1}$ at the highest gas fractions.

Interestingly, in line with the observations, the warm gas dispersions are systematically higher, and for all time. As already mentioned, gas dispersions measured with cool molecular lines tend to be narrower than dispersions measured with emission lines arising from warm gas, regardless of the galaxy’s redshift (e.g. Ejdetjärn et al. 2022). For the “no halo accretion” models, the dispersions are a factor of two higher. The “halo accretion” models are systematically higher still, mostly driven by the stronger disk-halo circulation seen in all the higher f_{gas} models. Unlike the cold gas, this material is not in dynamical equilibrium. There are strong vertical wind flows in these models out to tens of kiloparsecs - we refer the reader to the movies on our website. Furthermore, the cool gas mass is typically larger than the warm gas mass, and therefore is more representative of the disk dynamics.

In Fig. 5, the unexpected result is what is seen to occur with the vertical stellar dispersions, both for pre-existing stars and stars born within the gas in columns (3) and (4). In particular, the young stars are rapidly and kinematically heated from an initially very cold disk to a much warmer stellar disk. This does not reflect the high initial gas dispersions seen in the cold gas; these have exactly the opposite trend with time. Furthermore, the old stars are also heated at a time when the cold gas dispersions are settling down. Columns (5) and (6) illustrate how the vertical dispersion σ_z varies as the disk potential initially declines and then climbs again. We provide a novel interpretation of what is going on here in a later section (Sec. 5.3).

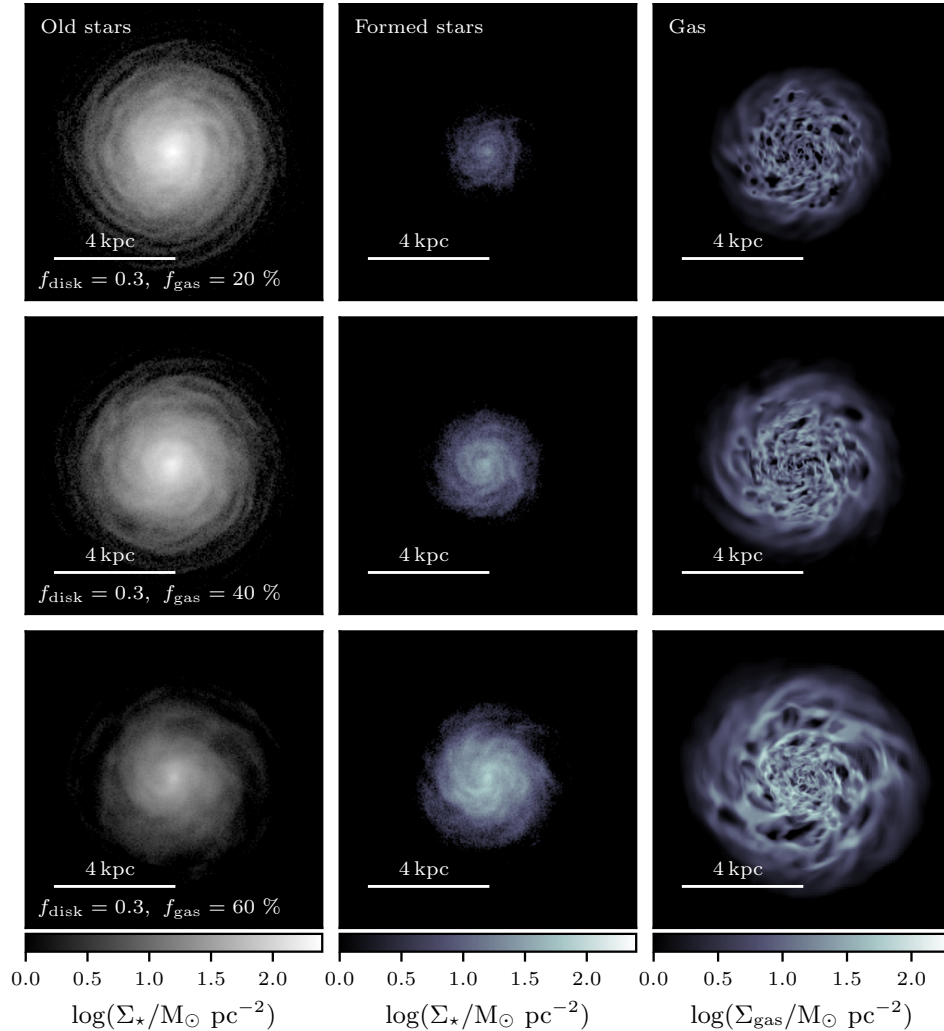


Figure 6. Final snapshots taken from three of our simulations in the low $f_{\text{disk}} (=0.3)$ limit. The gas fractions from top to bottom are $f_{\text{gas}} = 20\%$, 40% and 60% ; the pre-existing (old) stellar population has a smaller contribution, as we move to higher f_{gas} , to maintain a constant disk mass. Even after 2 Gyr, a gas-rich disk does *not* form a bar in contrast to what happens in heavy disks. The box scale is 10×10 ckpc. The *total* (stars+gas) disk baryon fraction f_{disk} is the primary agent that determines the onset timescale of the bar; f_{gas} becomes important only in the high f_{disk} limit (see text).

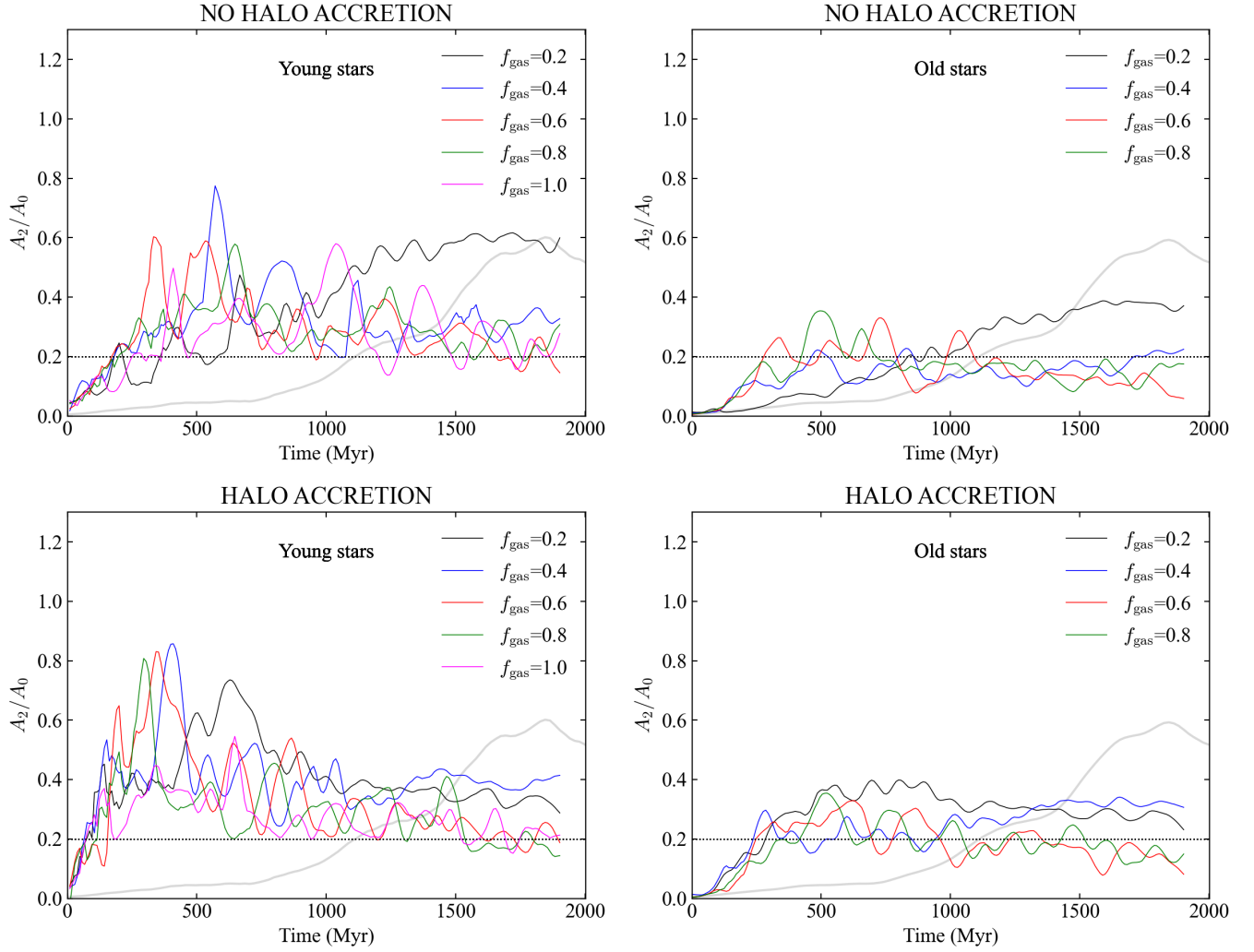


Figure 7. The evolution of A_2/A_0 in the surface density maps for (top) the “no accretion” models shown in Fig. 8, (bottom) the “halo accretion” models shown in Fig. 9. These correspond to $f_{\text{disk}} = 0.5$ models; the coloured lines represent the different gas fractions as shown: (left) the young stellar disk, (right) the pre-existing stellar disk ($f_{\text{gas}} = 100\%$ not applicable). The grey line shows the bar emergence for the gas-free ($f_{\text{gas}} = 0$) simulation. The presence of turbulent gas speeds up the formation of the bar in all cases, but note that most bars are weaker than their gas-free counterpart, and appear to fade at the highest gas fractions. The horizontal dotted line is the widely used, minimum threshold ($A_2/A_0 = 0.2$) for the existence of a bar in an N-body simulation.

4.3. Does gas help or hinder the formation of bar-like distortions?

This is an age-old question that has never really been tackled in galactic dynamics, particularly in the presence of star formation and turbulent gas in the limit of high gas fraction. Since the JWST discovery of well-developed stellar bars in turbulent, gas rich disks at $z \sim 2$ (Guo et al. 2022; Costantin et al. 2023), this has become a topic of renewed interest. For earlier works that include gas, only a narrow range in gas fraction is treated and few consider prescriptions for star formation. Notable studies that do consider star-forming disks are Berentzen et al. (2007) and Seo et al. (2019), but for these models, $f_{\text{gas}} \lesssim 10\%$. One study suggests that the presence of gas reduces a *stellar* bar’s lifetime (Villa-Vargas et al. 2010) or at least weakens it (Athanasoula et al. 2013). The lifetime of gaseous bars has never been considered, to our knowledge.

We believe our current framework is the ideal platform to treat bar formation in gas-rich disks. We perform simulations in the low (light) and high (heavy) disk baryon fraction limit, with a range of gas fractions. First, we show that the answer depends on whether disk baryons do or do not dominate the inner galactic potential. Gas appears to

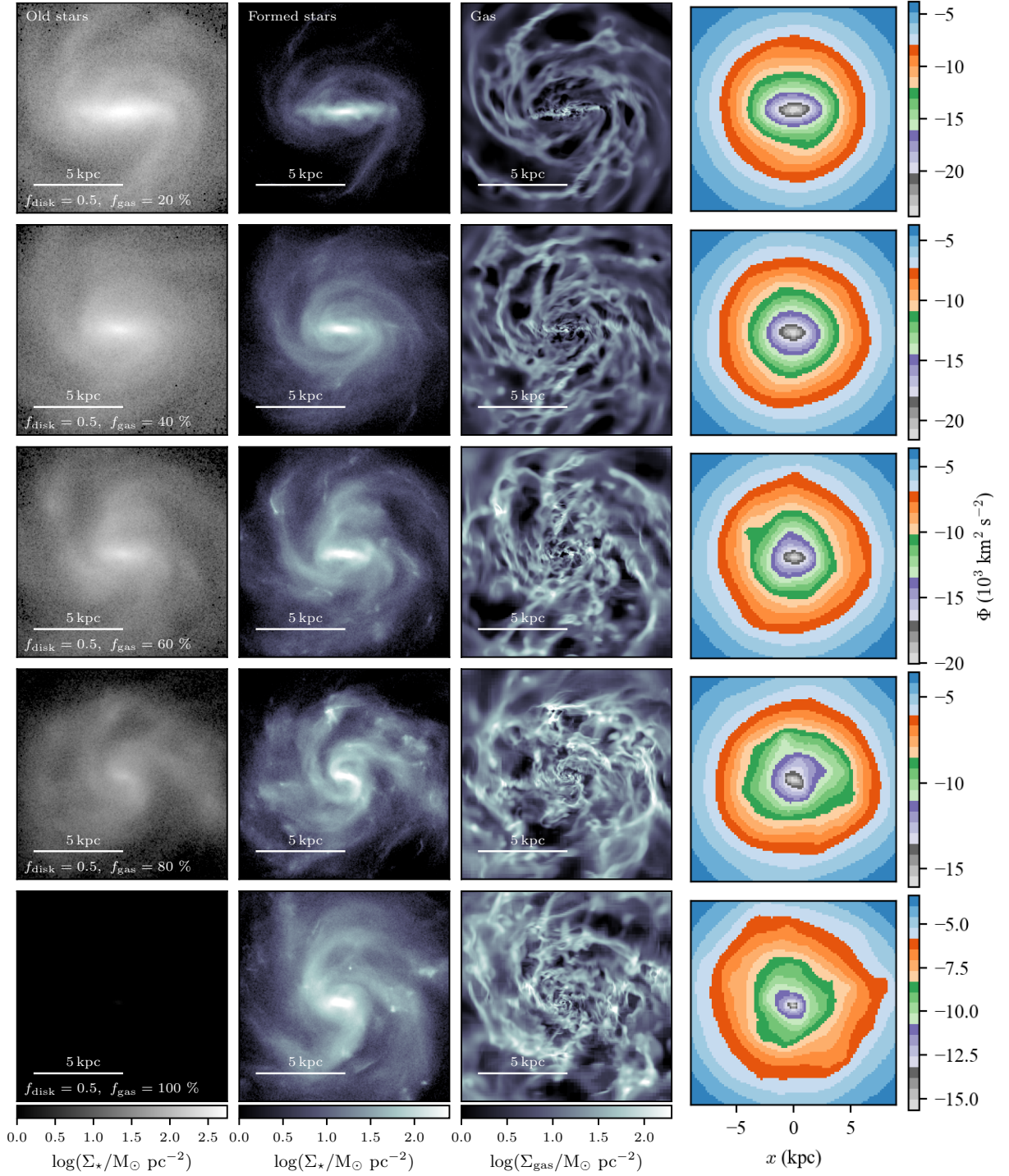


Figure 8. The five rows correspond to a single snapshot in time ($t_o = 2$ Gyr) taken from five $f_{\text{disk}} = 0.5$ simulations without halo accretion, in order from the top, $f_{\text{gas}} = 20, 40, 60, 80, 100\%$. The box scale is 12×12 ckpc (comoving kpc). There is *no* halo accretion active here. The columns are: (1) surface density of pre-existing stars, (2) surface density of created stars, (3) gas surface density, (4) total gravitational potential. In the top three cases, the gas and young stellar bars survive for the full length of the simulation (2 Gyr). For the highest gas fractions, spiral arms are more diffuse, and bars are smaller and collapse to form bulges in the next timestep ($t_o \approx 1.3$ Gyr). Radial shear flows are active in all cases, being strongest at low gas fraction (see Fig. 11). These phenomena are clearly seen in the movies referenced in the main text.

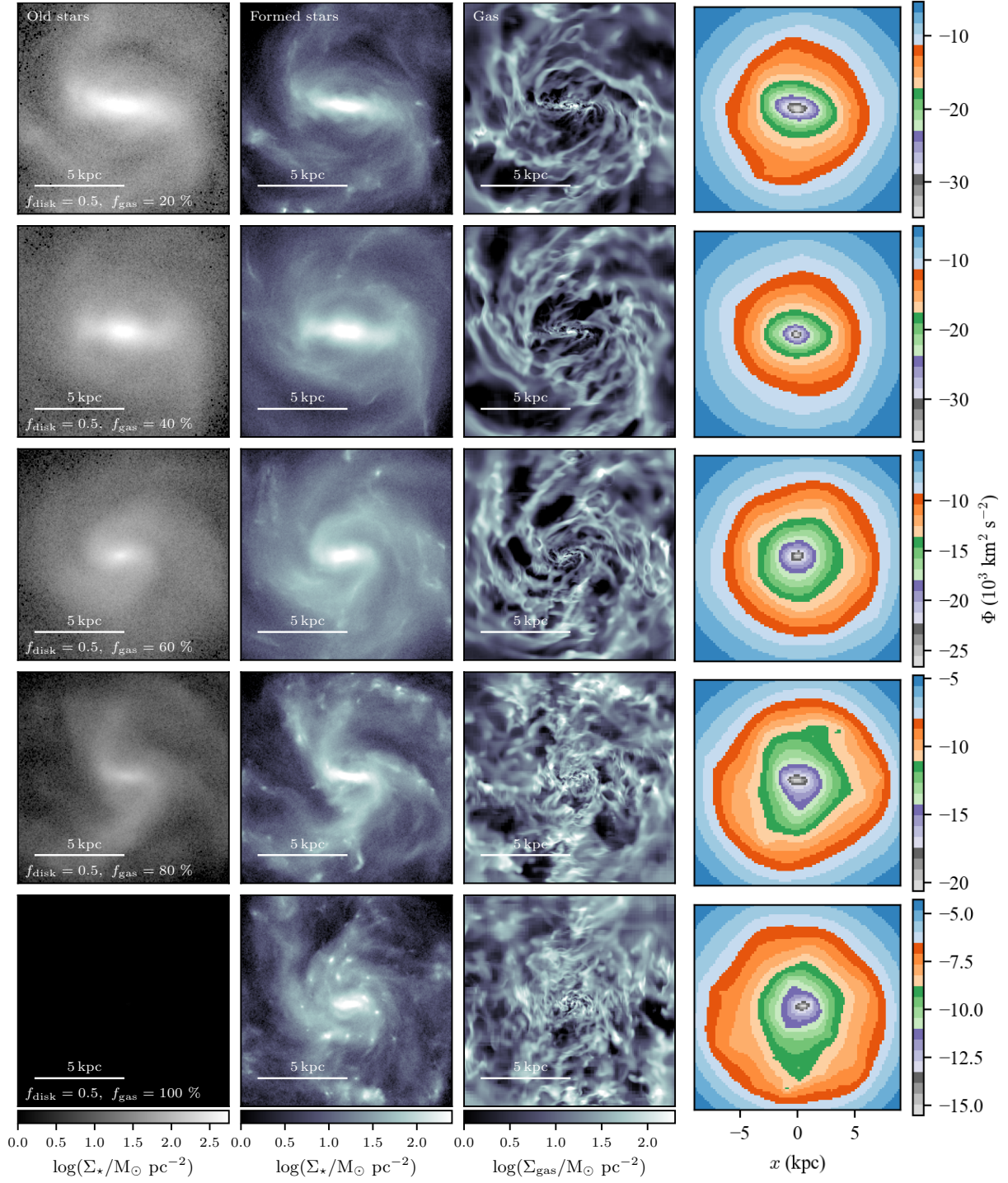


Figure 9. Same as Figure 8, but for simulations *with* halo accretion.

have minimal influence on bar formation when the disk is light, a conclusion that seems to hold for low or high gas fractions.

4.3.1. Light disks

In Bland-Hawthorn et al. (2023), we extend the earlier work of Fujii et al. (2018) to confirm the discovery of an inverse relation – which we refer to as the Fujii relation – between the stellar bar formation time τ_{bar} and the disk baryon fraction f_{disk} . Fujii et al. (2018) found that the higher the value of f_{disk} , the shorter the timescale for the onset of the bar instability. With sufficient disk resolution, this result is largely independent of the number of particles used to sample the density distribution (Fujii et al. 2019; Bland-Hawthorn et al. 2023).

For f_{disk} evaluated at $R = R_s$, Fujii established that the dividing line occurs at $f_{\text{disk}} \approx 0.3$, in the sense that smaller values lead to bar formation timescales that exceed a Hubble time. They also find that there is an asymptotic limit to the bar formation timescale such that, in the limit of high f_{disk} , there is a finite *minimum* timescale for bar formation of order $1 - 2$ Gyr.

In the low f_{disk} limit ($f_{\text{disk}} = 0.3$), we run simulations with $f_{\text{gas}} = 0, 0.2, 0.4, 0.6$. These models are dubbed `fd30_fg20_nac`, `fd30_fg40_nac` and `fd30_fg60_nac` at our website. Since this work is primarily concerned with high-redshift discs ($z \gtrsim 3$), the expensive simulations are restricted to 2 Gyr. In all simulations shown in Fig. 6, we see that a bar does *not* form within 2 Gyr, thus confirming that bar formation is still suppressed in the light disc limit, even in the presence of a high gas content. *This is an important result.* Regardless of what makes up the disk baryons, it must dominate the local potential to form a stellar bar, or any bar-like distortion. By comparison, in heavy disks ($f_{\text{disk}} \gtrsim 0.5$), internally triggered, *stellar* bars form in $1 - 2$ Gyr (Fujii et al. 2018, 2019; Bland-Hawthorn et al. 2023), an issue we return to below.

4.3.2. Heavy disks

Our approach to exploring the role of gas is to run simulations over a range of gas fractions when the disk dominates, and to examine the bar strength and survival time, as illustrated in Fig. 7. But as the gas fraction increases, the role of any stellar bar becomes less important, so we consider the prospect of gas bars and/or young stellar bars that may form within them.

We now examine the simulations in more depth. They are investigated using analytic methods that have become fairly routine (e.g. Elmegreen & Elmegreen 1985; Rix & Zaritsky 1995). Bisymmetric disturbances are detected in both the surface density and kinematic maps; the latter are particularly useful in turbulent media. At each timestep, a Fourier decomposition is performed on the surface density of the simulated disk, such that

$$\frac{\Sigma(R, \phi)}{\Sigma_0} = \frac{1}{A_0} \sum_{m=0}^{\infty} A_m(R) e^{im[\phi_0 - \phi_m(R)]} \quad (10)$$

for which $A_m(R)$ and $\phi_m(R)$ are the Fourier amplitude and phase angle for the m th mode at a radius R , and Σ_0 is the central surface density. In our simulations, $m = 2$ is the dominant mode when the bar emerges.

Fujii et al. (2018) define $\tau_{\text{bar},0.2}$ as the timespan between the initial state of an unbarred synthetic galaxy, and the epoch at which the maximum normalised amplitude of the quadrupole moment (Fourier $m = 2$ mode), commonly referred to as A_2/A_0 , crosses the (arbitrary) threshold value of 0.2. Once again, we adopt Fujii’s A_2/A_0 threshold criterion. The method used by Fujii et al. (2018) to measure the Fourier amplitudes was not specified. To calculate A_2/A_0 and ϕ_2 , we adopt the algorithm described in and the corresponding code provided by Dehnen et al. (2023). In brief, they implement an automated identification of the bar region (subject to a number of tunable parameters) using the disk particles, and perform the discrete Fourier decomposition of the particle density within the bar region using an iterative procedure to calculate the azimuthal harmonics.

In Fig. 7, the evolution of A_2/A_0 is presented for a heavy disk with five different gas fractions. The models are dubbed `fd50_fg20_nac`, `fd50_fg40_nac`, `fd50_fg60_nac`, `fd50_fg80_nac` and `fd50_fg100_nac` at our website; in both panels, the grey line refers to the gas-free model, `fd50_fg00_nac`. For $f_{\text{gas}} = 20\%$, we see from both panels that the bar onset occurs in half the time, or about 600-800 Myr depending on the stellar population considered. While the trends are frenetic, the bar strength appears stronger and the bar onset is faster (300-600 Myr) for the young stars compared to the old stars. Interestingly, the bar strength appears to slowly fade for both young and old stars for the highest gas fractions, in agreement with Athanassoula et al. (2013), although the latter bars took *longer* to form with the inclusion of gas.

The evolutionary tracks in Fig. 7 were drawn from the models presented in Figs. 8 and 9. In the latter figures, which corresponds to the snapshots where the young bar is strongest in each case, the top three rows reveal well-pronounced young stellar bars, all of which show signs of a strong radial shear flow, evident in the density map, but particularly prominent in the stellar/gas kinematics (see below). These bars all form within about 300-600 Myr and survive for

the full length of the simulation (~ 2 Gyr). The bar length correlates with the gas fraction, such that the bar radius is about 3 ckpc (comoving kpc) for $f_{\text{gas}} = 20\%$, declining to about 1 ckpc in the high f_{gas} limit. The bars in both of the highest gas fraction simulations collapse to form bulges shortly after the timestep shown.

Thus we find that f_{gas} is found to have a secondary, but important, role in the presence of a heavy disk, and obviously a primary role when the stellar content is close to zero. The fact that turbulent gas accelerates bar formation, compared to *inert* gas that seems to delay the process (e.g. Athanassoula et al. 2013; Bland-Hawthorn et al. 2023), requires an explanation. An overarching theme of the simulations, when viewed as a whole, is that higher gas fractions lead to noisier and clumpier galaxies. Our expectation is that the increasing noise levels in the gas imparts the same or similar perturbations on the evolving stellar disk. We explore this idea in the next section.

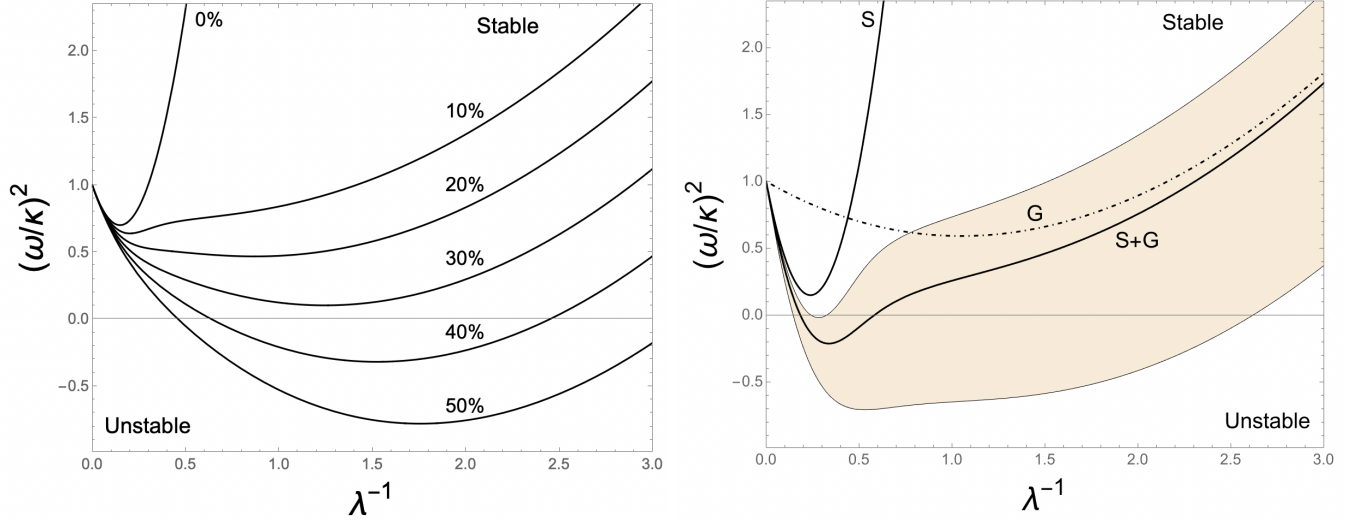


Figure 10. (Left) Square of the normalized oscillation frequency (ω^2/κ^2) vs. inverse wavelength (λ^{-1}) of the perturbation (in units of kpc^{-1}). The different curves show the degree of stability for different gas fractions f_{gas} . The upper region ($\omega^2/\kappa^2 > 0$) is largely stable; the lower region ($\omega^2/\kappa^2 < 0$) is where perturbations grow exponentially. (Right) The different contributions from stars only (S) and gas only (G) to the overall two-fluid stability. Individually, they appear stable, but when co-existing, the two-fluid medium is more unstable (S+G). The shaded region illustrates the changing conditions in the S+G combined fluid when the local gas surface density varies by a factor of two, as in a turbulent medium.

4.3.3. Instabilities in star-gas fluids

We have seen that increasing the gas fraction (f_{gas}) in the disk makes the disk increasingly unstable, and excites low order modes that lead to stellar/gas bars on shorter timescales compared to gas-free (single fluid) disks. The growth of gravitational instabilities in a fluid has played a role in galactic dynamics since the 1960s (q.v. Binney & Tremaine 2008). Several authors have suggested that the solar neighbourhood should be relatively stable, but even small perturbations on the assumed parameters can lead to very different growth rates (e.g. Rafikov 2001). This effect is amplified when one considers the gravitational interaction of two fluids, particularly when one is dynamically colder or more viscous than the other. Both fluids can be separately stable, but then rendered unstable by “the additional gravitational self-energy in the system resulting from the gravitational interaction between the two fluids (Jog & Solomon 1984, see also Romeo 1992).”

Perturbations propagate in space and time. In linear analysis, for any physical property under study, there is a factor $\exp[i(kr + \omega t)]$ where ω is referred to as the angular frequency and k is the wavenumber of the perturbation with wavelength λ ($k = 2\pi/\lambda$). After using Poisson’s equation to treat perturbations in the gravitational potential, Jog & Solomon (1984) arrive at a quadratic dispersion relation with solutions

$$\omega^2(k) = \frac{1}{2} \left((\alpha_\star + \alpha_{\text{gas}}) \pm \sqrt{(\alpha_\star + \alpha_{\text{gas}})^2 - 4(\alpha_\star \alpha_{\text{gas}} - \beta_\star \beta_{\text{gas}})} \right). \quad (11)$$

The subscripts “ \star ” and “gas” refer to the stellar and gas fluids; the variables are as follows:

$$\beta_{\star} = 2\pi G k \mu_{\star} \mathcal{R}_{\star} \quad (12)$$

$$\beta_{\text{gas}} = 2\pi G k \mu_{\text{gas}} \mathcal{R}_{\text{gas}} \quad (13)$$

$$\alpha_{\star} = \kappa^2 + k^2 c_{\star}^2 - \beta_{\star} \quad (14)$$

$$\alpha_{\text{gas}} = \kappa^2 + k^2 c_{\text{gas}}^2 - \beta_{\text{gas}} \quad (15)$$

where \mathcal{R}_{\star} and \mathcal{R}_{gas} are the so-called reduction factors that correct for the different vertical scaleheights of the disks (see below). The positive root describes stable oscillatory perturbations; the negative root considers the transition from stable ($\omega^2 > 0$) to unstable modes ($\omega^2 < 0$). The in-plane epicyclic frequency κ recognizes that the differential disk rotation influences the fluid instabilities. The two fluids (with thermal sound speeds c_{\star} and c_{gas}) have local surface densities μ_{\star} and μ_{gas} . The stellar “sound speed” is usually taken as the local radial velocity dispersion. The dispersion relation for ω^2 is solved in terms of k , or equivalently $1/\lambda$ as we show in Fig. 10, where ω^2 is made dimensionless by normalizing to κ^2 .

In Fig. 10 (left), the increasing trend towards instability is clear as the gas fraction f_{gas} increases. Here, we adopt $\mu_{\text{total}} = 10^8 \text{ M}_{\odot} \text{ kpc}^{-2}$, $\kappa = 36 \text{ km s}^{-1} \text{ kpc}^{-1}$, $c_{\star} = 35 \text{ km s}^{-1}$ and $c_{\text{gas}} = 5 \text{ km s}^{-1}$, inspired by the solar neighbourhood values considered by Jog & Solomon (1984). As presented, this figure gives the false impression that low gas fractions are everywhere stable. These curves correspond to average values and do not treat local variations.

In Fig. 10 (right), we look at the two-fluid system in more detail. The gaseous (G) and stellar (S) fluids are independently stable, but when considered together (S+G), they are much less so, particularly on scales of 2 – 3 kpc, due to their mutual interaction. The curves shown assume $f_{\text{gas}} = 20\%$ and correct for the scale-height differences between the two fluids, as presented by Jog & Solomon (1984, Eq. (23)). The reduction factors are

$$\mathcal{R}_{\star} = (1 - \exp(-kh_{\star}))/kh_{\star}, \quad (16)$$

$$\mathcal{R}_{\text{gas}} = (1 - \exp(-kh_{\text{gas}}))/kh_{\text{gas}}. \quad (17)$$

Here we adopt exponential scale heights of $h_{\star} = 300 \text{ pc}$ and $h_{\text{gas}} = 75 \text{ pc}$, otherwise using the same parameters above, except the total surface density is now doubled in line with Jog & Solomon (1984) and our models, i.e. $\mu_{\text{total}} = 2 \times 10^8 \text{ M}_{\odot} \text{ kpc}^{-2}$. Note how the quadratic “stars only” curve has now moved closer to the instability region – compared to the left panel, in line with the Toomre Q criterion in Eq. 19 and its inverse dependence on the surface density.

In Fig. 10 (right), the shaded region illustrates the changing conditions arising when the local gas surface density varies by a factor of two. The shaded area grows larger as f_{gas} increases. In our models, the turbulent medium drives large fluctuations in the local gravitational potential. *These fluctuations are imposed on the stars and explain the faster onset of the bar when gas becomes important.*

We refrain from a more detailed analysis at this time, in particular, a study of 3D instabilities associated with cloud formation and their comparison with 2D instabilities affecting the disk (see e.g. Romeo et al. 2010 on how turbulence scaling relations affect disc stability). Partial (Jeans-like) 3D instabilities are possible even when 2D instabilities are suppressed. In fact, this is evident when watching the development of the most massive clumps in the low f_{gas} simulations (cf. Fig. 10). An excellent updated review and analysis of these distinctions is given in Meidt (2022).

4.3.4. Summary

In summary, we conclude that what fundamentally drives bars to form is f_{disk} , i.e. the *total* disk baryon content, with f_{gas} having no strong influence for light disks. Conversely, the story is very different for heavy disks, where a new mechanism appears to be at play in the presence of a high gas fraction. Gas fractions higher than about $f_{\text{gas}} \gtrsim 10\%$ appear to speed up the onset of a bar, contrary to what is reported elsewhere albeit for lower gas fractions (Berentzen et al. 2007; Athanassoula et al. 2013). The difference may be due to our more realistic treatment involving star formation, where the new stars contribute to the non-dissipative component in the disk. Interestingly, Robichaud et al. (2017) found that, in the presence of AGN feedback, bars form earlier for higher f_{gas} . It is not obvious why feedback processes (AGN or star formation) are able to speed up bar formation. But, as we discuss in Sec. 4.3.3, turbulent energy tends to introduce fluctuations in the local gravitational potential, and these drive accelerated exponential growth in the density perturbations.

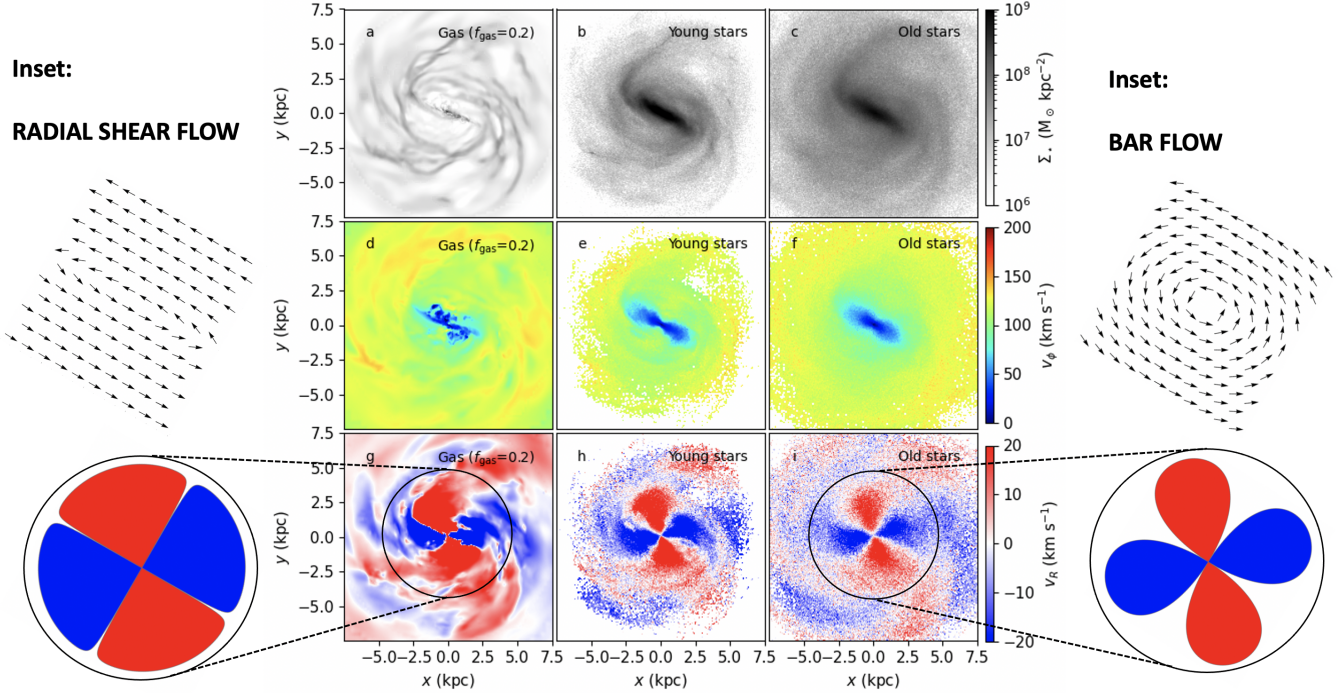


Figure 11. A collage showing the surface density and kinematic maps at $t_o = 2$ Gyr for our model with $f_{\text{disk}} = 50\%$ and $f_{\text{gas}} = 20\%$. In the top row, from left to right, the projected surface density is shown for gas, newly created stars and pre-existing (old) stars. In the middle row, we present the tangential velocity v_ϕ , and in the bottom row, the radial velocity v_R . The developing bar is particularly prominent at late times in the stellar components. The expected quadrupolar signature (“quatrefoil”) is prominent in v_R although the patterns are different for the gas and the old stars, as illustrated by the colour insets. These arise from different flow patterns as indicated: the radial shear flow on the left, and the bar flow on the right. The (saturated) encircled schematics correspond to the circular regions indicated in the bottom row.

4.4. The emergence of bar-like distortions in turbulent gas

4.4.1. Radial shear flow

The top row of Fig. 8 presents a snapshot of the “no accretion” model for $f_{\text{gas}} = 20\%$ at $t_o = 2$ Gyr; we explore these results in more detail in Fig. 11. As the movies reveal, newly formed stars emerge into what appears to be an extreme ‘bar-like’ flow, or a radial shear flow. This is best seen by watching the simulation `fd50_fg20_nac` at our website, although a similar mechanism is clearly operating in `fd50_fg40_nac` and `fd50_fg60_nac`. After a few disk rotations, a differentially rotating, gas-rich turbulent disk develops a pile-up of turbulent gas in two opposing streams. The flow appears to operate with or without an underlying stellar bar, although the flow is strongest at low f_{gas} when there is a stellar bar present.

In Fig. 11, the radial velocity of the gas v_R has a distinctive pattern. This radial shear flow is long-lived, tumbles with the disk’s rotation and gives rise to a kinematic “quatrefoil” pattern that is more extreme than seen in normal bar-driven flows. In particular, compare the LHS and RHS insets: the vector flow patterns for both kinds of flow are also presented in Fig. 11 (see insets). The equivalent maps for $f_{\text{gas}} = 40, 60, 80, 100\%$ are included at our website in the interests of brevity.

In Fig. 12, we repeat the top three models in Fig. 8, but this time they correspond to disks characterised by $f_{\text{disk}} = 0.7$, the heaviest disks we have simulated to date. These models are dubbed `fd70_fg20_nac`, `fd70_fg40_nac` and `fd70_fg60_nac` at our website. The bar is longer and stronger, and the radial shear flow is even more pronounced. The terminator line between the two flows is particularly evident in the top right panel in Fig. 8; it appears as a thin, horizontal enhancement of gas about 4 ckpc in length centred on the galaxy. The terminator is also evident in panel ‘d’ of Fig. 11 as a thin blue strip with $v_\phi \approx 0$, i.e. a radial gas stream with no circular motions in the rest frame of the flow.

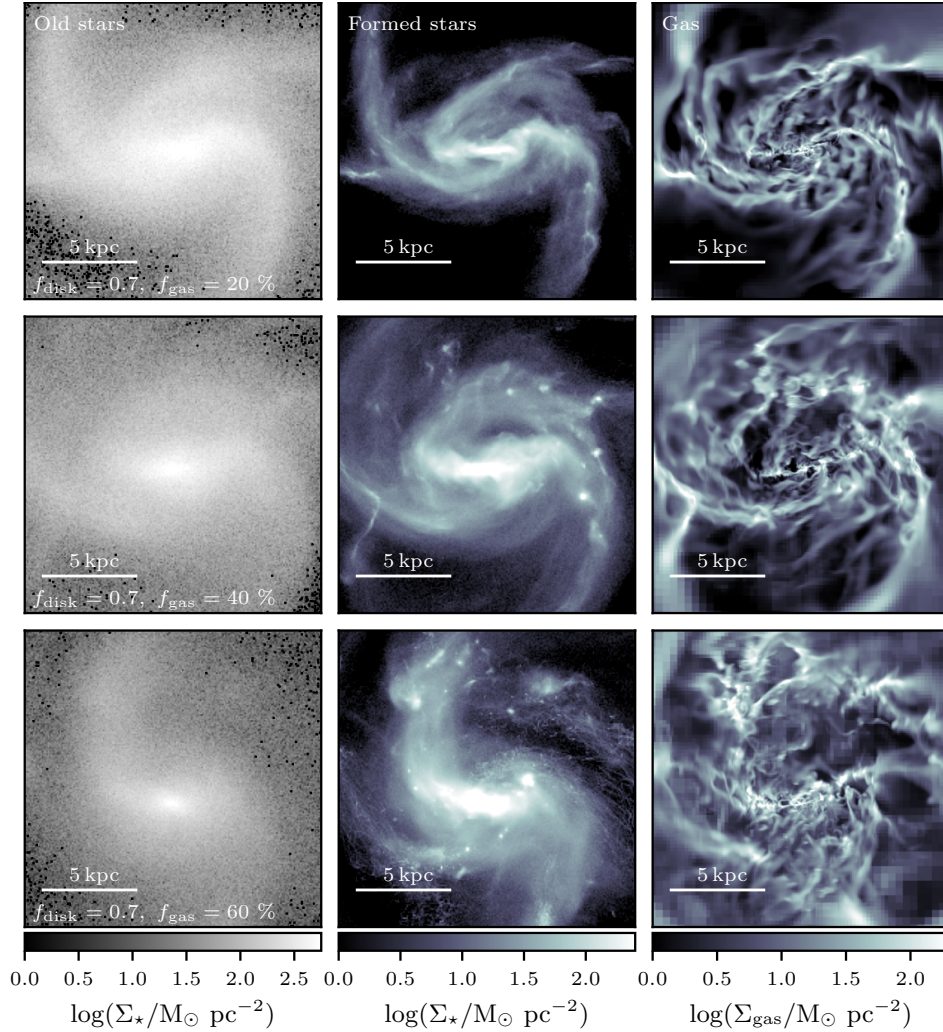


Figure 12. The three rows correspond to a single snapshot in time taken from three $f_{\text{disk}} = 0.7$ simulations, in order from the top, $f_{\text{gas}} = 20, 40, 60\%$. The box scale is 16×16 kpc. There is *no* halo accretion active here. The columns are: (1) surface density of pre-existing stars, (2) surface density of created stars, (3) gas surface density. Compared to Fig. 8, these disks are even more dominant, and the implied gas content (by mass) is higher. Here, we observe very large bar-like distortions and strong radial shear flows that form earlier than for lighter disks.

The roiling action of this radial shear flow is clearly seen by watching the simulation `fd70_fg20_nac` at our website. Heavy, turbulent disks manifest this extraordinary behaviour, leading to kinematic signatures that are somewhat different from radial bar streaming in the local Universe. These signatures may be observable in future high-resolution observations.

4.4.2. What causes the radial shear flow?

In all simulations, the character of the stellar/gas bar is complicated, exhibiting a variety of non-axisymmetric morphologies at different evolutionary stages. Interestingly, at times the bar potential is distinctly dumbbell-shaped, as predicted by Barnes & Tohline (2001). This may be a feature of early bars where a bulge has yet to form. In later work, we examine the stellar orbit families in more detail, but generally we observe a behaviour that is complex. In classical references (e.g. Binney & Tremaine 2008), we learn that many of the inner orbits are boxy, defined by three different frequencies in R , ϕ and z and some orbits can move arbitrarily close to the galactic centre. Other orbits are more chaotic and can cross the bar axis several times in each orbit. The tube orbits typically lie beyond the bar region.

Fig. 13 presents a toy model to illustrate this point. We examine a range of bar potentials suggested in the literature for a Hamiltonian with the form $\mathcal{H}_J(\mathbf{q}, \mathbf{p}) = \frac{1}{2}p^2 + \Phi_{\text{eff}}(\mathbf{q})$ where \mathbf{q} is the position vector and \mathbf{p} is the momentum vector. In the absence of a strong bulge, a dumbbell-shaped potential is often seen in our simulations. We adopt the

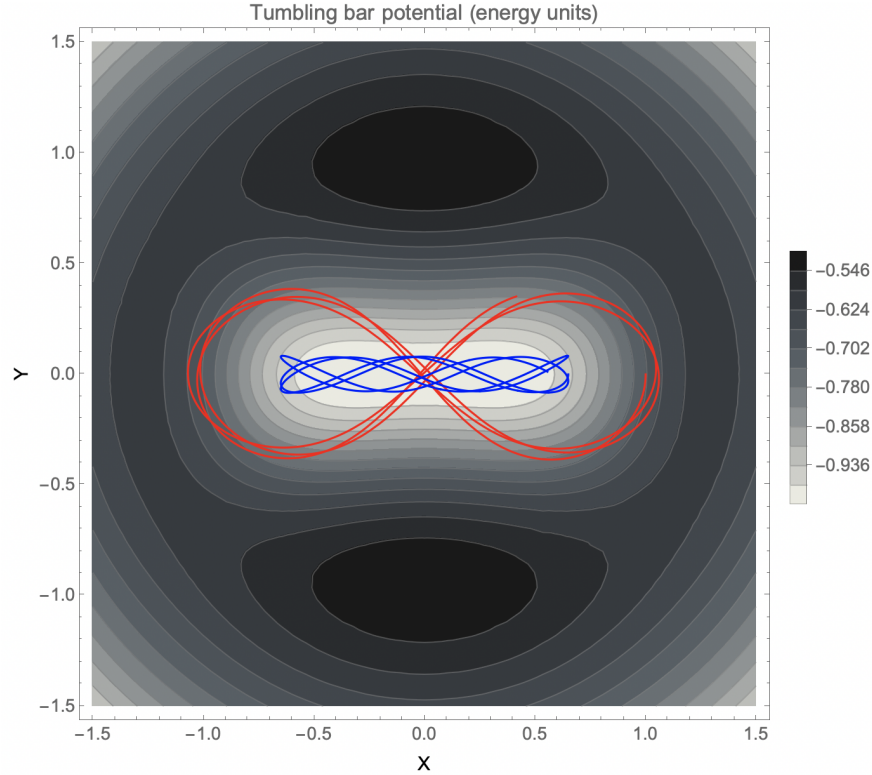


Figure 13. A toy model of a bar potential $\Phi_{\text{eff}} = \Phi_o - \Omega_b L$ that is partly supported by gas, and partly by stars born in the gas (Barnes & Tohline 2001). The dumbbell shape of the potential aligned with the bar is typical of bars of this kind, and seen in our simulations as the bar evolves. The low energy orbit (blue) crosses the axis several times in each radial oscillation; most orbits have this form. Higher energy orbits (red) can take a similar form, or exhibit the “bow tie” morphology, as shown.

dumbbell potential of Cazes & Tohline (2000) specifically tailored to a gaseous bar, but similar conclusions are drawn from simpler bar models.

If \mathcal{H} is the Hamiltonian of the system in the inertial frame, and $\mathbf{L}_z = \mathbf{x} \times \mathbf{p}$ is the angular momentum about the disk’s spin axis, neither of which are conserved in the tumbling potential, then we can define a conserved quantity, i.e. the Jacobi Integral $\mathcal{H}_J = \mathcal{H} - \Omega_b \cdot \mathbf{L}_z$ where Ω_b is the bar pattern speed. \mathcal{H}_J defines the energy of the orbit within the tumbling frame for which $\mathcal{H}_J = \Phi_{\text{eff}}$ establishes the “zero velocity surface” where all orbits are at their turnaround point. In order to examine the orbits, we solve Hamilton’s equations for the chosen effective potential Φ_{eff} describing a Cazes bar, where

$$\dot{\mathbf{q}} = \frac{\partial \mathcal{H}_J}{\partial \mathbf{p}}, \quad \dot{\mathbf{p}} = -\frac{\partial \mathcal{H}_J}{\partial \mathbf{q}} \quad (18)$$

At a fixed energy \mathcal{H}_J , we examine the main orbit families with real solutions, e.g. $(\dot{x} = 0, y = 0)$ at turnaround with (x, y) as solutions to Eq. 18. With these initial conditions, we carry out the symplectic orbit integration as described in Binney & Tremaine (2008, Sec. 3.4).

This brings us to the origin of the radial shear flow. Gas wants to follow the stars which it tends to do along circularized tube orbits in the outer disk. But over the inner disk, most stellar orbits follow the bar with frequent crossings of the bar axis, as shown in Fig. 13. The turbulent, viscous gas is not able to follow the bar crossing and is deflected into the forward direction before turning back sharply, at the extremities of the bar where the bar is weaker, reversing its direction. As first noted by Barnes & Tohline (2001), this specific potential includes the relatively unusual “bow tie” orbit that crosses at the galactic centre. Once again, gas attempting to cross at the centre is either accreted there or deflected forward to conserve momentum along the bar axis. Momentum is not conserved perpendicular to the bar axis.

4.4.3. Do bar-like gas flows help or hinder star formation?

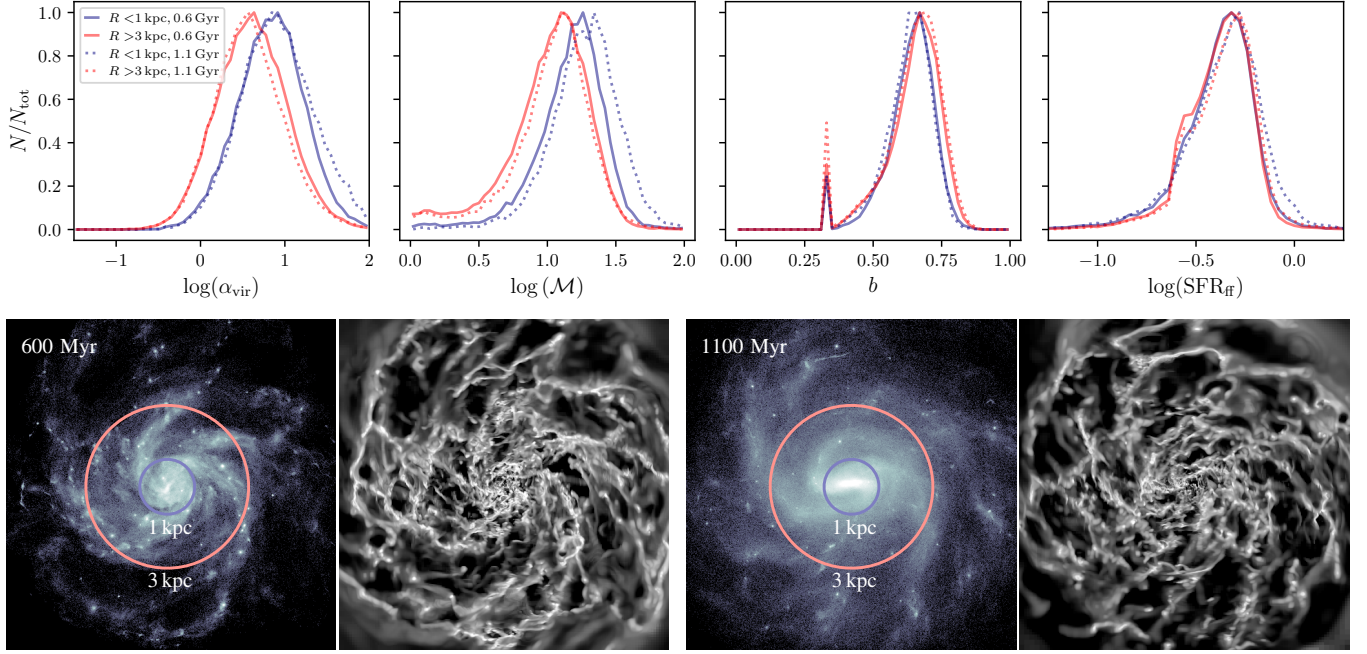


Figure 14. (Top) Key dimensionless parameters characteristic of resolved star forming regions extracted from the `fd50_fg40_nac` simulation re-run at high resolution. From left to right, these are: $\log(\alpha_{\text{vir}})$, $\log(\mathcal{M})$, b , $\log(\text{SFR}_{\text{ff}})$ – see main text for discussion. We compare the measured parameters in two radial zones: inner ($R < 1$ kpc) and outer ($1 < R < 3$ kpc). The solid lines show the results at 600 Myr, the dotted lines at a later time (1.1 Gyr) when a bar has formed. (Bottom) The radial zones are overlaid on the relevant time steps for young stars, next to the gas surface density maps. We find no significant change to the mode of star formation after bar formation; see also Fig. 15.

The science of how stars form is a central pillar of modern astrophysics (Mac Low & Klessen 2004). Some of the most important insights have come from studies of resolved galaxies (Kennicutt 1998), in particular, the explicit dependence of the star formation rate (SFR) on the cold gas surface density, μ_{gas} (Bigiel et al. 2008). Many studies invoke Toomre’s famous Q parameter

$$Q = \frac{\kappa \sigma_{\text{gas}}}{\pi G \mu_{\text{tot}}} \quad (19)$$

where values larger than about unity are considered to be locally stable to gravitational collapse (self gravity). Here, once again, κ is the local epicyclic frequency and σ_{gas} is the internal (cold) gas velocity dispersion. Note that μ_{tot} integrates over the contribution from stars (μ_{\star}), gas (μ_{gas}) and the underlying dark matter over the vertical scale of the gas. But when we consider two-fluid stability (e.g. Sec. 4.3.3), a different criterion is needed (Jog & Solomon 1984; Romeo 1992), particularly in the presence of turbulent media (Romeo et al. 2010; Agertz et al. 2015). Martin & Kennicutt (2001) found that Q averaged over azimuth, when evaluated as a function of galactic radius, roughly predicts where the star formation threshold occurs. The dependence on Q likely arises from the parameter’s inverse dependence on the gas surface density more than anything else.

While gas and star formation are occasionally seen along the length of stellar bars in resolved galaxies, the association is relatively rare. This has led to the idea that bars effectively “quench” star formation through strong shearing motions along the bar (e.g. George et al. 2019). A problem with this interpretation is that the SFR surface density Σ_{\star} shows a strong positive correlation with the epicyclic frequency κ (and the Oort parameters) in local disk galaxies (Aouad et al. 2020). It is more likely that the gas supply has been exhausted within present-day bars through the streaming process. Today, in large relatively rare, gas-rich galaxies, streaming gas is able to form stars (e.g. Hüttemeister et al. 1999).

For a well-resolved sample of disk galaxies, Aouad et al. (2020, and references therein) determine the Oort parameters A and B (equivalent to shear and vorticity, respectively) as a function of galactic radius, such that

$$A(R) = -\frac{1}{2}R \frac{d\Omega}{dR}, \quad B(R) = -(\Omega + \frac{1}{2}R \frac{d\Omega}{dR}) \quad (20)$$

where $\Omega = V_{\text{circ}}/R$ is the angular frequency and V_{circ} is the circular velocity at a radius R . These are easily related to other important parameters: the epicyclic frequency is $\kappa = \sqrt{-4B\Omega}$, the magnitude of vorticity is $\omega = |2B| = \kappa^2/2\Omega$, and the local shear velocity is $\dot{x} = 2\delta A$ where δ is the distance between two points at different radii in the shear flow⁵. Importantly, *there is no compelling observational evidence for star formation suppressed by either gas shear or gas vorticity*. In fact, the opposite may be true: μ_\star has a clear positive dependence on both B and κ , and only a weak dependence on A .

There is a substantial literature on how star formation can be enhanced through cloud collisions in regions of strong, turbulent shear and even reduced in regions of low shear (e.g. Tan 2000; Anathpindika 2010; Tasker & Tan 2009; Dobbs et al. 2015; Renaud et al. 2015; Takahira et al. 2018). Federrath & Klessen (2012) reason that high Mach numbers $\mathcal{M} = \sigma_{\text{gas}}/c_s$ in turbulent gas with sound speed c_s generally *increase* star formation rates compared to transonic or subsonic media. (Since interstellar gas is a magnetized medium, a more general definition for \mathcal{M} includes the magnetic pressure.) The virial parameter for a uniform spherical cloud $\alpha_{\text{vir}} = 2E_{\text{kin}}/|E_{\text{grav}}|$ must be kept small (Krumholz et al. 2005a). High Mach numbers generally increase the SFR since they lead to smaller clumps and high densities (cf. Sec. 3).

Thus, to offset the increased gas dispersion at high \mathcal{M} , the gravitational binding energy must be enhanced in high mass-density pockets. These are the conditions set up by shell-crossing due to eddies in a supersonically turbulent, magnetized medium. To quote Elmegreen (1993), “supersonic turbulence compresses gas at the interfaces between converging flows, and this compression lasts for a relatively long time equal to the crossing time *between* clumps.” Within these eddies, turbulently-compressed clumps form and disperse continually and continuously, but the densest clumps become gravitationally unstable and collapse. The mass spectrum of post-shock clumps can be calculated (Elmegreen 1990, 1993); higher turbulent Mach numbers produce stronger compression and higher star-formation rates (Federrath & Klessen 2012).

In Fig. 14, we present dimensionless properties – \mathcal{M} , α_{vir} , b , SFR_{ff} – measured from the `fd50_fg40_nacc` high-resolution simulation. This is done by running the simulation with a cell based efficiency per free-fall time derived from turbulence theory (see Eq. 8), rather than the fixed ϵ_{ff} introduced in Eq. 3. In future work we will explore the impact of such models further. All relevant turbulence parameters presented in Fig. 14 are measured locally on the mesh at the time of star formation.

These measures, which are crucial to resolve in any simulation of processes within star-forming regions, are compared in two radial zones – inside and outside the bar region – at two different times, as indicated. We resolve the forcing parameter b for each clump describing the nature of the compression⁶, typically in the range $b = 1/3$ (divergence free) to $b = 1$ (curl free). This parameter appears not to change either by location or in time, but more work is needed. Moreover, there is only a weak time dependence in any of the parameters. Interestingly, both α_{vir} and \mathcal{M} decline with increasing galactic radius, but in such a way that the SFR per freefall time, SFR_{ff} , is essentially invariant. The normalisation of the SFR with the local freefall time is appropriate to accommodate the multi-scale nature of a turbulent medium.

In Fig. 15, we show the radial profiles of the star formation rate surface density Σ_{SFR} , the gas depletion time and the average star formation efficiency per free fall time, $\epsilon_{\text{ff}} = t_{\text{ff}}/t_{\text{dep}}$, where t_{ff} is the azimuthally averaged gas free-fall time. Overall, as seen in the right hand panel, there is little evolution in the star formation efficiency by location or in time. We conclude that the radial shear flow or bar flow neither promotes nor suppresses star formation. We can overload a bar-like potential with gas and still form stars relatively efficiently. The streaming motions simply concentrate the star forming regions.

Thus, it is plausible that the shear flows arising in turbulent gas disks at early times provided the necessary conditions for forming stars in a central bar-like configuration. This bar-like structure is predicted to be associated with dense gas and young, luminous stars, or a post-starburst population if enough time has elapsed, i.e. of order a few disk rotations. This is what is seen in all of our Milky Way progenitor simulations.

4.4.4. Gaseous bars and their evolution

While we have a basic understanding of how stellar bars form, it is much less obvious why gaseous bars emerge at high gas fractions? Cold, rotationally-supported gas disks with self-gravity are low-entropy systems that are highly

⁵ x defines an axis in the reference frame rotating at the same angular frequency Ω of the system under consideration, e.g. galaxy disk, bar or spiral arm.

⁶ We approximate b via the the relative contribution of compressive and rotational motions to the total (local) gas flow using equation 5 in (Federrath et al. 2008).

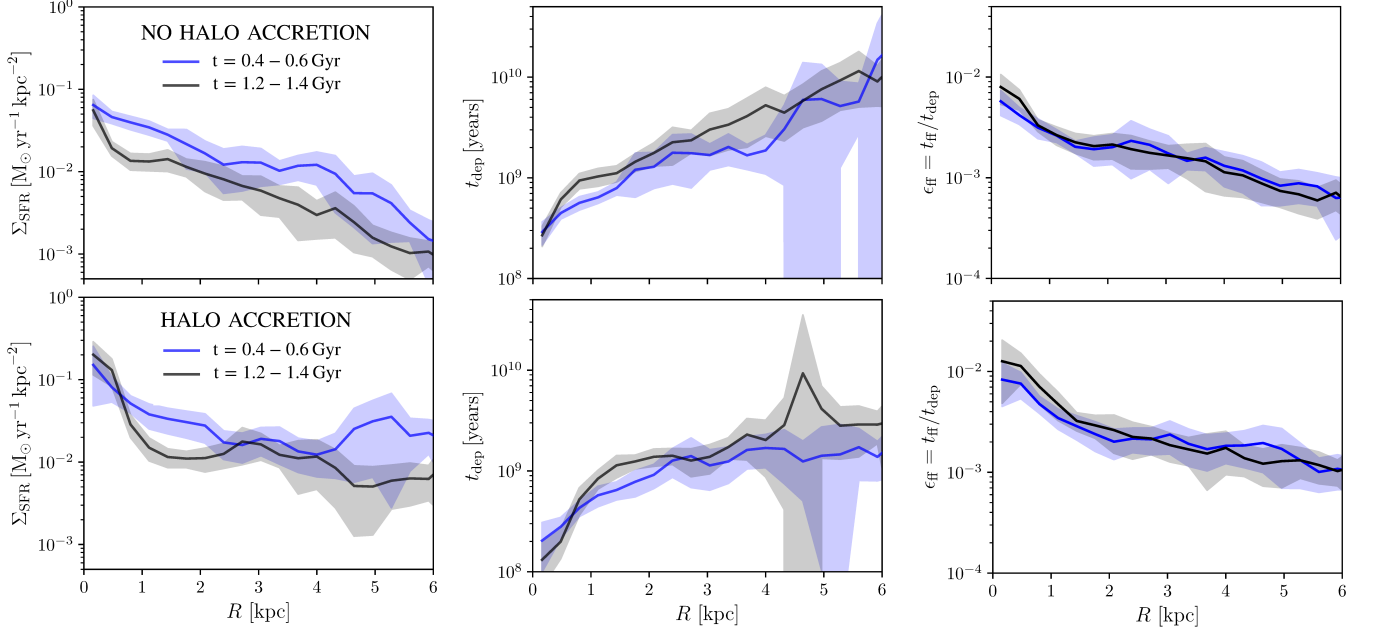


Figure 15. Azimuthally averaged radial profiles of (left) star formation rate surface density, Σ_{SFR} (middle) the gas depletion time, t_{dep} , and (right) the characteristic star formation efficiency per free fall time, ϵ_{ff} — see main text for definitions. These are the results for $f_{\text{gas}} = 40\%$ models without halo accretion (top) and with halo accretion (bottom). The two lines show results before ($0.4 - 0.6$ Gyr, blue) and after ($1.2 - 1.4$ Gyr, black) bar formation, with the shaded regions showing one standard deviation. Gas depletion due to star formation leads to a lowering of Σ_{SFR} over time, with a slight increase in t_{dep} . We find no significant change to the mode of star formation after bar formation, as indicated by the dimensionless ϵ_{ff} profiles; see also Fig. 14.

HALO-ACCRETION

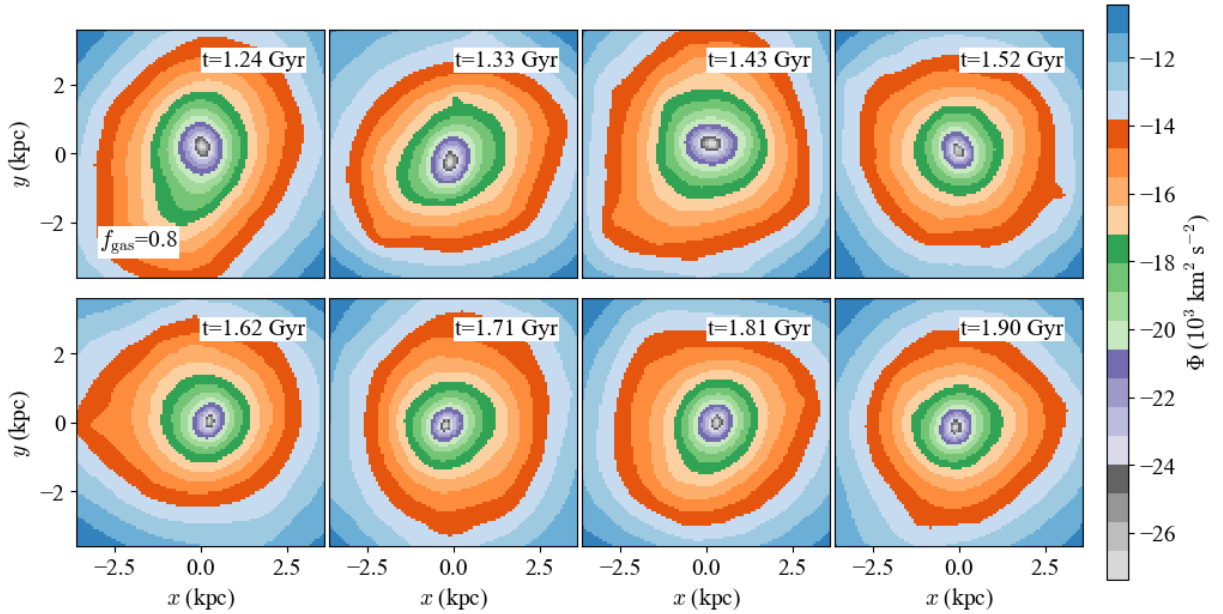


Figure 16. The evolution of the disk gravitational potential Φ from the $f_{\text{gas}} = 80\%$ model `fd50_fg80_acc`. Here, we show its later stages (top left to bottom right) after the central bar has begun to dissolve and on its way to forming a compact central bulge with a half mass radius of $r_b \approx 0.5$ ckpc.

susceptible to radial instabilities, much as with cold stellar disks. To quote from [Barnes & Tohline \(2001\)](#): “Just as cold, axisymmetric stellar dynamical configurations are known to be dynamically unstable toward a bisymmetric instability if they are sufficiently self-gravitating, the same is true for fluid configurations.” Part of the process appears to be young stars being launched into the disk⁷. Indeed, this is what is actually being observed in the simulations, e.g. Figs. 8, 9 and 12. The build-up of the young stellar bar is well defined, whereas the turbulence disperses the build-up of gas along the same axis. But the shear flow is the region where most stars are born. In Figs. 8 and 9, the disk’s central gravitational potential is bar-like even when the circumnuclear regions appear noisy.

What we see is that the turbulent disk forms discrete clumps and these launch dissolving star clusters into the disk. The young stars return energy to the cluster gas, which becomes overpressured and is forced out by a combination of radiation and wind action. Few of our clusters survive for more than 100 Myr or so, in line with [Bland-Hawthorn et al. \(2010\)](#). For example, in the simulation `fd50_fg100_nac`, star clusters emerge and disappear once the disk has settled down from the initial burst phase. These stars diffuse into the general disk for which the total baryon content dominates the local galactic potential. While this remains true, the stellar disk is susceptible to bar instabilities. Thus, it appears to be the young stars that lead the way to bar formation.

Gas-rich bars are occasionally observed in nearby galaxies, as discussed in Sec. 4.4.3, but always in association with dominant stellar bars ([Aalto et al. 1999](#); [Hüttemeister et al. 1999](#); [Kohno et al. 2008](#)). Nuclear gas bars are relatively common but appear to be associated with x_2 orbits embedded within the bar-supporting x_1 orbit families ([Athanasoulas 1992](#)). To date, we are unaware of any claims of a gas-dominated bar residing in a disk potential in the local Universe. The situation may be very different at high redshift, as discussed in the Introduction, with bar-like structures claimed in gas-dominated disks (e.g. [Tsukui et al. 2024](#); [Huang et al. 2023](#)). In the early universe, gas disks are likely to have formed before star formation commenced in the gas, as judged from the relative thinness of stellar disks at all epochs.

Are there fossil signatures in old stellar bars today that can separate the two different evolutionary paths? We have seen that gaseous bars emerge in a few rotation periods in turbulent gas disks, particularly at high fractions. It is interesting to contemplate what these become and how these differ from stellar bars that emerge from stellar disks. At the highest gas fractions, the gas-dominated bars collapse to form compact central bulges after 1.2–1.5 Gyr. This is a novel mechanism for bulge formation and deserves further study. Interestingly, bar formation dominated by radial shear flows do not appear to form box/peanut bulges, as can be seen from any of the $x - z$ or $y - z$ side elevations at our movie website.

In the prescient [Barnes & Tohline \(2001\)](#) study, they find that a high fraction of stars born in a gas bar are injected into ‘bowtie orbits’ and these build up a highly flattened dumbbell-shaped gravitational potential. [Barnes & Tohline \(2001\)](#) refer to this as the “Cazes bar” ([Cazes & Tohline 2000](#)) that was the focus of our study in Sec. 4.4.2. We provide an example of a bowtie (centre crossing) orbit in Fig. 13. The dumbbell shape is seen along the full length of the bar, unlike what is seen in the Milky Way for example where a *vertical* central box/peanut bulge has taken hold. The latter form through vertical instabilities and have been widely discussed since their discovery ([Combes et al. 1990](#)). In the Barnes study, there are surprisingly few prograde x_1 orbits in the gas bar compared to those that normally dominate N-body bars. Whether this is an artefact of their analytic model or symptomatic of gaseous bars remains to be seen.

5. DISCUSSION: BROADER IMPLICATIONS

5.1. Implications for high-redshift bars

In Fig. 17, we present an updated version of the diagram first presented in [Bland-Hawthorn et al. \(2023\)](#) in light of the results from Sec. 4.3.2. Given that cool ALMA disks are now being observed to $z \approx 6.5$ ([Neeleman et al. 2023](#)), we show only “bar – no bar” dividing lines for $z = 7$ and higher. The dashed lines refer to our earlier gas-free models; the solid lines refer to our new gas-rich models. Objects that fall above the lines have sufficient time to form a bar-like deformation in stars or in gas; objects that fall below the dividing lines do not.

The data points refer to data from [Price et al. \(2021\)](#) that is still the only published list of disk mass fractions beyond $z = 1$. But this is now becoming possible with ALMA data and so we anticipate f_{disk} data points at higher

⁷ It is unknown whether a turbulent gas-rich disk would form a bar without star formation, although this outcome seems feasible ([Cazes & Tohline 2000](#)). But, in our view, this is a philosophical question given that the high surface density of gas demands star formation to occur, and so we do not consider this case.

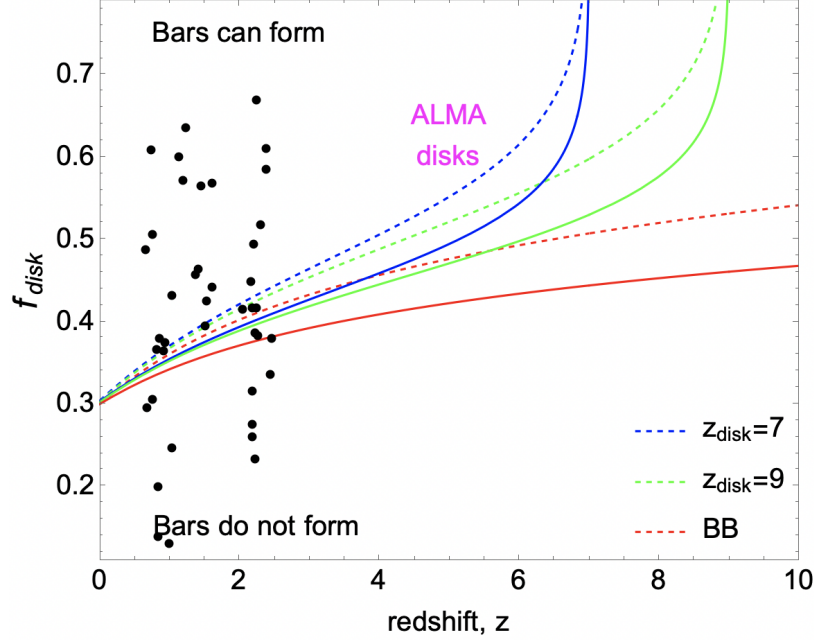


Figure 17. The inferred values of disk mass fraction f_{disk} plotted against the measured redshifts for each galaxy in Price et al. (2021); this is currently the only catalogue with computed f_{disk} data. The expected location of the highest-redshift ALMA galaxies is also indicated. The six overlaid curves are the dividing lines between bar formation and insufficient time for bars to form since the epoch of disk formation z_{disk} for three different disk onset times: (blue) $z_{\text{disk}} = 7$, (green) $z_{\text{disk}} = 9$, (red) Big Bang. Disk galaxies that fall above the curves are able to form a bar in the time span available. The dashed lines are for the gas-free models; the solid lines are for the turbulent gas disk models ($f_{\text{gas}} \gtrsim 40\%$) supported by star formation. The formulae for all curves are given in the text.

redshifts in the near future. The “ALMA disks” label refers to the region populated in the new unpublished study by F. Roman de Oliveira (2023, personal communication). In the upper regions, we anticipate that stellar bars will be more common at lower redshift, and gaseous bars will dominate at higher redshift given their accelerated formation times.

In Fig. 17, the three dashed curves for the gas-free model are as follows:

$$f_{\text{disk}}(z) = 0.30 - 0.0719424 \ln(-0.0559584 + g(z)) \quad z_{\text{disk}} = 7 \quad (21)$$

$$f_{\text{disk}}(z) = 0.30 - 0.0719424 \ln(-0.0400557 + g(z)) \quad z_{\text{disk}} = 9 \quad (22)$$

$$f_{\text{disk}}(z) = 0.311 - 0.0719424 \ln(1.220 g(z)) \quad z_{\text{disk}} = \infty \quad (23)$$

where

$$g(z) = 0.819698 \sinh^{-1} \frac{1.54591}{(z+1)^{3/2}}. \quad (24)$$

The small adjustment at $z = 0$ reflects the slightly higher halo mass compared to the low halo mass model in Bland-Hawthorn et al. (2023). The three solid curves for the gas-rich models ($f_{\text{gas}} \gtrsim 40\%$) are as follows:

$$f_{\text{disk}}(z) = 0.30 - 0.05 \ln(-0.0559584 + g(z)) \quad z_{\text{disk}} = 7 \quad (25)$$

$$f_{\text{disk}}(z) = 0.30 - 0.05 \ln(-0.0400557 + g(z)) \quad z_{\text{disk}} = 9 \quad (26)$$

$$f_{\text{disk}}(z) = 0.314 - 0.05 \ln(1.220 g(z)) \quad z_{\text{disk}} = \infty. \quad (27)$$

Here we have taken an average across all gas-rich models. The updated curves from Bland-Hawthorn et al. (2023) are constrained by the new $f_{\text{disk}} = 0.3, 0.5$ and 0.7 models (Table 1) and so are approximately correct. In future, more sampling in f_{disk} would be useful to refine the curves further.

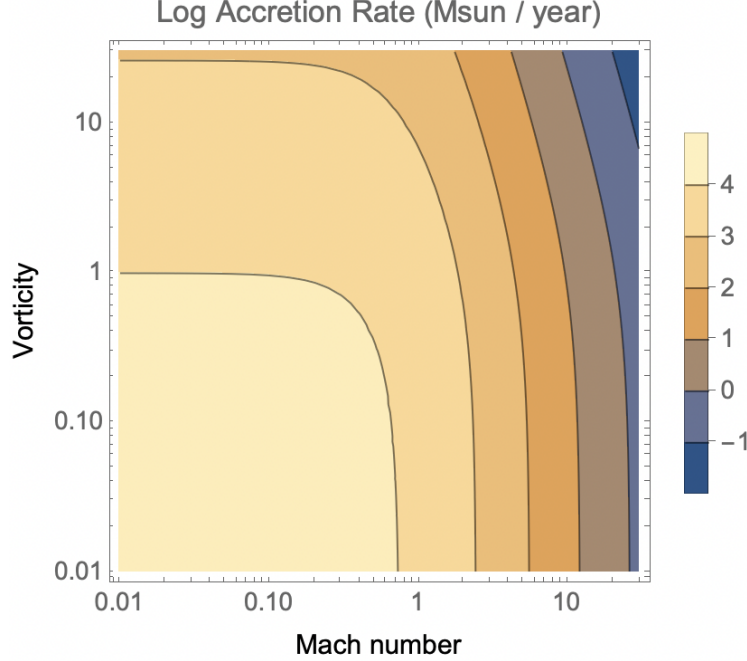


Figure 18. Bondi-Hoyle accretion rate for a supermassive black hole ($M_{\bullet} = 10^9 M_{\odot}$) as a function of the Mach number \mathcal{M} and normalised vorticity ω_{\star} of the infalling gas (see text for formulae). The contours show the accretion rate in log units of $M_{\odot} \text{ yr}^{-1}$. The region within the lowest contour (bottom left) is essentially the Bondi maximum accretion rate ($\mathcal{M} = 0$).

5.2. Implications for feeding nuclear activity

A remarkable aspect of high-redshift, turbulent ALMA disks is that some of them host powerful quasars (Farina et al. 2022; Walter et al. 2022; Tsukui & Iguchi 2021; Tsukui et al. 2023). Our work has identified interesting themes that can provide new avenues on the broader question of how supermassive black holes interact with their environment. The radial shear flow and its subsequent collapse to a central bulge (high f_{gas}) is a new phenomenon that should be investigated at higher spatial resolution using magnetohydrodynamics (e.g. Abramowicz & Fragile 2013).

Classically, quasar power is considered in the context of the Bondi-Hoyle accretion rate (Edgar 2004) given by

$$\dot{M}_{\bullet} = \frac{4\pi\rho_{\infty}(GM_{\bullet})^2}{(c_{\infty}^2 + v_{\infty}^2)^{3/2}} \quad (28)$$

$$= \frac{4\pi\rho_{\infty}(GM_{\bullet})^2}{c_{\infty}^3(1 + \mathcal{M}^2)^{3/2}} \quad (29)$$

where $(\rho_{\infty}, c_{\infty}, v_{\infty})$ are the density, sound and wind speed of the upwind flow far from the source, M_{\bullet} is the accretor mass, and \mathcal{M} is the sonic Mach number as before. (We have ignored additional factors, e.g. ratio of specific heats, that are of order unity - see Ruffert & Arnett (1994).) Numerous studies find that the Bondi-Hoyle formula substantially overestimates the accretion rate. But these estimates drop rapidly when one considers gas angular momentum and vorticity, instabilities and magnetic fields, and more realistic environments like turbulent media. Such considerations reveal that there are different regimes, e.g. a circumnuclear disk or torus that forms beyond the Schwarzschild radius, which modifies the ongoing accretion both through its geometry and subsequent feedback (e.g. Abramowicz & Zurek 1981).

There is already substantial work on how turbulent media supply gas to a supermassive black hole (q.v. Krumholz et al. 2005b). A useful approach is to examine the Bondi-Hoyle accretion rate in the presence of vorticity ($\nu = |\nabla \times v|$). This simple framework overlooks the fact that both momentum and mass are transferred to the accretor with the passage of time. The flow is also unstable, particularly in the region of the converged flow behind the accretor. Moreover, the accretion rate cannot be increased indefinitely because, at some point, the radiation pressure supplied by the accretion disk will cut off the gas supply (Eddington limit).

A helpful analysis is supplied by [Krumholz et al. \(2005b\)](#) who consider the dependence of the accretion rate on the nature of the approaching orbit. Low vorticity gas falls on essentially a radial orbit, gas accretes at the Bondi rate ($\approx r_B/c_s$) and the Bondi-Hoyle formula is unchanged. Gas approaching the accretor with high vorticity (equivalently, specific angular momentum ℓ) accretes at a much slower rate. In brief, the dimensionless vorticity $\nu_\star \approx 1$ describes the transition between efficient accretion and suppressed accretion. The transition vorticity $\nu_\star = 1$ corresponds to gas arriving at an impact parameter equal to the Bondi radius ($r_B = GM_\bullet/c_\infty^2$) travelling at the Keplerian velocity ($= \sqrt{GM_\bullet/r_B}$), with specific angular momentum $\ell_\infty \approx \nu_\star c_s r_B$ (see also [Abramowicz & Zurek 1981](#)). Here $c_s = c_\infty$ for an isothermal gas; [Krumholz et al. \(2005a\)](#) argues that the choice of the equation of state does not change the flow pattern or the accretion rate very much. The simplified approximation reduces to

$$\dot{M}_\bullet = 4\pi r_B^2 \rho_\infty c_s \mathcal{F}(\nu_\star) \quad (30)$$

where the piecewise function \mathcal{F} is supplied elsewhere ([Krumholz et al. 2005b](#)).

Thus, for a supermassive black hole with mass $M_\bullet = 10^9 M_\odot$, typical of high-redshift quasars, the accretion depends on both \mathcal{M} (see Eq. 29) and the gas vorticity (Fig. 18). In producing Fig. 18, we divide Eq. 30 by the Bondi accretion rate ($\mathcal{M} = 0$) (see [Krumholz et al. 2006](#)). From our initial analysis, we find that the inner regions have substantial levels of turbulence, with $\nu_\star \gg 1$ and Mach numbers $\mathcal{M} = 5 - 30$ (Fig. 14). The expected accretion rates are only $\dot{M}_\bullet \sim 0.01 - 1 M_\odot \text{ yr}^{-1}$, orders of magnitude below what is needed to explain the observations ($\dot{M}_\bullet \sim 10 - 100 M_\odot \text{ yr}^{-1}$) ([Farina et al. 2022](#)). At present, our simulations only reach to parsec scales and a different approach, in addition to MHD, is needed to go further (cf. [Federrath et al. 2021b](#); [Lee et al. 2014](#); [Cunningham et al. 2012](#)).

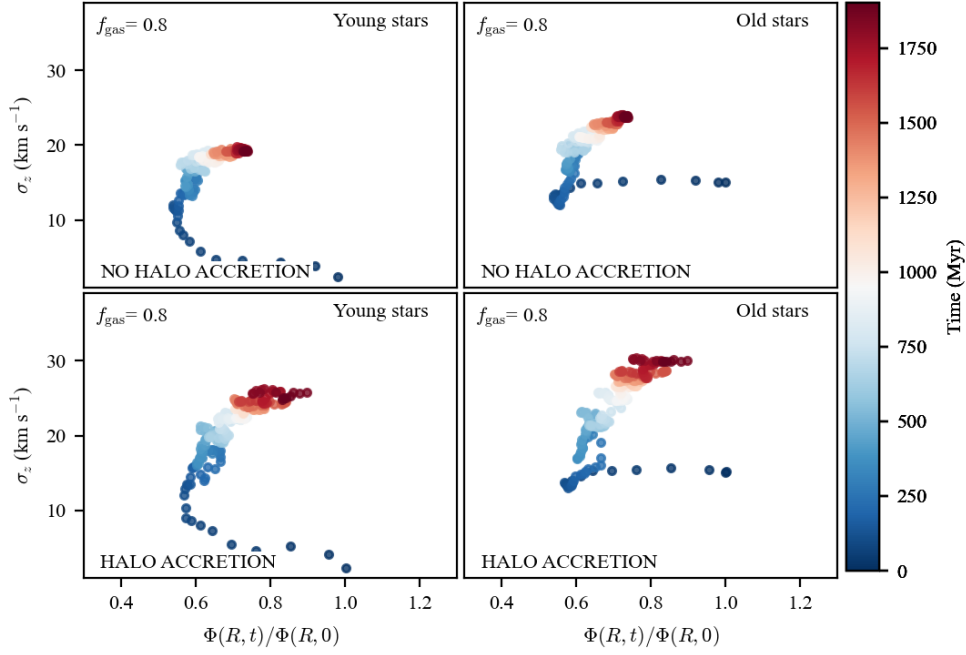


Figure 19. The evolution of the disk in the high gas fraction limit ($f_{\text{gas}} = 80\%$) for the (top) “no accretion” and (bottom) “halo accretion” simulations. (These are four magnified plots taken from Fig. 5.) The evolving disk potential is shown against the vertical dispersion for (left) young stars, (right) pre-existing stars. The colour coding indicates time passing, with blue to red indicating early to late times. As shown in Fig. 3, the disk gravitational potential loses a lot of baryon mass due to circulating winds, and then recovers this gas at later times. In the text, we show how the evolving kinematic dispersion can be understood dynamically.

5.3. Implications for disk evolution imposed by baryon mass loss

In Fig. 3, we presented the evolution of the total disk potential $\Phi(R, t)$ normalised to the starting potential $\Phi(R, 0)$. For $f_{\text{gas}} < 0.5$, the disk potential is fairly constant, but above this limit, the loss of gas mass in circulating winds leads to a substantial weakening of the disk potential by up to 50%. This is an unsettling aspect of trying to match the properties of high-redshift, gas-rich disks. The measured levels of SFR surface density are sufficient to disrupt the disk substantially or even entirely, assuming the strong mechanical coupling is correct. We can reduce the rate of mass loss from the disk by lowering the efficiency of feedback coupling. But the coupling efficiency used ($\sim 10\%$) is consistent with most contemporary cosmological simulations (e.g. Hopkins 2018; Agertz et al. 2021).

How does the weakening of the disk potential influence the disk’s dynamical evolution, including the observed stellar kinematics? Interestingly, this issue does not appear to have been addressed to date. Our analysis shows that, for the old stars (Fig. 19), the kinematic dispersions σ_R and σ_z both decline with time during the most active mass loss phase but then regather when the disk mass increases subsequently. The young stellar dispersions remain relatively constant as the disk weakens, before increasing as the disk potential grows again through reaccretion. All the while, the ratio σ_z/σ_R remains roughly constant. How are we to understand this?

To understand what happens to the *stellar* disk when a major part of the baryons are lost, we consider the galactic potential of an axisymmetric exponential disk. The mass loss is sufficiently slow (i.e. a few percent per rotation period) that we can treat the vertical action of an ensemble of stars as a conserved quantity, i.e. an adiabatic invariant. The vertical action J_z can be related to a disk’s vertical kinematic dispersion σ_z through the vertical disk frequency, Ω_z . For all actions ($i = R, \phi, z$), we may write

$$2\pi J_i = \oint \dot{x}_i dx_i = \frac{1}{\Omega_i} \int_0^{2\pi} (\dot{x})^2 d\theta_i = \frac{2\pi}{\Omega_i} \langle v_i^2 \rangle. \quad (31)$$

Thus the time average of a star’s squared velocity component is related to the action J_i through the associated frequency Ω_i such that $\langle v_i^2 \rangle = \Omega_i J_i$ (Bland-Hawthorn et al. 2019). Passing from this result for time averages for individual stars to population averages over the stars that reach a given place is non-trivial, but it generally follows that

$$\sigma_i^2/\sigma_j^2 = \langle \Omega_i J_i \rangle / \langle \Omega_j J_j \rangle \quad (32)$$

where $\langle \cdot \rangle$ is an appropriate average. More broadly, we may write

$$\sigma_z/\sigma_R \approx \sqrt{\langle \Omega_z/\Omega_R \rangle} \sqrt{\langle J_z/J_R \rangle}. \quad (33)$$

First, in order to understand why the dispersions decline during the mass loss phase, we consider a simple *axisymmetric* disk model (Binney & Tremaine 2008)

$$\Phi_o(R, z) = \frac{v_c^2}{2} \ln(R^2 + \frac{z^2}{q^2}) \quad (34)$$

for which the circular rotation curve ($z = 0$) has a constant circular velocity $v_\phi(R) = v_c$. This is the equation for an isothermal sphere that has been flattened by a factor $q < 1$ along the z -axis. More complex treatments arrive at the same general conclusion (Sharma & Bland-Hawthorn 2013). For a rotating system, the effective gravitational potential is given by

$$\Phi_{\text{eff}}(R, 0) = \Phi_o(R, 0) + \frac{L_z^2}{2R^2} \quad (35)$$

for which L_z is the conserved disk angular momentum about the z -axis.

The vertical and radial frequencies are defined by

$$\Omega_z^2 = \left| \frac{\partial^2 \Phi_{\text{eff}}}{\partial z^2} \right|_{z=0} \approx \frac{v_c^2}{q^2 R^2} \quad (36)$$

$$\Omega_R^2 = \left| \frac{\partial^2 \Phi_{\text{eff}}}{\partial R^2} \right|_{z=0} \approx \frac{v_c^2}{R^2} + O\left(\frac{1}{R^3}\right) \quad (37)$$

where both are evaluated in the plane at an arbitrary radius. The explicit appearance of q arises from flattening an isothermal spheroid, causing σ_z to increase due to adiabatic compression; there is negligible contribution to σ_R . If we assume that the disk keeps its shape as mass is lost slowly from the system, and the actions are broadly

conserved, at a fixed radius, both Ω_z and Ω_R must be reduced given the slower rotation speed. Thus, as observed in the simulations, both stellar dispersions decline as disk mass is lost, and the ratio σ_z/σ_R is approximately conserved. Stars move outwards and upwards, reaching progressively higher disk heights and disk radii. In practice, this ratio can be influenced by other internal processes (Ida et al. 1993). The dispersions σ_ϕ and σ_R are largely coupled by the epicyclic motion.

Interestingly, for all gas fractions, about half of the young stars are born in a very cold, thin disk, which is where the bar streaming and radial shear flow operate most effectively. A comparable fraction of stars appear to be born far from the mid-plane in the extended turbulent disk (see also van Dokkelaar et al. 2022). Much of the disk thickening appears to arise from these two processes, at least at early times although other processes are probably operating in a cosmological setting (e.g. Bird et al. 2021; McCluskey et al. 2024). We consider these other processes in later papers.

5.4. Implications for Galactic archaeology

The archaeological record contains a great deal of information about how the Milky Way’s stellar dispersions evolve as a function of location, stellar abundance and in time (Hayden et al. 2015; Aumer et al. 2016; Haywood et al. 2018). Since the launch of ESA Gaia, stellar dispersions can be determined for all axes, i.e. R , ϕ and z (Sharma et al. 2021). Cosmological simulators have come to appreciate the extraordinary richness contained within multidimensional kinematic data (e.g. McCluskey et al. 2024).

In Sec. 4.2, we showed how the vertical dispersions σ_z in stars and gas evolve within the turbulent disk simulations, but similar data can be extracted for all axes, as we show elsewhere. Our full suite of models have important implications for galactic archaeology (e.g. Hayden et al. 2015), which we explore in an upcoming paper for the GALAH DR4 data release (Bland-Hawthorn et al. 2024, in prep.). Our earlier work demonstrates that there is no discernible contribution from insufficient numerical resolution in our approach (Bland-Hawthorn & Tepper-García 2021) and so we believe the changing kinematic dispersions reflect dynamical processes (e.g. Ida et al. 1993; Aumer et al. 2016; Sharma et al. 2021).

In the last section, we looked at how the stellar disk is expected to evolve in the presence of mass loss through circulating wind flows, particularly at high gas fraction. Generally, the stellar dispersions are expected to decline at all radii where the disk baryons are reduced. *But the converse is also true* – a slow increase in disk mass has the opposite effect in the sense that the kinematic dispersions increase with time. Inter alia, this has implications for the old α -rich disk in the Milky Way, which has a vertical dispersion of about $\sigma_z^T \approx 50 \text{ km s}^{-1}$ today (Bland-Hawthorn & Gerhard 2016), a factor of two larger than the more massive α -poor disk. Such a large value for a rotating disk does *not* need to reflect its intrinsic dispersion at birth.

The α -rich disk preceded the more massive α -poor disk, which has built up mostly through quiescent accretion over past 9 – 10 Gyr, and shares the same gravitational potential. (The last significant merger event before the disrupting Sgr dwarf observed at the current epoch appears to date back to about $z \sim 2$.) Thus, the build-up of the α -poor disk over billions of years may have increased the α -rich *in situ* dispersion significantly from an initially low value, say, $\sigma_z^{Ti} \approx 25 - 30 \text{ km s}^{-1}$ as a consequence of conserved action. This possibility appears to have been overlooked to date.

In Fig. 5, the message is that halo accretion significantly increases the gas and stellar dispersions – at all radii and for all time – by almost a factor two in some cases, compared to the no-accretion models. Within an aperture of $R = 2.2R_{\text{disk}}$, for the “no halo accretion” models, we have an average value of $\langle\sigma_z\rangle \approx 18 \text{ km s}^{-1}$ at the highest f_{gas} , declining to $\langle\sigma_z\rangle \approx 6 \text{ km s}^{-1}$ for the most gas-poor model. For the halo accretion models, taken at the same time ($t_o \approx 1 \text{ Gyr}$), the vertical dispersions are $\langle\sigma_z\rangle \approx 30 \text{ km s}^{-1}$ and $\langle\sigma_z\rangle \approx 13 \text{ km s}^{-1}$ respectively. The ionized gas dispersions over the same apertures are factors of 2 – 3 times higher. These average values compare favourably with the warm (e.g. H α) and cold (e.g. CO) gas diagnostics for the range of values seen in galaxies matched in total baryonic mass (e.g. Ejdetjärn et al. 2022). In upcoming papers, we carry out detailed comparisons of our simulations with the latest high-redshift results (e.g. Tsukui et al. 2023; Neeleman et al. 2023).

5.5. Possible manifestations of turbulent gas disks

The most obvious manifestations of turbulent galaxies at high redshift are the observed high gas fractions, elevated star formation rates and broadened gas kinematics seen in ALMA and JWST surveys. These have been the main themes of our paper. To date, all of the enhanced star-forming disks at high redshift exhibit larger velocity dispersions than for local disks, regardless of the emission diagnostic used (Ejdetjärn et al. 2022), and presumably these reflect enhanced levels of turbulent energy. In future observations, these same galaxies are expected to have very active circumgalactic media that may be observable in ionized emission lines or in warm dust emission, and almost certainly

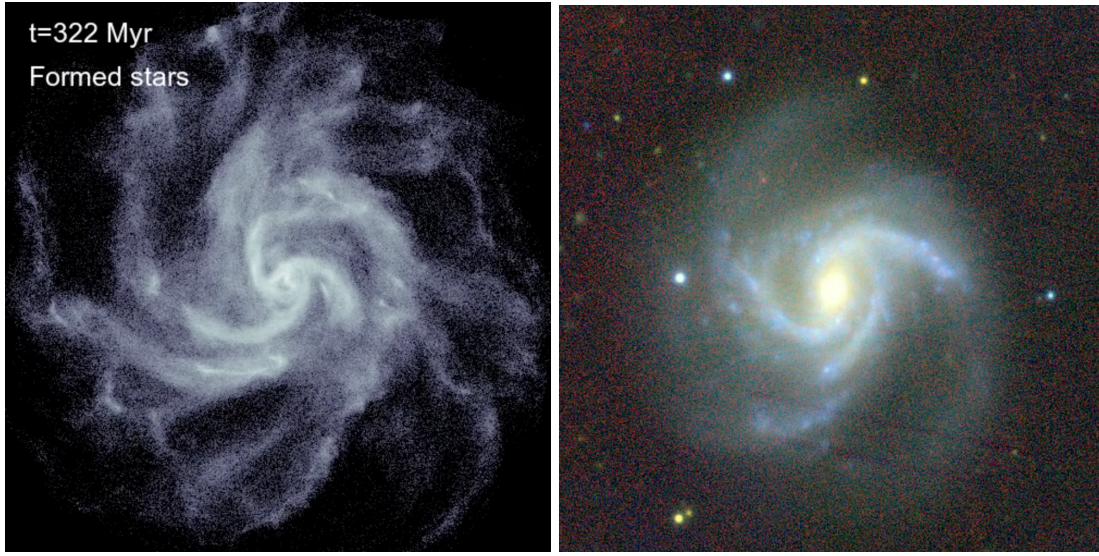


Figure 20. (Left) Three-arm spirals are a common occurrence in the early stages of gas-rich simulations for which disks dominate the local gravitational potential. The model uses $f_{\text{disk}} = 0.5$ with a gas fraction of 40%. We ran the simulation with three different random seeds, and 3-arm spirals are observed to be transitory (of order a rotation period) in each case. (Right) They are occasionally seen in nearby galaxies and at least one is claimed at high redshift (see text). The example shown here is NGC 7309 taken from C. Seligman’s atlas at <https://cseligman.com>.

in absorption-line diagnostics along quasar sightlines, for example (Tumlinson et al. 2017). It is unlikely that we can probe the stellar kinematics in the same way, except for fossil signatures that live on in local stellar populations, discussed briefly in the last section. But our simulations show a few manifestations that are worth contemplating in future observations.

An interesting feature of our gas-rich models is the occasional appearance of 3-arm ($m = 3$) spirals before the two-arm spiral and/or bar-like shear flow sets in. For example, 3-arm spirals emerge, albeit temporarily, in all three versions of `fd50_fg40_nac`; we show one such timestep in Fig. 20 (left). In the near field, there are spectacular 3-arm spirals known (Elmegreen et al. 1992; Hancock 2019), but this manifestation is relatively rare across disk galaxies; we show one example in Fig. 20 (right). The few studies that do exist agree that the 3-arm spiral is likely to be transitory and reflects a global instability, particularly if it is confined within the $m = 3$ resonances, i.e. $\Omega_s \pm \kappa/3$, where Ω_s is the spiral arm pattern speed, which appears to be the case. It can arise from an $m = 1$ mode (i.e. lopsided disturbance) interacting with an $m = 2$ mode (e.g. tidal perturbation). To our knowledge, such behaviour has not been modelled before, although $m = 3$ kinematic patterns have been considered (Canzian 1993). We raise the issue here because a 3-arm spiral has been suggested in a turbulent, gas-rich disk at $z = 2.2$ (Law et al. 2012). In brief, our models appear to confirm that this manifestation is relatively shortlived and indicative of large-scale instabilities early in the lifecycle of the disk.

Since their discovery with the Hubble Space Telescope (Cowie et al. 1995), ‘chain galaxies’ have defied an easy explanation (Elmegreen et al. 2004). These enigmatic objects were recently revisited in a new JWST study (Pandya et al. 2023). There are of order a hundred linear objects at $z = 1 - 3$ identified to date and these may comprise a heterogeneous class of objects, e.g. interacting and/or edge on clumpy galaxies (e.g. Dekel et al. 2009; Agertz et al. 2009), or lensed systems, but even so, many are difficult to explain, e.g. the example shown in Fig. 21. They are typically at the detection limit of the HST in most bands, are sufficiently bright in the restframe blue bands to suggest active star formation, and are of order a few kiloparsecs in linear dimension. Intriguingly, few show signs of a velocity gradient consistent with an edge-on disk undergoing circular rotation (e.g. Bunker et al. 2000). It is plausible that at least some of these sources may arise from star formation confined to a radial shear flow. This could explain the lack of a velocity gradient along the chain axis in some sources. But at higher spatial resolution, the shearing effect could be visible perpendicular to the flow (see Fig. 11). Further work is needed to establish if these reside within an extended cool gas disk since the radial shear flow cannot exist in isolation.

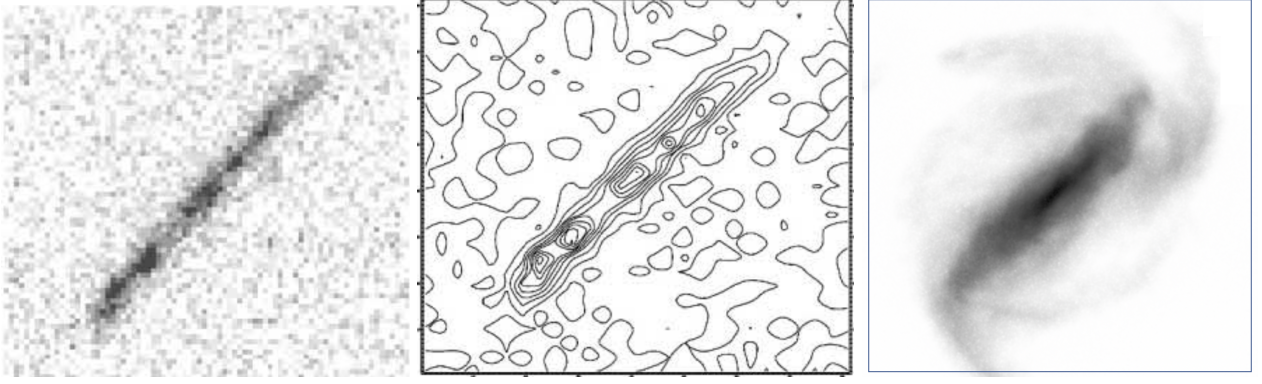


Figure 21. Example kiloparsec-scale ‘chain galaxy’ object from [Elmegreen et al. \(2004\)](#) where the V band intensity is shown (left) in grayscale and (middle) in contours; a more up-to-date collage is presented in [Pandya et al. \(2023, their figure 17\)](#). The contact layer in the radial shear flow produces stars along a narrow corridor (right); only the young stars are shown here; radiation transfer in dense gas (and matched instrument response) is needed to properly compare to the left and middle figures. This is a single timestep ($t_o = 1.677$ Gyr) taken from `fd50_fg20_nac` for illustration purposes. The few chain galaxies that have kinematic signatures show either weak or no evidence for velocity gradients along their axis, as observed in the simulated shear flow. Are some chain galaxies powered by radial shear flows in turbulent disks?

6. MAIN RESULTS

The surprising and compelling new evidence for well-developed disks (stars+gas) at early times (up to at least $z \approx 7$) is one of the most pressing problems in galaxy formation studies. The first hydro/N-body cosmological simulations tended to overload the central regions of galaxies with baryons. This was known as the “overcooling problem” and led to the introduction of feedback mechanisms to disperse the baryons over larger radial scales (e.g. [Benson 2010](#)). Just how the models are to be fixed to ensure dominant central baryons with net rotation at early times is not at all clear ([Kretschmer et al. 2022](#); [Gurvich et al. 2022](#)).

In [Bland-Hawthorn et al. \(2023\)](#), we set out to investigate and extend important work ([Fujii et al. 2018, 2019](#)) that deserves wider attention in light of new results for high-redshift disks in recent years (e.g. [Price et al. 2021](#); [Rizzo et al. 2020](#)). Even without any external interaction, given enough time, all substantial disks succumb to bar instabilities eventually. We refer to the exponential dependence of the bar formation time (τ_{bar}) as a function of f_{disk} as the ‘Fujii relation.’ Above some limiting value of f_{disk} ($\approx 0.30 \pm 0.05$), the bar formation time scales exponentially fast, with $1 < \tau_{\text{bar}} < 2$ Gyr for most models. We find that the presence of a bar in a high-redshift disk puts a lower limit on f_{disk} for a given redshift. Fig. 17 is particularly useful because f_{disk} can be estimated independently from the disk kinematics (e.g. [Genzel et al. 2020](#); [Förster Schreiber & Wuyts 2020](#); [Price et al. 2021](#)).

In our new work, we explore the evolution of gas-rich disks in the early Universe in the presence of strong turbulence driven by the energy output from star formation. We examine in detail the distinctive signatures of both no halo accretion and halo accretion models. In the former case, the gas supply and star formation rate decline fairly rapidly over an exponential timescale of about a Gyr; in the latter case, both decline once again but over a longer timescale.

Here are the summary points of our work to date where we include the earlier results in the first two items:

- For internally triggered stellar bars, there is a clear dependence between the disk mass fraction ($R \lesssim 2.2R_{\text{disk}}$) and the onset time of the stellar bar. After that, the bar is long-lived for gas-free simulations.
- If the disk baryons dominate the inner galaxy, stellar bars are likely to be common at redshifts currently surveyed by JWST and ALMA imaging ($z \lesssim 7$).
- If the disk baryons are sub-dominant, the bar onset time is very long ($t > 5$ Gyr) such that the bar is unlikely to form at high redshift; the fraction of baryons in gas does not alter this conclusion.
- If the disk baryons dominate the inner galaxy, the bar onset time does depend on the gas fraction. At $f_{\text{gas}} = 20\%$, the turbulent gas appears to speed up bar formation by 50% or more. For higher gas fractions, the bar onset time is at least a factor of two shorter than the gas-free case.

- In all cases, the stellar bars (in the presence of gas) are weaker than their gas-free counterpart. The bar strength and bar length appear to be inversely related to the gas fraction f_{gas} .
- As in observations, “gas bars” exist but are mostly stochastic and intermittent features. The observed bar-like objects seen with ALMA (see Sec. 1) may arise from young stars on bar-like orbits heating up the associated dust and molecules.
- In the high f_{gas} ($> 70\%$) limit, a (mostly gas) bar emerges but eventually collapses to form a bulge.
- For all gas-rich models, a radial shear flow is active. These produce the distinctive quadrupolar (quatrefoil) pattern in the gas kinematics, particularly at low f_{gas} , which may be visible in future ALMA observations.
- The predicted gas dispersions in the cool ($\lesssim 10^3$ K) gas are typically $\sigma_z \lesssim 30$ km s $^{-1}$ for both the halo accretion and no accretion models. The warm gas dispersions are consistently 2 – 3 times higher than their cool counterparts.

7. NEXT STEPS

Very little is known about the character, formation or evolution of early galactic disks ($z > 3$). These objects are currently at the observational limits of our most powerful telescopes and appear to be different in character from their low-redshift counterparts. We have attempted to provide a framework for advancing the discussion of these enigmatic objects.

A major omission at the present time is that there are only a handful of high-redshift galaxies with combined JWST and ALMA imaging, or combined JWST imaging and integral field spectroscopy (Förster Schreiber & Wuyts 2020). This issue will need to be addressed in the coming years. We anticipate that there will be large samples of galaxies with estimated f_{disk} values in the near future, out to the highest ALMA redshifts. JWST imaging will be needed to determine the baryon mass fraction in stars compared to gas, although significant dust corrections may be required. We fully anticipate that early disks will show evidence of blue, star-forming bars, nuclear disks and spiral arms, even while dominated by gas turbulence. Central stellar bulges are expected to be relatively small until later times ($z < 2$).

We have made the case for tracing departures from axisymmetry as evidence for the importance of baryons over dark matter in the inner regions of disk galaxies. This goes to the heart of how galaxies form and evolve at early times. Stellar bars and spiral arms are now seen well beyond $z \sim 2$; this was quite unexpected. Adding to the mystery, these manifestations were thought to be unlikely to occur in the presence of strong gas turbulence. All of the simulations show long-term evolution in their baryonic properties and distributions, as was demonstrated in Sec. 5.4. There are aspects of the existing simulations that we explore in more detail in later work, e.g. metal production, secular evolution (e.g. migration), 3D stellar dispersion (e.g. disk thickening), and the long-term evolution of the models within a CDM hierarchy.

A key step is to understand better how our controlled experiments (App. A) fit within the context of cosmological evolution. We have begun to consider the response of turbulent disks to external forces, in particular, the strong dynamical impulse from a merging system. Can the radial shear flow survive a merger interaction (A. Wetzel, personal communication)? An interesting prospect is that the radial shear flow is able to feed an active galactic nucleus, particularly at late times and high gas fractions when the gas bars collapse to a central bulge. In turn, how does the turbulent disk respond to strong AGN feedback?

Our early results point the way to future refinements and developments, especially in forward modelling to improve comparison with observations. We can use our simulations to interpret the limited multi-wavelength data for high-redshift disks. Specifically, we now post-process the multiphase simulations to address specific emission lines targetted by ALMA. These are particularly useful for establishing whether the inferred star formation rates, gas and dust fractions and total masses, etc. are mutually consistent. This line of analysis will benefit greatly from recent developments in non-equilibrium chemistry networks coupled to on-the-fly multifrequency radiation transport in RAMSES (PRISM: Katz et al. 2022). Moreover, the primary source of ionization or heating can be inferred from the relative strength of C $^+$, O and O $^+$ lines, inter alia. These lines have been used to infer gas masses but, in most instances, the line strengths are a reflection of cooling rates and how much energy was dumped into these lines initially (Appleton et al. 2017).

The predicted line strengths can guide our understanding of whether the simulated feedback processes coupling to the gas reflect the actual physical conditions. For example, in our attempt to model ALMA galaxy disks, we are forced to high gas fractions in dominant disks. But as we have seen, this can lead to a catastrophic loss of disk baryons in extrema, at least in our models, although the baryons are re-accreted in some models. Is it really true that some ALMA disks lay the seeds of their own destruction, or does this evolutionary path solve the longstanding mystery of superthin disc galaxies (Goad & Roberts 1981; Banerjee & Jog 2013; Ossa-Fuentes et al. 2023)?

Arguably, the most urgent improvement is to incorporate magnetohydrodynamics, accompanied by cosmic ray heating (Farcy et al. 2022), with good spatial resolution while operating on galactic scales. There are solid theoretical reasons for believing that magnetic fields influence the star formation prescriptions (Sec. 3.1.1). Moreover, it is feasible that, at even higher resolution, denser filaments emerge leading to a lower covering fraction and filaments that are harder to accelerate (e.g. Cooper et al. 2008, 2009), thus a lower overall coupling efficiency. This fundamental limitation has yet to be addressed by any of the cosmological simulations targetting galaxies in the early Universe. Rather than “feedback-free” galaxy evolution (e.g. Dekel et al. 2023), there is a case for weakening the strong coupling by a substantial factor. This is a problem that extends across to all cosmological simulations, and needs to be investigated.

8. ACKNOWLEDGMENTS

JBH, TTG and OA wish to thank Professors Paola Di Matteo and Misha Haywood for insightful conversations and for hosting them at the Paris Observatory. We received valuable feedback from Ken Freeman, Mark Krumholz, Francois Boulanger, Andrew Wetzel, Takafumi Tsukui, Emily Wisnioski, Francesca Rizzo, Filippo Fraternali and Fernanda Roman de Oliveira. We are grateful to Eugene Vasiliev for continuous assistance with AGAMA and to Walter Dehnen for help with his code. JBH is indebted to James Binney for long walks, pub lunches and inspired conversations, and to Merton College and the Beecroft building for providing a stimulating research environment.

TTG acknowledges financial support from the Australian Research Council (ARC) through an Australian Laureate Fellowship awarded to JBH. OA acknowledges support from the Knut and Alice Wallenberg Foundation, the Swedish Research Council (grant 2019-04659) and the Swedish National Space Agency (SNSA Dnr 2023-00164). CF acknowledges funding provided by the Australian Research Council (Discovery Project DP230102280), and the Australia-Germany Joint Research Cooperation Scheme (UA-DAAD).

The computations and data storage were enabled by two facilities: (i) the National Computing Infrastructure (NCI) Adapter Scheme, provided by NCI Australia, an NCRIS capability supported by the Australian Government; and (ii) LUNARC, the Centre for Scientific and Technical Computing at Lund University (resource allocations LU 2023/2-39 and LU 2023/12-6).

APPENDIX

A. THE CASE FOR CONTROLLED EXPERIMENTS OF ISOLATED SYSTEMS

Controlled experiments sit between theoretical models and cosmological simulations, and are complementary to both. They are very useful for isolating processes that are not easily apparent in a cosmological setting. Our new framework is the ideal setting to understand the long-term relationship between the evolving ISM and stellar dynamical processes. The advantage of a controlled experiment is especially apparent when dealing with highly non-linear processes. Cosmological simulations have the advantage of treating the evolving hierarchy realistically, since mass assembly is largely driven by the dark matter. Once baryons are included, it becomes increasingly difficult to understand the role of interacting processes given the very large number of free parameters, made more difficult by inadequate numerical resolution. In general, the best results have come from re-running a simulation of a specific “local volume” at higher resolution (e.g. Sorce et al. 2016; Ma et al. 2017) but even then, there are many competing processes to unwind.

Famously, some of the earliest (restricted) N-body calculations (Toomre & Toomre 1972) revealed the emergence of bridges, tails and spiral-like features in galaxy-galaxy interactions. Related phenomena include stellar shells interleaved in radius that are due to an infalling satellite (Quinn 1984; Barnes & Hernquist 1992), now detected in cosmological simulations (Pop et al. 2018). In a seminal paper, through controlled simulations, Sellwood & Carlberg (1984) showed how spiral instabilities are triggered by accretion and star formation, and are likely to be transient features of disk galaxies.

There are numerous examples of how controlled N-body experiments have led to new insights in galactic dynamics (Athanasoula 1992). Typically, these manifestations are preceded by a strong theoretical basis, but not always (Binney & Tremaine 2008). The discovery of 2D (Hohl 1971) and 3D (Combes et al. 1990) bar instabilities came from early N-body simulations of isolated disks. Later it was shown that bars must slow down due to the exchange of energy through dynamical friction with a live (reactive) dark matter halo (Debattista & Sellwood 1998). A related process also makes a difference to the accretion of satellites in low-eccentricity orbits, and dynamical friction of these systems against the baryon disk can be much more important than against the dark halo (Walker et al. 1996).

After Sellwood & Binney (2002) argued on theoretical grounds that stellar migration was possible, Roškar et al. (2008) realized the same behaviour in an isolated N-body disk, albeit with much higher rates of migration. Inner and outer disk rings and resonances (Sellwood & Wilkinson 1993), outer disk warps and flares (Binney 1992; Reshetnikov & Combes 1998) were first realized in controlled N-body experiments, as were other manifestations like disk heating due to disk-crossing satellites (Quinn et al. 1993), prior to being observed in cosmological simulations, and this trend persists to the present time. For example, when a strong impulse (e.g. disk-crossing massive satellite) warps the outer disk, this triggers a bending wave (corrugation) across the inner disk that *wraps up* with the disk’s differential rotation (Bland-Hawthorn & Tepper-García 2021). Beyond the Milky Way, corrugations have since been seen in several disk galaxies with outer warps (Urrejola-Mora et al. 2022).

When Antoja et al. (2018) discovered the remarkable “phase spiral” in the local disk, this was soon realized in a dozen controlled experiments before being detected in cosmological simulations (q.v. García-Conde et al. 2022). Aumer et al. (2016) showed that the observed 3D stellar kinematic dispersions in the Milky Way result largely from the collective effects of scattering in both molecular clouds and spiral arms over cosmic time. Impressively, these processes are beginning to emerge in the best zoom-in simulations (McCluskey et al. 2024).

We recognize that upcoming cosmological simulations will soon produce more realistic gas-rich disks at earlier times. This is likely to be a very complex and messy process. Synthetic galaxies at any epoch will continue to be highly idealised in the sense that no method is yet able to fully accommodate MHD dynamos and diffusion, suprathermal particle and cosmic ray heating, dust and molecular processes, and so forth. In part, our motivation for the new work is to provide a framework for simplifying what is seen in cosmological simulations with a view to understanding what happens with each added parameter. In upcoming work, we compare our results to the earliest disk systems emerging in the VINTERGATAN simulations that use, by design, the same star formation and feedback prescriptions (Agertz et al. 2021).

REFERENCES

- Aalto, S., Hüttemeister, S., Scoville, N. Z., & Thaddeus, P. 1999, *ApJ*, 522, 165, doi: [10.1086/307610](https://doi.org/10.1086/307610)
- Abramowicz, M. A., & Fragile, P. C. 2013, *Living Reviews in Relativity*, 16, 1, doi: [10.12942/lrr-2013-1](https://doi.org/10.12942/lrr-2013-1)
- Abramowicz, M. A., & Zurek, W. H. 1981, *ApJ*, 246, 314, doi: [10.1086/158924](https://doi.org/10.1086/158924)
- Agertz, O., Kravtsov, A. V., Leitner, S. N., & Gnedin, N. Y. 2013, *ApJ*, 770, 25, doi: [10.1088/0004-637X/770/1/25](https://doi.org/10.1088/0004-637X/770/1/25)
- Agertz, O., Romeo, A. B., & Grisdale, K. 2015, *MNRAS*, 449, 2156, doi: [10.1093/mnras/stv440](https://doi.org/10.1093/mnras/stv440)
- Agertz, O., Teyssier, R., & Moore, B. 2009, *MNRAS*, 397, L64, doi: [10.1111/j.1745-3933.2009.00685.x](https://doi.org/10.1111/j.1745-3933.2009.00685.x)
- Agertz, O., Renaud, F., Feltzing, S., et al. 2021, *MNRAS*, 503, 5826, doi: [10.1093/mnras/stab322](https://doi.org/10.1093/mnras/stab322)
- Anathpindika, S. V. 2010, *MNRAS*, 405, 1431, doi: [10.1111/j.1365-2966.2010.16541.x](https://doi.org/10.1111/j.1365-2966.2010.16541.x)
- Antoja, T., Helmi, A., Romero-Gómez, M., et al. 2018, *Nature*, 561, 360, doi: [10.1038/s41586-018-0510-7](https://doi.org/10.1038/s41586-018-0510-7)
- Aouad, C. J., James, P. A., & Chilingarian, I. V. 2020, *MNRAS*, 496, 5211, doi: [10.1093/mnras/staa1945](https://doi.org/10.1093/mnras/staa1945)
- Appleton, P. N., Guillard, P., Togi, A., et al. 2017, *ApJ*, 836, 76, doi: [10.3847/1538-4357/836/1/76](https://doi.org/10.3847/1538-4357/836/1/76)
- Ascasibar, Y., Yepes, G., Müller, V., & Gottlöber, S. 2003, *MNRAS*, 346, 731
- Asplund, M., Grevesse, N., Sauval, A. J., & Scott, P. 2009, *ARA&A*, 47, 481, doi: [10.1146/annurev.astro.46.060407.145222](https://doi.org/10.1146/annurev.astro.46.060407.145222)
- Athanasoula, E. 1992, *MNRAS*, 259, 345, doi: [10.1093/mnras/259.2.345](https://doi.org/10.1093/mnras/259.2.345)
- Athanasoula, E., Machado, R. E. G., & Rodionov, S. A. 2013, *MNRAS*, 429, 1949, doi: [10.1093/mnras/sts452](https://doi.org/10.1093/mnras/sts452)
- Athanasoula, E., & Sellwood, J. A. 1986, *MNRAS*, 221, 213, doi: [10.1093/mnras/221.2.213](https://doi.org/10.1093/mnras/221.2.213)
- Aubert, D., & Teyssier, R. 2010, *ApJ*, 724, 244, doi: [10.1088/0004-637X/724/1/244](https://doi.org/10.1088/0004-637X/724/1/244)
- Aumer, M., Binney, J., & Schönrich, R. 2016, *MNRAS*, 462, 1697, doi: [10.1093/mnras/stw1639](https://doi.org/10.1093/mnras/stw1639)

- Banerjee, A., & Jog, C. J. 2013, *MNRAS*, 431, 582, doi: [10.1093/mnras/stt186](https://doi.org/10.1093/mnras/stt186)
- Barnes, E. I., & Tohline, J. E. 2001, *ApJ*, 551, 80, doi: [10.1086/320073](https://doi.org/10.1086/320073)
- Barnes, J. E., & Hernquist, L. 1992, *ARA&A*, 30, 705, doi: [10.1146/annurev.aa.30.090192.003421](https://doi.org/10.1146/annurev.aa.30.090192.003421)
- Bellocchi, E., Arribas, S., & Colina, L. 2012, *A&A*, 542, A54, doi: [10.1051/0004-6361/201117894](https://doi.org/10.1051/0004-6361/201117894)
- Benson, A. J. 2010, *PhR*, 495, 33
- Berentzen, I., Shlosman, I., Martinez-Valpuesta, I., & Heller, C. H. 2007, *ApJ*, 666, 189, doi: [10.1086/520531](https://doi.org/10.1086/520531)
- Bigiel, F., Leroy, A., Walter, F., et al. 2008, *AJ*, 136, 2846, doi: [10.1088/0004-6256/136/6/2846](https://doi.org/10.1088/0004-6256/136/6/2846)
- Binney, J. 1992, *ARA&A*, 30, 51, doi: [10.1146/annurev.aa.30.090192.000411](https://doi.org/10.1146/annurev.aa.30.090192.000411)
- Binney, J., & Tremaine, S. 2008, *Galactic Dynamics: Second Edition*
- Bird, J. C., Loebman, S. R., Weinberg, D. H., et al. 2021, *MNRAS*, 503, 1815, doi: [10.1093/mnras/stab289](https://doi.org/10.1093/mnras/stab289)
- Bland-Hawthorn, J., & Gerhard, O. 2016, *Annual Review of Astronomy and Astrophysics*, 54, 529
- Bland-Hawthorn, J., Krumholz, M. R., & Freeman, K. 2010, *ApJ*, 713, 166, doi: [10.1088/0004-637X/713/1/166](https://doi.org/10.1088/0004-637X/713/1/166)
- Bland-Hawthorn, J., & Tepper-García, T. 2021, *MNRAS*, 504, 3168
- Bland-Hawthorn, J., Tepper-García, T., Agertz, O., & Freeman, K. 2023, *ApJ*, 947, 80, doi: [10.3847/1538-4357/acc469](https://doi.org/10.3847/1538-4357/acc469)
- Bland-Hawthorn, J., Sharma, S., Tepper-García, T., et al. 2019, *MNRAS*, 486, 1167, doi: [10.1093/mnras/stz217](https://doi.org/10.1093/mnras/stz217)
- Blondin, J. M., Wright, E. B., Borkowski, K. J., & Reynolds, S. P. 1998, *ApJ*, 500, 342, doi: [10.1086/305708](https://doi.org/10.1086/305708)
- Bullock, J. S., Dekel, A., Kolatt, T. S., et al. 2001, *ApJ*, 555, 240
- Bunker, A. J., Moustakas, L. A., & Davis, M. 2000, *ApJ*, 531, 95, doi: [10.1086/308432](https://doi.org/10.1086/308432)
- Burkhart, B., & Mocz, P. 2019, *ApJ*, 879, 129, doi: [10.3847/1538-4357/ab25ed](https://doi.org/10.3847/1538-4357/ab25ed)
- Canzian, B. 1993, *ApJ*, 414, 487, doi: [10.1086/173095](https://doi.org/10.1086/173095)
- Carilli, C. L., & Walter, F. 2013, *ARA&A*, 51, 105, doi: [10.1146/annurev-astro-082812-140953](https://doi.org/10.1146/annurev-astro-082812-140953)
- Cazes, J. E., & Tohline, J. E. 2000, *ApJ*, 532, 1051, doi: [10.1086/308609](https://doi.org/10.1086/308609)
- Chabrier, G. 2003, *PASP*, 115, 763, doi: [10.1086/376392](https://doi.org/10.1086/376392)
- Chapman, S. C., Smail, I., Windhorst, R., Muxlow, T., & Ivison, R. J. 2004, *ApJ*, 611, 732, doi: [10.1086/422383](https://doi.org/10.1086/422383)
- Cioffi, D. F., McKee, C. F., & Bertschinger, E. 1988, *ApJ*, 334, 252, doi: [10.1086/166834](https://doi.org/10.1086/166834)
- Combes, F., Debbasch, F., Friedli, D., & Pfenniger, D. 1990, *A&A*, 233, 82
- Cooper, J. L., Bicknell, G. V., Sutherland, R. S., & Bland-Hawthorn, J. 2008, *ApJ*, 674, 157, doi: [10.1086/524918](https://doi.org/10.1086/524918)
- . 2009, *ApJ*, 703, 330, doi: [10.1088/0004-637X/703/1/330](https://doi.org/10.1088/0004-637X/703/1/330)
- Correa, C. A., Wyithe, J. S. B., Schaye, J., & Duffy, A. R. 2015, *MNRAS*, 452, 1217
- Costantin, L., Pérez-González, P. G., Guo, Y., et al. 2023, arXiv e-prints, arXiv:2311.04283, <https://arxiv.org/abs/2311.04283>
- Cowie, L. L., Hu, E. M., & Songaila, A. 1995, *AJ*, 110, 1576, doi: [10.1086/117631](https://doi.org/10.1086/117631)
- Cunningham, A. J., McKee, C. F., Klein, R. I., Krumholz, M. R., & Teyssier, R. 2012, *ApJ*, 744, 185, doi: [10.1088/0004-637X/744/2/185](https://doi.org/10.1088/0004-637X/744/2/185)
- Dawson, S., McCrady, N., Stern, D., et al. 2003, *AJ*, 125, 1236, doi: [10.1086/367792](https://doi.org/10.1086/367792)
- Debattista, V. P., & Sellwood, J. A. 1998, *ApJL*, 493, L5, doi: [10.1086/311118](https://doi.org/10.1086/311118)
- Dehnen, W., Semczuk, M., & Schönrich, R. 2023, *MNRAS*, 518, 2712, doi: [10.1093/mnras/stac3184](https://doi.org/10.1093/mnras/stac3184)
- Dekel, A., Sari, R., & Ceverino, D. 2009, *ApJ*, 703, 785, doi: [10.1088/0004-637X/703/1/785](https://doi.org/10.1088/0004-637X/703/1/785)
- Dekel, A., Sarkar, K. C., Birnboim, Y., Mandelker, N., & Li, Z. 2023, *MNRAS*, 523, 3201, doi: [10.1093/mnras/stad1557](https://doi.org/10.1093/mnras/stad1557)
- Dhawalikar, S., Federrath, C., Davidovits, S., et al. 2022, *MNRAS*, 514, 1782, doi: [10.1093/mnras/stac1480](https://doi.org/10.1093/mnras/stac1480)
- Dobbs, C. L., Pringle, J. E., & Duarte-Cabral, A. 2015, *MNRAS*, 446, 3608, doi: [10.1093/mnras/stu2319](https://doi.org/10.1093/mnras/stu2319)
- Edgar, R. 2004, *NewAR*, 48, 843, doi: [10.1016/j.newar.2004.06.001](https://doi.org/10.1016/j.newar.2004.06.001)
- Ejdetjärn, T., Agertz, O., Östlin, G., Renaud, F., & Romeo, A. B. 2022, *MNRAS*, 514, 480, doi: [10.1093/mnras/stac1414](https://doi.org/10.1093/mnras/stac1414)
- Elmegreen, B. G. 1990, *ApJL*, 361, L77, doi: [10.1086/185831](https://doi.org/10.1086/185831)
- . 1993, *ApJL*, 419, L29, doi: [10.1086/187129](https://doi.org/10.1086/187129)
- Elmegreen, B. G., & Elmegreen, D. M. 1985, *ApJ*, 288, 438, doi: [10.1086/162810](https://doi.org/10.1086/162810)
- Elmegreen, B. G., Elmegreen, D. M., & Leitner, S. N. 2003, *ApJ*, 590, 271, doi: [10.1086/374860](https://doi.org/10.1086/374860)
- Elmegreen, B. G., Elmegreen, D. M., & Montenegro, L. 1992, *ApJS*, 79, 37, doi: [10.1086/191643](https://doi.org/10.1086/191643)
- Elmegreen, D. M., Elmegreen, B. G., & Sheets, C. M. 2004, *ApJ*, 603, 74, doi: [10.1086/381357](https://doi.org/10.1086/381357)
- Erwin, P. 2018, *MNRAS*, 474, 5372, doi: [10.1093/mnras/stx3117](https://doi.org/10.1093/mnras/stx3117)
- Farcy, M., Rosdahl, J., Dubois, Y., Blaizot, J., & Martin-Alvarez, S. 2022, *MNRAS*, 513, 5000, doi: [10.1093/mnras/stac1196](https://doi.org/10.1093/mnras/stac1196)

- Farina, E. P., Schindler, J.-T., Walter, F., et al. 2022, *ApJ*, 941, 106, doi: [10.3847/1538-4357/ac9626](https://doi.org/10.3847/1538-4357/ac9626)
- Federrath, C. 2013, *MNRAS*, 436, 1245, doi: [10.1093/mnras/stt1644](https://doi.org/10.1093/mnras/stt1644)
- . 2015, *MNRAS*, 450, 4035, doi: [10.1093/mnras/stv941](https://doi.org/10.1093/mnras/stv941)
- . 2018, *Physics Today*, 71, 38, doi: [10.1063/PT.3.3947](https://doi.org/10.1063/PT.3.3947)
- Federrath, C., & Banerjee, S. 2015, *MNRAS*, 448, 3297, doi: [10.1093/mnras/stv180](https://doi.org/10.1093/mnras/stv180)
- Federrath, C., & Klessen, R. S. 2012, *ApJ*, 761, 156, doi: [10.1088/0004-637X/761/2/156](https://doi.org/10.1088/0004-637X/761/2/156)
- Federrath, C., Klessen, R. S., Iapichino, L., & Beattie, J. R. 2021a, *Nature Astronomy*, 5, 365, doi: [10.1038/s41550-020-01282-z](https://doi.org/10.1038/s41550-020-01282-z)
- . 2021b, *Nature Astronomy*, 5, 365, doi: [10.1038/s41550-020-01282-z](https://doi.org/10.1038/s41550-020-01282-z)
- Federrath, C., Klessen, R. S., & Schmidt, W. 2008, *ApJL*, 688, L79, doi: [10.1086/595280](https://doi.org/10.1086/595280)
- Federrath, C., Roman-Duval, J., Klessen, R. S., Schmidt, W., & Mac Low, M. 2010, *A&A*, 512, A81, doi: [10.1051/0004-6361/200912437](https://doi.org/10.1051/0004-6361/200912437)
- Federrath, C., Schrön, M., Banerjee, R., & Klessen, R. S. 2014, *ApJ*, 790, 128, doi: [10.1088/0004-637X/790/2/128](https://doi.org/10.1088/0004-637X/790/2/128)
- Ferreira, L., Conselice, C. J., Sazonova, E., et al. 2022, arXiv e-prints, arXiv:2210.01110, doi: [10.48550/arXiv.2210.01110](https://doi.org/10.48550/arXiv.2210.01110)
- Förster Schreiber, N. M., & Wuyts, S. 2020, *Annual Review of Astronomy and Astrophysics*, 58, 661, doi: [10.1146/annurev-astro-032620-021910](https://doi.org/10.1146/annurev-astro-032620-021910)
- Förster Schreiber, N. M., Genzel, R., Lehnert, M. D., et al. 2006, *ApJ*, 645, 1062, doi: [10.1086/504403](https://doi.org/10.1086/504403)
- Fujii, M. S., Bédorf, J., Baba, J., & Portegies Zwart, S. 2018, *MNRAS*, 477, 1451
- . 2019, *MNRAS*, 482, 1983, doi: [10.1093/mnras/sty2747](https://doi.org/10.1093/mnras/sty2747)
- García-Conde, B., Roca-Fàbrega, S., Antoja, T., Ramos, P., & Valenzuela, O. 2022, *MNRAS*, 510, 154, doi: [10.1093/mnras/stab3417](https://doi.org/10.1093/mnras/stab3417)
- Genzel, R., Tacconi, L. J., Eisenhauer, F., et al. 2006, *Nature*, 442, 786
- Genzel, R., Price, S. H., Übler, H., et al. 2020, *ApJ*, 902, 98, doi: [10.3847/1538-4357/abb0ea](https://doi.org/10.3847/1538-4357/abb0ea)
- George, K., Subramanian, S., & Paul, K. T. 2019, *A&A*, 628, A24, doi: [10.1051/0004-6361/201935207](https://doi.org/10.1051/0004-6361/201935207)
- Gerrard, I. A., Federrath, C., Pingel, N. M., et al. 2023, *MNRAS*, 526, 982, doi: [10.1093/mnras/stad2718](https://doi.org/10.1093/mnras/stad2718)
- Goad, J. W., & Roberts, M. S. 1981, *ApJ*, 250, 79, doi: [10.1086/159349](https://doi.org/10.1086/159349)
- Grisdale, K., Agertz, O., Renaud, F., & Romeo, A. B. 2018, *MNRAS*, doi: [10.1093/mnras/sty1595](https://doi.org/10.1093/mnras/sty1595)
- Grisdale, K., Agertz, O., Renaud, F., et al. 2019, *MNRAS*, 486, 5482, doi: [10.1093/mnras/stz1201](https://doi.org/10.1093/mnras/stz1201)
- Grisdale, K., Agertz, O., Romeo, A. B., Renaud, F., & Read, J. I. 2017, *MNRAS*, 466, 1093, doi: [10.1093/mnras/stw3133](https://doi.org/10.1093/mnras/stw3133)
- Guo, Y., Jogee, S., Finkelstein, S. L., et al. 2022, arXiv e-prints, arXiv:2210.08658, <https://arxiv.org/abs/2210.08658>
- Gurvich, A. B., Stern, J., Faucher-Giguère, C.-A., et al. 2022, Rapid disc settling and the transition from bursty to steady star formation in Milky Way-mass galaxies, arXiv, doi: [10.48550/ARXIV.2203.04321](https://doi.org/10.48550/ARXIV.2203.04321)
- Haardt, F., & Madau, P. 1996, *ApJ*, 461, 20, doi: [10.1086/177035](https://doi.org/10.1086/177035)
- Hancock, C. 2019, Master's thesis, University of Alabama, Tuscaloosa
- Hayden, M. R., Bovy, J., Holtzman, J. A., et al. 2015, *ApJ*, 808, 132
- Haywood, M., Di Matteo, P., Lehnert, M. D., et al. 2018, *ApJ*, 863, 113, doi: [10.3847/1538-4357/aad235](https://doi.org/10.3847/1538-4357/aad235)
- Hennebelle, P., & Chabrier, G. 2011, *ApJL*, 743, L29, doi: [10.1088/2041-8205/743/2/L29](https://doi.org/10.1088/2041-8205/743/2/L29)
- Heyer, M. H., & Brunt, C. M. 2004, *ApJL*, 615, L45, doi: [10.1086/425978](https://doi.org/10.1086/425978)
- Hodge, J. A., Smail, I., Walter, F., et al. 2019, *ApJ*, 876, 130, doi: [10.3847/1538-4357/ab1846](https://doi.org/10.3847/1538-4357/ab1846)
- Hohl, F. 1971, *ApJ*, 168, 343, doi: [10.1086/151091](https://doi.org/10.1086/151091)
- Hopkins, A. M. 2018, ArXiv e-prints, <https://arxiv.org/abs/1807.09949>
- Huang, S., Kawabe, R., Kohno, K., et al. 2023, arXiv e-prints, arXiv:2310.01782, doi: [10.48550/arXiv.2310.01782](https://doi.org/10.48550/arXiv.2310.01782)
- Huertas-Company, M., Iyer, K. G., Angeloudi, E., et al. 2023, arXiv e-prints, arXiv:2305.02478, doi: [10.48550/arXiv.2305.02478](https://doi.org/10.48550/arXiv.2305.02478)
- Hüttemeister, S., Aalto, S., & Wall, W. F. 1999, *A&A*, 346, 45, doi: [10.48550/arXiv.astro-ph/9903409](https://doi.org/10.48550/arXiv.astro-ph/9903409)
- Ida, S., Kokubo, E., & Makino, J. 1993, *MNRAS*, 263, 875, doi: [10.1093/mnras/263.4.875](https://doi.org/10.1093/mnras/263.4.875)
- Jog, C. J., & Solomon, P. M. 1984, *ApJ*, 276, 114, doi: [10.1086/161597](https://doi.org/10.1086/161597)
- Kartalpe, J., Rose, C., Vanderhoof, B., & Ceers Collaboration. 2023, in American Astronomical Society Meeting Abstracts, Vol. 55, American Astronomical Society Meeting Abstracts, 102.01
- Katz, H., Liu, S., Kimm, T., et al. 2022, arXiv e-prints, arXiv:2211.04626, doi: [10.48550/arXiv.2211.04626](https://doi.org/10.48550/arXiv.2211.04626)
- Kaufmann, T., Mayer, L., Wadsley, J., Stadel, J., & Moore, B. 2006, *MNRAS*, 370, 1612
- Kennicutt, Robert C., J. 1998, *ApJ*, 498, 541, doi: [10.1086/305588](https://doi.org/10.1086/305588)

- Kim, C.-G., & Ostriker, E. C. 2015, *ApJ*, 802, 99, doi: [10.1088/0004-637X/802/2/99](https://doi.org/10.1088/0004-637X/802/2/99)
- Kim, J.-h., Abel, T., & Agertz, O. e. a. 2014, *ApJS*, 210, 14, doi: [10.1088/0067-0049/210/1/14](https://doi.org/10.1088/0067-0049/210/1/14)
- Klessen, R. S., Heitsch, F., & Mac Low, M.-M. 2000, *ApJ*, 535, 887, doi: [10.1086/308891](https://doi.org/10.1086/308891)
- Kohno, K., Tosaki, T., Miura, R., et al. 2008, *PASJ*, 60, 457, doi: [10.1093/pasj/60.3.457](https://doi.org/10.1093/pasj/60.3.457)
- Kretschmer, M., Dekel, A., & Teyssier, R. 2022, *MNRAS*, 510, 3266, doi: [10.1093/mnras/stab3648](https://doi.org/10.1093/mnras/stab3648)
- Kritsuk, A. G., Norman, M. L., Padoan, P., & Wagner, R. 2007, *ApJ*, 665, 416, doi: [10.1086/519443](https://doi.org/10.1086/519443)
- Krumholz, M. R., & McKee, C. F. 2005, *ApJ*, 630, 250, doi: [10.1086/431734](https://doi.org/10.1086/431734)
- Krumholz, M. R., McKee, C. F., & Klein, R. I. 2005a, *Nature*, 438, 332, doi: [10.1038/nature04280](https://doi.org/10.1038/nature04280)
- . 2005b, *ApJ*, 618, 757, doi: [10.1086/426051](https://doi.org/10.1086/426051)
- . 2006, *ApJ*, 638, 369, doi: [10.1086/498844](https://doi.org/10.1086/498844)
- Larson, R. B. 1981, *MNRAS*, 194, 809
- Law, D. R., Shapley, A. E., Steidel, C. C., et al. 2012, *Nature*, 487, 338, doi: [10.1038/nature11256](https://doi.org/10.1038/nature11256)
- Le Conte, Z. A., Gadotti, D. A., Ferreira, L., et al. 2023, arXiv e-prints, arXiv:2309.10038, doi: [10.48550/arXiv.2309.10038](https://doi.org/10.48550/arXiv.2309.10038)
- Lee, A. T., Cunningham, A. J., McKee, C. F., & Klein, R. I. 2014, *ApJ*, 783, 50, doi: [10.1088/0004-637X/783/1/50](https://doi.org/10.1088/0004-637X/783/1/50)
- Leitherer, C., Schaerer, D., Goldader, J. D., et al. 1999, *ApJS*, 123, 3, doi: [10.1086/313233](https://doi.org/10.1086/313233)
- Li, P. S., Norman, M. L., Mac Low, M.-M., & Heitsch, F. 2004, *ApJ*, 605, 800, doi: [10.1086/382652](https://doi.org/10.1086/382652)
- Li, Y., Klessen, R. S., & Mac Low, M.-M. 2003, *ApJ*, 592, 975, doi: [10.1086/375780](https://doi.org/10.1086/375780)
- Ma, X., Hopkins, P. F., Wetzel, A. R., et al. 2017, *MNRAS*, 467, 2430, doi: [10.1093/mnras/stx273](https://doi.org/10.1093/mnras/stx273)
- Mac Low, M.-M., & Klessen, R. S. 2004, *Reviews of Modern Physics*, 76, 125, doi: [10.1103/RevModPhys.76.125](https://doi.org/10.1103/RevModPhys.76.125)
- Margalef-Bentabol, B., Conselice, C. J., Haeussler, B., et al. 2022, *MNRAS*, 511, 1502, doi: [10.1093/mnras/stac080](https://doi.org/10.1093/mnras/stac080)
- Martin, C. L., & Kennicutt, Robert C., J. 2001, *ApJ*, 555, 301, doi: [10.1086/321452](https://doi.org/10.1086/321452)
- McCluskey, F., Wetzel, A., Loebman, S. R., et al. 2024, *MNRAS*, 527, 6926, doi: [10.1093/mnras/stad3547](https://doi.org/10.1093/mnras/stad3547)
- Meidt, S. E. 2022, *ApJ*, 937, 88, doi: [10.3847/1538-4357/ac86ce](https://doi.org/10.3847/1538-4357/ac86ce)
- Mo, H. J., Mao, S., & White, S. D. M. 1998, *MNRAS*, 295, 319
- Molina, F. Z., Glover, S. C. O., Federrath, C., & Klessen, R. S. 2012, *MNRAS*, 423, 2680, doi: [10.1111/j.1365-2966.2012.21075.x](https://doi.org/10.1111/j.1365-2966.2012.21075.x)
- Neeleman, M., Walter, F., Decarli, R., et al. 2023, arXiv e-prints, arXiv:2311.00771, doi: [10.48550/arXiv.2311.00771](https://doi.org/10.48550/arXiv.2311.00771)
- Neeleman, M., Novak, M., Venemans, B. P., et al. 2021, *ApJ*, 911, 141
- Neichel, B., Hammer, F., Puech, M., et al. 2008, *A&A*, 484, 159, doi: [10.1051/0004-6361:20079226](https://doi.org/10.1051/0004-6361:20079226)
- Nolan, C. A., Federrath, C., & Sutherland, R. S. 2015, *MNRAS*, 451, 1380, doi: [10.1093/mnras/stv1030](https://doi.org/10.1093/mnras/stv1030)
- Ossa-Fuentes, L., Borlaff, A. S., Beckman, J. E., Marcum, P. M., & Fanelli, M. N. 2023, *ApJ*, 951, 149, doi: [10.3847/1538-4357/acd54c](https://doi.org/10.3847/1538-4357/acd54c)
- Ossenkopf, V., & Mac Low, M.-M. 2002, *A&A*, 390, 307, doi: [10.1051/0004-6361:20020629](https://doi.org/10.1051/0004-6361:20020629)
- Padoan, P. 1995, *MNRAS*, 277, 377, doi: [10.1093/mnras/277.2.377](https://doi.org/10.1093/mnras/277.2.377)
- Padoan, P., & Nordlund, Å. 2002, *ApJ*, 576, 870, doi: [10.1086/341790](https://doi.org/10.1086/341790)
- . 2011, *ApJ*, 730, 40, doi: [10.1088/0004-637X/730/1/40](https://doi.org/10.1088/0004-637X/730/1/40)
- Pandya, V., Zhang, H., Huertas-Company, M., et al. 2023, arXiv e-prints, arXiv:2310.15232, doi: [10.48550/arXiv.2310.15232](https://doi.org/10.48550/arXiv.2310.15232)
- Passot, T., & Vázquez-Semadeni, E. 1998, *PhRvE*, 58, 4501
- Planck Collaboration, Aghanim, N., Akrami, Y., et al. 2020, *A&A*, 641, A6
- Pop, A.-R., Pillepich, A., Amorisco, N. C., & Hernquist, L. 2018, *MNRAS*, 480, 1715, doi: [10.1093/mnras/sty1932](https://doi.org/10.1093/mnras/sty1932)
- Price, S. H., Shimizu, T. T., Genzel, R., et al. 2021, *ApJ*, 922, 143, doi: [10.3847/1538-4357/ac22ad](https://doi.org/10.3847/1538-4357/ac22ad)
- Quinn, P. J. 1984, *ApJ*, 279, 596, doi: [10.1086/161924](https://doi.org/10.1086/161924)
- Quinn, P. J., Hernquist, L., & Fullagar, D. P. 1993, *ApJ*, 403, 74, doi: [10.1086/172184](https://doi.org/10.1086/172184)
- Rafikov, R. R. 2001, *MNRAS*, 323, 445, doi: [10.1046/j.1365-8711.2001.04201.x](https://doi.org/10.1046/j.1365-8711.2001.04201.x)
- Raiteri, C. M., Villata, M., & Navarro, J. F. 1996, *A&A*, 315, 105. http://adsabs.harvard.edu/cgi-bin/nph-data_query?bibcode=1996A%2526A...315..105R&link_type=ABSTRACT
- Renaud, F., Bournaud, F., Emsellem, E., et al. 2015, *MNRAS*, 454, 3299, doi: [10.1093/mnras/stv2223](https://doi.org/10.1093/mnras/stv2223)
- Reshetnikov, V., & Combes, F. 1998, *A&A*, 337, 9, doi: [10.48550/arXiv.astro-ph/9806114](https://doi.org/10.48550/arXiv.astro-ph/9806114)
- Rix, H.-W., & Zaritsky, D. 1995, *ApJ*, 447, 82, doi: [10.1086/175858](https://doi.org/10.1086/175858)
- Rizzo, F., Kohandel, M., Pallottini, A., et al. 2022, arXiv e-prints, arXiv:2204.05325
- Rizzo, F., Vegetti, S., Powell, D., et al. 2020, *Nature*, 584, 201, doi: [10.1038/s41586-020-2572-6](https://doi.org/10.1038/s41586-020-2572-6)
- Robertson, B. E., Tacchella, S., Johnson, B. D., et al. 2023, *ApJL*, 942, L42, doi: [10.3847/2041-8213/aca086](https://doi.org/10.3847/2041-8213/aca086)

- Robichaud, F., Williamson, D., Martel, H., Kawata, D., & Ellison, S. L. 2017, *MNRAS*, 469, 3722, doi: [10.1093/mnras/stx1121](https://doi.org/10.1093/mnras/stx1121)
- Rodrigues, M., Hammer, F., Flores, H., Puech, M., & Athanassoula, E. 2017, *MNRAS*, 465, 1157, doi: [10.1093/mnras/stw2711](https://doi.org/10.1093/mnras/stw2711)
- Roman-Duval, J., Federrath, C., Brunt, C., et al. 2011, *ApJ*, 740, 120, doi: [10.1088/0004-637X/740/2/120](https://doi.org/10.1088/0004-637X/740/2/120)
- Romeo, A. B. 1992, *MNRAS*, 256, 307, doi: [10.1093/mnras/256.2.307](https://doi.org/10.1093/mnras/256.2.307)
- Romeo, A. B., Burkert, A., & Agertz, O. 2010, *MNRAS*, 407, 1223, doi: [10.1111/j.1365-2966.2010.16975.x](https://doi.org/10.1111/j.1365-2966.2010.16975.x)
- Rosen, A., & Bregman, J. N. 1995, *ApJ*, 440, 634, doi: [10.1086/175303](https://doi.org/10.1086/175303)
- Rosolowsky, E., & Blitz, L. 2005, *ApJ*, 623, 826, doi: [10.1086/428897](https://doi.org/10.1086/428897)
- Roškar, R., Debattista, V. P., Quinn, T. R., Stinson, G. S., & Wadsley, J. 2008, *ApJL*, 684, L79, doi: [10.1086/592231](https://doi.org/10.1086/592231)
- Ruffert, M., & Arnett, D. 1994, *ApJ*, 427, 351, doi: [10.1086/174145](https://doi.org/10.1086/174145)
- Sellwood, J. A., & Binney, J. J. 2002, *MNRAS*, 336, 785, doi: [10.1046/j.1365-8711.2002.05806.x](https://doi.org/10.1046/j.1365-8711.2002.05806.x)
- Sellwood, J. A., & Carlberg, R. G. 1984, *ApJ*, 282, 61, doi: [10.1086/162176](https://doi.org/10.1086/162176)
- Sellwood, J. A., & Wilkinson, A. 1993, *Reports on Progress in Physics*, 56, 173, doi: [10.1088/0034-4885/56/2/001](https://doi.org/10.1088/0034-4885/56/2/001)
- Seo, W.-Y., Kim, W.-T., Kwak, S., et al. 2019, *ApJ*, 872, 5, doi: [10.3847/1538-4357/aafc5f](https://doi.org/10.3847/1538-4357/aafc5f)
- Shapiro, K. L., Genzel, R., Förster Schreiber, N. M., et al. 2008, *ApJ*, 682, 231, doi: [10.1086/587133](https://doi.org/10.1086/587133)
- Sharma, S., & Bland-Hawthorn, J. 2013, *ApJ*, 773, 183, doi: [10.1088/0004-637X/773/2/183](https://doi.org/10.1088/0004-637X/773/2/183)
- Sharma, S., Hayden, M. R., Bland-Hawthorn, J., et al. 2021, *MNRAS*, 506, 1761, doi: [10.1093/mnras/stab1086](https://doi.org/10.1093/mnras/stab1086)
- Simons, R. C., Kassin, S. A., Snyder, G. F., et al. 2019, *ApJ*, 874, 59, doi: [10.3847/1538-4357/ab07c9](https://doi.org/10.3847/1538-4357/ab07c9)
- Smail, I., Dudzeviciute, U., Gurwell, M., et al. 2023, *arXiv e-prints*, arXiv:2306.16039, doi: [10.48550/arXiv.2306.16039](https://doi.org/10.48550/arXiv.2306.16039)
- Solomon, P. M., Rivolo, A. R., Barrett, J., & Yahil, A. 1987, *ApJ*, 319, 730, doi: [10.1086/165493](https://doi.org/10.1086/165493)
- Sorce, J. G., Gottlöber, S., Yepes, G., et al. 2016, *MNRAS*, 455, 2078, doi: [10.1093/mnras/stv2407](https://doi.org/10.1093/mnras/stv2407)
- Sutherland, R. S., & Dopita, M. A. 1993, *ApJS*, 88, 253, doi: [10.1086/191823](https://doi.org/10.1086/191823)
- Swinbank, A. M., Smail, I., Sobral, D., et al. 2012, *ApJ*, 760, 130, doi: [10.1088/0004-637X/760/2/130](https://doi.org/10.1088/0004-637X/760/2/130)
- Tacconi, L. J., Genzel, R., & Sternberg, A. 2020, *ARA&A*, 58, 157, doi: [10.1146/annurev-astro-082812-141034](https://doi.org/10.1146/annurev-astro-082812-141034)
- Takahira, K., Shima, K., Habe, A., & Tasker, E. J. 2018, *PASJ*, 70, S58, doi: [10.1093/pasj/psy011](https://doi.org/10.1093/pasj/psy011)
- Tan, J. C. 2000, *ApJ*, 536, 173, doi: [10.1086/308905](https://doi.org/10.1086/308905)
- Tasker, E. J., & Tan, J. C. 2009, *ApJ*, 700, 358, doi: [10.1088/0004-637X/700/1/358](https://doi.org/10.1088/0004-637X/700/1/358)
- Tepper-Garcia, T., Bland-Hawthorn, J., & Freeman, K. 2022, *arXiv e-prints*, arXiv:2204.12096
- Tepper-Garcia, T., Bland-Hawthorn, J., Vasiliev, E., et al. 2021, *arXiv e-prints*, arXiv:2111.05466
- Teyssier, R. 2002, *A&A*, 385, 337
- Teyssier, R., Pontzen, A., Dubois, Y., & Read, J. I. 2013, *MNRAS*, 429, 3068
- Thornton, K., Gaudlitz, M., Janka, H.-T., & Steinmetz, M. 1998, *ApJ*, 500, 95, doi: [10.1086/305704](https://doi.org/10.1086/305704)
- Toomre, A. 1981, in *Structure and Evolution of Normal Galaxies*, ed. S. M. Fall & D. Lynden-Bell, 111–136
- Toomre, A., & Toomre, J. 1972, *ApJ*, 178, 623, doi: [10.1086/151823](https://doi.org/10.1086/151823)
- Toro, E. F. 1999, *Riemann Solvers and Numerical Methods for Fluid Dynamics*, 2nd edition (Springer-Verlag, Berlin/Heidelberg/New York)
- Tsukui, T., & Iguchi, S. 2021, *Science*, 372, 1201, doi: [10.1126/science.abe9680](https://doi.org/10.1126/science.abe9680)
- Tsukui, T., Wisnioski, E., Bland-Hawthorn, J., et al. 2024, *MNRAS*, 527, 8941, doi: [10.1093/mnras/stad3588](https://doi.org/10.1093/mnras/stad3588)
- Tsukui, T., Wisnioski, E., Krumholz, M. R., & Battisti, A. 2023, *MNRAS*, 523, 4654, doi: [10.1093/mnras/stad1464](https://doi.org/10.1093/mnras/stad1464)
- Tumlinson, J., Peebles, M. S., & Werk, J. K. 2017, *ARA&A*, 55, 389, doi: [10.1146/annurev-astro-091916-055240](https://doi.org/10.1146/annurev-astro-091916-055240)
- Urrejola-Mora, C., Gómez, F. A., Torres-Flores, S., et al. 2022, *ApJ*, 935, 20, doi: [10.3847/1538-4357/ac78ec](https://doi.org/10.3847/1538-4357/ac78ec)
- van Dokelaar, F., Agertz, O., & Renaud, F. 2022, *MNRAS*, 512, 3806, doi: [10.1093/mnras/stac692](https://doi.org/10.1093/mnras/stac692)
- Vasiliev, E. 2019, *MNRAS*, 482, 1525
- Vázquez-Semadeni, E. 1994, *ApJ*, 423, 681, doi: [10.1086/173847](https://doi.org/10.1086/173847)
- Villa-Vargas, J., Shlosman, I., & Heller, C. 2010, *ApJ*, 719, 1470
- Walker, I. R., Mihos, J. C., & Hernquist, L. 1996, *ApJ*, 460, 121, doi: [10.1086/176956](https://doi.org/10.1086/176956)
- Walter, F., Neeleman, M., Decarli, R., et al. 2022, *ApJ*, 927, 21, doi: [10.3847/1538-4357/ac49e8](https://doi.org/10.3847/1538-4357/ac49e8)
- Wang, H.-H., Klessen, R. S., Dullemond, C. P., van den Bosch, F. C., & Fuchs, B. 2010, *MNRAS*, 407, 705
- Wisnioski, E., Förster Schreiber, N. M., Wuyts, S., et al. 2015, *ApJ*, 799, 209
- Woosley, S. E., & Heger, A. 2007, *PhR*, 442, 269, doi: [10.1016/j.physrep.2007.02.009](https://doi.org/10.1016/j.physrep.2007.02.009)

Yuan, T., Richard, J., Gupta, A., et al. 2017, ApJ, 850, 61,
doi: [10.3847/1538-4357/aa951d](https://doi.org/10.3847/1538-4357/aa951d)

Zhou, L., Federrath, C., Yuan, T., et al. 2017, MNRAS,
470, 4573, doi: [10.1093/mnras/stx1504](https://doi.org/10.1093/mnras/stx1504)